Astronomy Letters, Vol. 28, No. 5, 2002, pp. 279–286. Translated from Pis'ma v Astronomicheskiĭ Zhurnal, Vol. 28, No. 5, 2002, pp. 323–330.

Long-Term Mir–Kvant Observations of the Transient X-ray Burster KS 1731–260

N. L. Aleksandrovich[1], M. G. Revnivtsev[1,2], V. A. Aref'ev[1*], R. A. Sunyaev[2,1], and G. K. Skinner[3]

[1] *Space Research Institute, Russian Academy of Sciences, ul. Profsoyuznaya 84/32, Moscow, 117810 Russia*

[2] *Max-Planck Institut für Astrophysik, Karl-Schwarzschild-Str. 1, Garching bei München, 85740 Germany*

[3] *University of Birmingham, Edgbaston, Birmingham, B152TT, UK*

Received October 22, 2001

Abstract—We present the observations of the X-ray burster KS 1731–260 from 1988 until 1999 with the Kvant/TTM telescope supplemented with published data from the ASM and PCA instruments of the RXTE observatory for 1996–2001. We constructed the light curve of the source and confirmed the dependence of spectral variations on its X-ray luminosity. © *2002 MAIK "Nauka/Interperiodica".*

Key words: *Mir–Kvant orbiting observatory, X-ray bursters*

INTRODUCTION

The X-ray burster KS 1731–260 was discovered and localized with the TTM telescope of the Mir–Kvant orbiting observatory during the observations of the Galactic-center region in August 1989 (Sunyaev 1989). The image of the region around KS 1731–260 obtained from all TTM observations is shown in Fig. 1. Over the entire period of TTM observations, the flux from this source varied within the range 50–200 mCrab (in the 2–27 keV energy band); several type I X-ray bursts with duration of 10–20 s and a peak flux up to 600 mCrab were detected (Sunyaev *et al.* 1990). On September 23, 1996, the BeppoSax satellite recorded a long ($\sim$12 h) burst with the same peak flux (in the 2–28 keV energy band); otherwise, it is similar to a type I burst (Kuulkers *et al.* 2001). This is the longest X-ray burst known to date.

Optical observations of this source are severely hampered by its proximity to the Galactic plane and, hence, by substantial optical interstellar absorption. Infrared observations of KS 1731–260 also failed to clearly reveal a companion star (Barret *et al.* 1998). Recently, using the Chandra improved position of KS 1731–260 (Revnivtsev and Sunyaev 2001; Wijnands *et al.* 2001), efforts to search for an infrared counterpart of this source have been significantly intensified (Wijnands *et al.* 2001; Revnivtsev and Sunyaev 2001; Orosz *et al.* 2001). A $\sim 18^m$ star is currently the most reliable candidate for infrared counterparts of the source (Orosz *et al.* 2001).

*E-mail: gita@hea.iki.rssi.ru

INSTRUMENTS AND OBSERVATIONS

In this paper, we analyze data from the TTM X-ray telescope of the Roentgen orbiting observatory. We also use data from the All-Sky Monitor (ASM) and the PCA spectrometer of the RXTE observatory to describe the long-term evolution of KS 1731–260 in more detail.

The TTM (shadow-mask telescope) X-ray telescope had been in operation in a near-Earth orbit as part of the Roentgen observatory onboard the Mir–Kvant module from 1987 until 1999. The instrument was sensitive to X-ray emission in the 2–27 keV energy band (with the highest efficiency in the soft region) and was capable of forming images within a $15^\circ \times 15^\circ$ (beam FWHM) field of view with an angular resolution of $\approx$2 arcmin (Brinkman *et al.* 1983). The telescope could also obtain the spectra (in 30 energy channels) of bright sources that fell within its field of view. Because of the low ($\approx$350 km) orbit and its significant ($\sim 52^\circ$) inclination to the equator, the orbiting station passed twice a period through the radiation belts, the high-latitude regions where the Earth's magnetic field confines charged particles with energies that were high enough to be detectable with the sensitive instruments of the observatory. Since these particles produced a high background, the instrumentation was always switched off during the passage through the radiation belts. Therefore, the duration of a single TTM observing session did not exceed 30 min.

The RXTE X-ray observatory was placed into orbit in December 1995. It consisted of the All-Sky

1063-7737/02/2805-0279$22.00

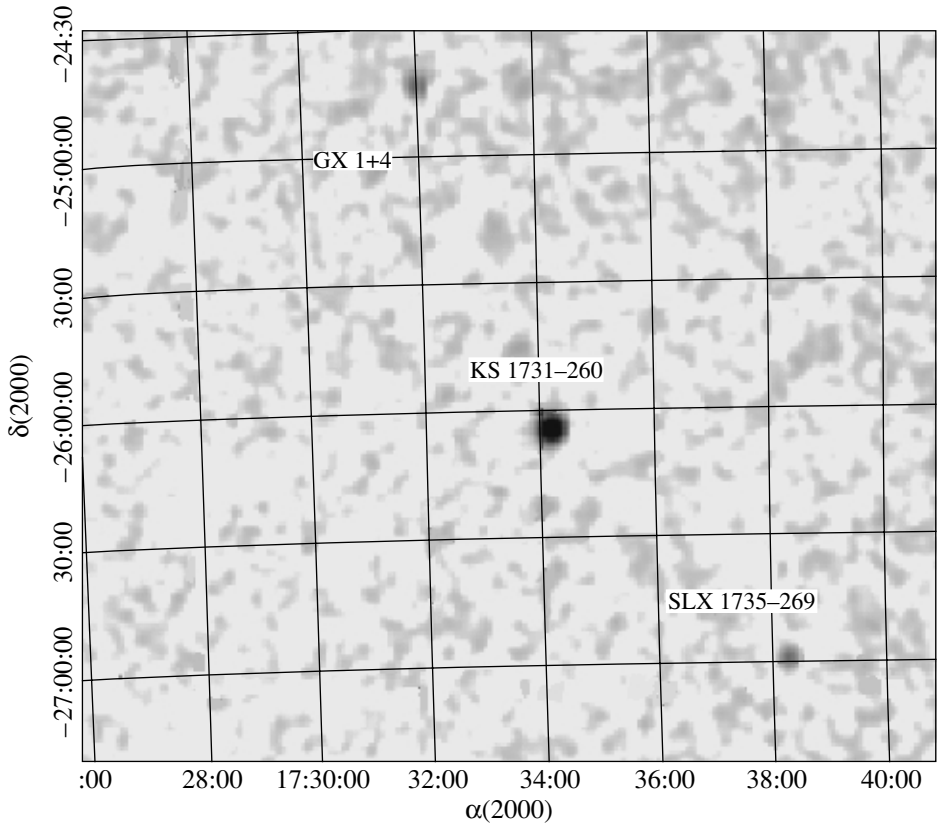

Fig. 1. The map of the region around KS 1731–260 obtained from all TTM 2–27 keV observations. Equatorial coordinates are along the axes.

Monitor (ASM) operating in the 2–12 keV energy band, the PCA spectrometer (operating in the 2–20 keV energy band), and the HEXTE spectrometer (20–250 keV energy band). The ASM light curves were taken from the MIT archive (http://xte.mit.edu/ASM_lc.html). The PCA data were processed with the standard FTOOLS/LHEASOFT software package using RXTE CookBook recipes (http://legacy.gsfc.nasa.gov/docs/xte/recipes/cook_book.html). Here, we did not use data from the HEXTE spectrometer, because its operating energy band lay virtually outside the TTM energy range.

THE LIGHT CURVE

The light curve of the burster KS 1731–260, as constructed from the TTM (1987–1999, 2–27 keV energy band) and ASM (1996–2001, 2–12 keV) data, is shown in Fig. 2. More detailed data on 131 TTM observing sessions are given in the table. Interestingly, the TTM and ASM observations almost completely cover the history of KS 1731–260, from its discovery in 1989 (its appearance in the X-ray sky with a flux higher than ~40 mCrab) until its return to the off state in 2001. The Chandra observations in 2001 showed the off-state luminosity of the source to be 10^{33} erg s^{-1}.

The source exhibited a significant variability over the entire observing period. However, there is evidence that the variability amplitude of the source X-ray flux decreased with increasing mean flux. Thus, according to the ASM data (Fig. 2), the variability amplitude of KS 1731–260 in 1996–1997 (TJD ~ 10 200–10 700) was small, while in 1998–2001, it was much larger.

It should be noted that a reanalysis of the archival TTM observations revealed evidence for the presence of the source (at a ~20-mCrab level with ~4σ confidence) in one of the four sessions carried out on October 21, 1988, i.e., eight months before the first publication on its discovery. However, the confidence level of the recorded flux is too low to assert with certainty that the source is present.

Variability of the source on time scales of several days is clearly seen in Fig. 3, which shows the light curve of KS 1731–260 for August–September 1989. The significant increase in the measurement errors of the fluxes for the sessions of August 22 and 23, 1989 (MJD 7760–7762), stems from the fact that during these observations, the source was at the very edge of

The TTM observational data on the burster KS 1731–260 for 1988–1999 shown in Figs. 2 and 3: R is the angular distance of the source from the center of the TTM field of view; the flux is given for the 2–27 keV energy band. An (3σ) upper limit on the flux is given for the sessions when the source was not detected.

Date	MJD	Exposure, min	R	Flux, mCrab	Date	MJD	Exposure, min	R	Flux, mCrab
Oct. 21, 1988	7455.491	11.85	0.77	<17	Aug. 31, 1989	7769.010	15.60	1.02	77 ± 3
Oct. 21, 1988	7455.554	11.85	0.73	<17	Aug. 31, 1989	7769.074	15.60	0.97	77 ± 4
Oct. 21, 1988	7455.617	11.60	0.68	<16	Aug. 31, 1989	7769.138	15.62	0.93	77 ± 3
Oct. 21, 1988	7455.681	11.63	0.65	18 ± 5	Aug. 31, 1989	7769.202	15.62	0.88	67 ± 4
Mar. 20, 1989	7605.724	11.60	4.07	<23	Sep. 4, 1989	7772.919	11.60	0.54	83 ± 4
Mar. 20, 1989	7605.787	11.62	4.02	<23	Sep. 4, 1989	7772.982	10.00	0.55	83 ± 4
Mar. 20, 1989	7605.851	11.62	3.96	<22	Sep. 4, 1989	7773.046	11.60	0.58	90 ± 5
Mar. 21, 1989	7605.915	11.35	3.93	<21	Sep. 4, 1989	7773.110	11.60	0.62	89 ± 5
Mar. 21, 1989	7605.978	11.62	3.87	<21	Sep. 4, 1989	7773.175	10.80	0.62	89 ± 6
Mar. 21, 1989	7606.042	11.67	3.82	<21	Sep. 4, 1989	7773.239	10.28	0.67	78 ± 6
Apr. 1, 1989	7617.726	19.10	5.75	<23	Sep. 5, 1989	7773.880	7.60	1.12	93 ± 5
Apr. 1, 1989	7617.790	20.00	5.65	<22	Sep. 5, 1989	7773.944	7.60	1.19	86 ± 5
Aug. 16, 1989	7754.201	19.60	0.08	71 ± 3	Sep. 5, 1989	7774.008	7.60	1.24	86 ± 5
Aug. 16, 1989	7754.267	17.15	0.20	92 ± 3	Sep. 5, 1989	7774.072	7.60	1.28	86 ± 5
Aug. 16, 1989	7754.330	19.35	0.38	83 ± 3	Sep. 5, 1989	7774.136	7.62	1.35	85 ± 8
Aug. 16, 1989	7754.394	19.62	0.52	60 ± 3	Sep. 5, 1989	7774.202	4.80	1.40	89 ± 13
Aug. 16, 1989	7754.458	19.62	0.67	70 ± 3	Sep. 9, 1989	7778.199	10.78	9.27	<132
Aug. 16, 1989	7754.522	19.88	0.89	71 ± 3	Sep. 9, 1989	7778.327	10.55	9.33	<131
Aug. 16, 1989	7754.586	19.35	1.05	65 ± 3	Oct. 17, 1992	8912.801	11.90	5.97	87 ± 18
Aug. 20, 1989	7758.176	19.35	0.93	77 ± 3	Oct. 18, 1992	8913.830	15.92	5.92	112 ± 14
Aug. 20, 1989	7758.240	19.35	0.85	112 ± 3	Oct. 19, 1992	8913.894	15.90	5.91	74 ± 13
Aug. 20, 1989	7758.303	19.35	0.79	122 ± 3	Oct. 20, 1992	8914.925	14.32	6.20	94 ± 18
Aug. 20, 1989	7758.367	19.35	0.78	116 ± 3	Oct. 20, 1992	8914.989	16.58	6.19	76 ± 18
Aug. 20, 1989	7758.429	12.15	0.79	119 ± 4	Oct. 23, 1992	8917.945	11.88	4.26	114 ± 8
Aug. 20, 1989	7758.495	19.35	0.82	96 ± 3	Oct. 23, 1992	8918.009	11.92	4.27	156 ± 8
Aug. 20, 1989	7758.559	19.35	0.92	121 ± 3	Oct. 24, 1992	8918.910	13.18	4.22	148 ± 8
Aug. 21, 1989	7759.137	19.60	0.94	93 ± 3	Oct. 24, 1992	8918.974	11.90	4.23	150 ± 8
Aug. 21, 1989	7759.266	19.62	0.68	110 ± 3	Sep. 26, 1993	9256.042	23.12	1.17	162 ± 3
Aug. 21, 1989	7759.330	19.62	0.60	100 ± 3	Sep. 27, 1993	9257.131	25.38	1.43	132 ± 4
Aug. 21, 1989	7759.394	19.62	0.55	89 ± 3	Oct. 3, 1993	9262.959	18.27	4.17	110 ± 6
Aug. 21, 1989	7759.458	19.62	0.55	107 ± 3	Oct. 3, 1993	9263.023	19.60	4.20	120 ± 6
Aug. 21, 1989	7759.522	19.52	0.64	107 ± 4	Oct. 7, 1993	9267.188	11.60	3.45	150 ± 6
Aug. 22, 1989	7760.163	19.60	6.67	67 ± 9	Oct. 24, 1993	9283.962	19.60	3.18	201 ± 5
Aug. 22, 1989	7760.227	19.62	6.85	62 ± 9	Mar. 14, 1994	9425.581	19.65	3.46	146 ± 3
Aug. 22, 1989	7760.292	20.50	6.99	64 ± 10	Mar. 15, 1994	9426.607	19.92	4.23	162 ± 6
Aug. 22, 1989	7760.356	19.62	7.13	61 ± 10	Mar. 16, 1994	9427.569	19.60	4.32	125 ± 7
Aug. 22, 1989	7760.419	20.77	7.28	63 ± 12	Mar. 17, 1994	9428.531	15.47	4.25	164 ± 11
Aug. 22, 1989	7760.484	19.75	7.47	51 ± 14	Mar. 18, 1994	9429.557	19.07	4.38	176 ± 7
Aug. 23, 1989	7761.060	20.02	6.70	57 ± 9	Mar. 19, 1994	9430.519	19.60	3.97	177 ± 6
Aug. 23, 1989	7761.190	17.60	7.01	36 ± 11	Mar. 20, 1994	9431.481	19.60	3.44	182 ± 3
Aug. 23, 1989	7761.381	17.75	7.51	56 ± 14	May 6, 1994	9478.317	23.60	4.29	135 ± 6

Table. (Contd.)

Date	MJD	Exposure, min	R	Flux, mCrab	Date	MJD	Exposure, min	R	Flux, mCrab
May 8, 1994	9481.524	23.60	4.27	89 ± 6	Sep. 12, 1995	9972.256	19.60	6.09	129 ± 17
May 12, 1994	9484.601	19.33	4.38	107 ± 7	Sep. 16, 1995	9976.235	23.33	5.78	158 ± 13
May 12, 1994	9484.665	17.73	4.35	93 ± 7	Sep. 17, 1995	9977.262	23.60	4.12	170 ± 6
May 15, 1994	9487.166	20.00	4.43	88 ± 6	Sep. 18, 1995	9978.481	23.60	4.13	150 ± 5
May 15, 1994	9487.232	16.45	4.37	103 ± 7	Sep. 19, 1995	9979.439	9.20	4.25	154 ± 9
Aug. 29, 1994	9593.738	19.33	4.34	109 ± 6	Nov. 4, 1995	10025.635	19.92	4.55	73 ± 5
Aug. 31, 1994	9595.792	18.80	4.56	92 ± 7	Nov. 4, 1995	10025.699	19.87	4.47	56 ± 5
Sep. 1, 1994	9596.691	19.33	4.50	151 ± 7	Feb. 6, 1996	10119.103	23.65	3.73	98 ± 13
Sep. 23, 1994	9618.129	22.80	4.24	131 ± 6	Feb. 6, 1996	10119.681	23.92	3.71	87 ± 13
Sep. 26, 1994	9621.210	21.73	4.16	126 ± 8	Feb. 7, 1996	10120.643	23.92	3.70	118 ± 14
Sep. 27, 1994	9622.172	23.60	4.13	88 ± 7	Feb. 28, 1996	10141.655	15.92	3.64	54 ± 11
Sep. 28, 1994	9623.135	19.60	4.16	111 ± 7	Mar. 1, 1996	10143.772	15.92	3.78	225 ± 17
Feb. 16, 1995	9763.922	23.32	5.15	52 ± 5	Mar. 1, 1996	10143.836	15.85	3.84	192 ± 15
Apr. 2, 1995	9809.017	20.67	4.14	56 ± 8	Mar. 3, 1996	10145.634	19.65	3.81	147 ± 14
Apr. 2, 1995	9809.787	23.33	4.11	51 ± 6	Mar. 4, 1996	10146.019	19.65	3.85	114 ± 13
Apr. 2, 1995	9809.851	23.07	4.08	51 ± 6	Mar. 4, 1996	10146.659	16.32	3.58	169 ± 16
Apr. 3, 1995	9810.877	23.60	4.13	16 ± 5	Mar. 5, 1996	10146.980	15.92	3.64	151 ± 16
Apr. 5, 1995	9812.799	19.60	3.50	36 ± 4	Mar. 5, .1996	10147.878	15.90	3.59	133 ± 14
Apr. 25, 1995	9832.548	11.33	6.34	107 ± 19	Sep. 20, 1996	10346.269	21.73	3.85	182 ± 12
Apr. 26, 1995	9833.771	23.07	4.22	150 ± 7	Sep. 21, 1996	10346.884	12.78	3.76	186 ± 13
Apr. 27, 1995	9834.668	23.60	4.25	121 ± 6	Feb. 23, 1997	10502.026	15.92	4.33	184 ± 15
Apr. 29, 1995	9836.400	19.33	4.36	131 ± 7	Feb. 24, 1997	10503.116	15.92	4.21	174 ± 13
Apr. 30, 1995	9837.362	20.00	4.32	91 ± 6	Apr. 5, 1999	11273.572	16.00	3.42	87 ± 3
Apr. 30, 1995	9837.426	18.80	4.27	104 ± 6	June 27, 1999	11356.643	9.98	4.07	85 ± 8

the TTM field of view (at about 7° from the optical axis), where the event recording efficiency is much lower than at the center. For the same reason, the errors in Fig. 2 differ significantly in different TTM sessions, and in the two sessions of September 9, 1989 (MJD $\sim$ 7778), the upper limits on the flux are so large.

The ASM data for 1996–1998 revealed a period of $\approx$38 days in the light curve of KS 1731–260 (Revnivtsev and Sunyaev 2001). Unfortunately, the TTM data do not allow this periodicity to be verified, because the mean time interval between individual TTM observations is too long (more than 38 days). Nevertheless, we searched for a periodicity in the accessible frequency range (5×10^{-4}–0.0185 days^{-1}) by using the periodogram technique of Lomb (1976) and Scargle (1982). The derived periodogram is shown in Fig. 4. The variability is clearly present (above the thresholds shown in the figure), but it is aperiodic. We found no evidence of a periodic X-ray variability in KS 1731–260 on time scales from 50 days to 5 years.

THE SOURCE SPECTRUM

The statistical significance of the source spectra obtained in each individual TTM observing session is low and insufficient for a qualitative spectral analysis. To increase the statistics, we averaged the observations close in time and in recorded flux. Three sessions of April 2, 1995 (MJD $\sim$ 9809), with a mean flux of $\sim$55 mCrab (low state) and four sessions of March 17–20, 1994 (MJD 9428–9431), with a mean flux of

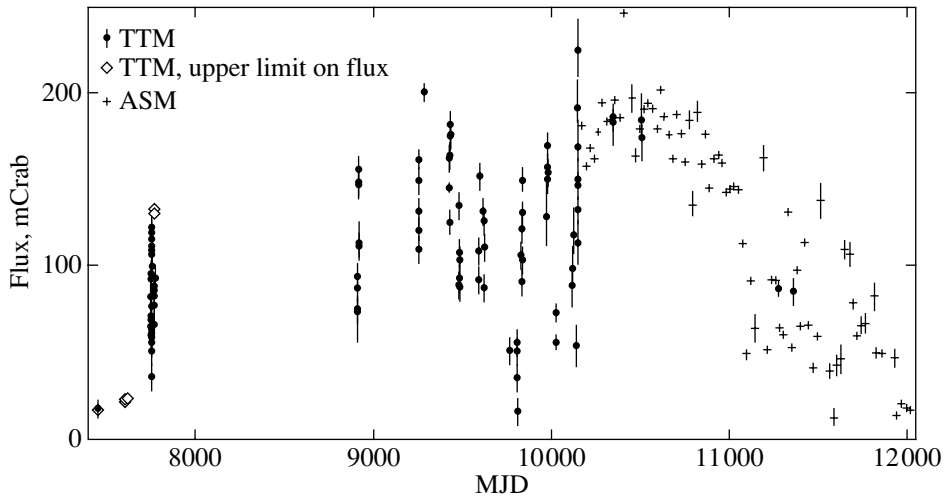

Fig. 2. The light curve of the burster KS 1731–260 for 1988–2001, as constructed from the TTM 2–27 keV and ASM 2–12 keV data. Upper limits (3σ) on the source flux during the TTM sessions when the burster was within its field of view but was not detected are also indicated.

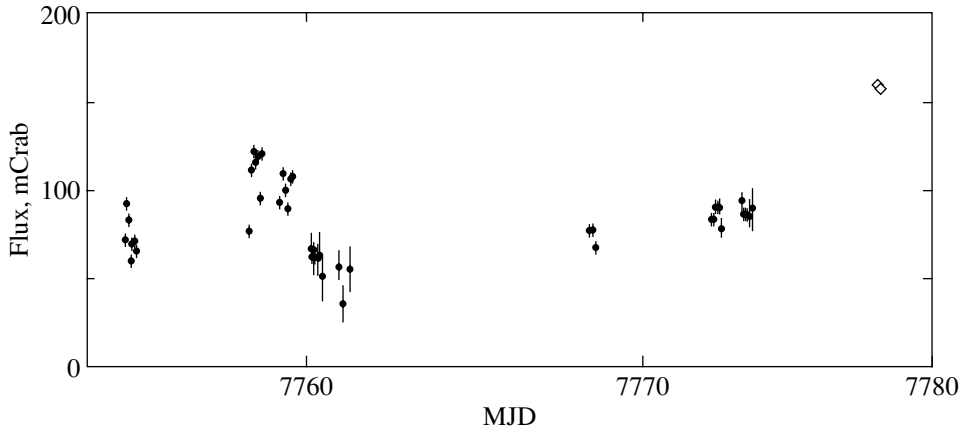

Fig. 3. Part of the light curve shown in Fig. 2 for the TTM sessions of August 22–23, 1989.

~170 mCrab (high state) meet these requirements best. Figure 5 shows the spectra taken in these sessions and the PCA/RXTE data for the high (July 14, 1996) and low (October 2, 1998) states. We see from the figure that the spectral shape of the source strongly depends on its mean flux. Similar spectral states were also obtained when analyzing the RXTE data.

The TTM energy spectrum of KS 1731–260 in its high state (at an X-ray flux of ~170 mCrab from the source) can be described by the bremsstrahlung model of an optically thin plasma (the bremss model in the XSPEC package) with a temperature of ~5–6 keV (see also Sunyaev 1989). However, the two-component model (White *et al.* 1988) is a physically more realistic spectral model of the source in this state. One component in this model is the radiation from a standard optically thick accretion disk (Shakura and Sunyaev 1973), and the other component is the radiation from the matter accreted onto the neutron-star surface or the boundary-layer radiation. Tenma (Mitsuda *et al.* 1984), EXOSAT (White *et al.* 1988), Ginga (Tanaka 1992), RXTE, and other observations of X-ray binaries with neutron stars did reveal these two components in the spectra of accreting neutron stars (Tanaka and Shibazaki 1996). Unfortunately, however, the statistical significance of the TTM spectra is too low for these components to be clearly separated. Note that, because of the low statistical significance of the source spectra, we fixed the interstellar absorption column density toward the source at $N_{\rm HL} = 2 \times 10^{22}$ obtained by the ROSAT observatory (Barret *et al.* 1998).

In the low spectral state (at an observed 2–27 keV X-ray flux of ~55 mCrab), when the observed spectrum is fitted by the bremsstrahlung model, the tem-

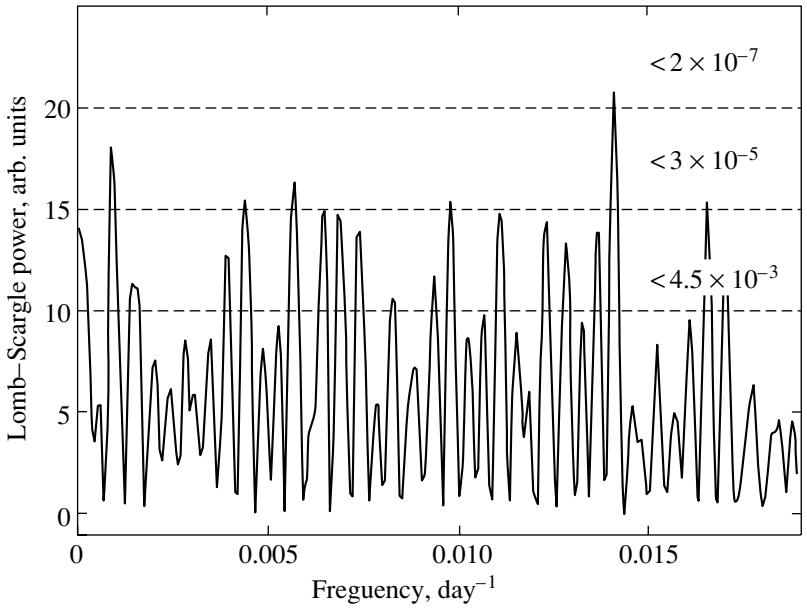

Fig. 4. The Lomb–Scargle periodogram constructed from the TTM data for 1988–1999. The dashed lines indicate the levels that correspond to the following probabilities of random deviations of the powers: 4.5×10^{-3}, 3×10^{-5}, and 2×10^{-7}, respectively.

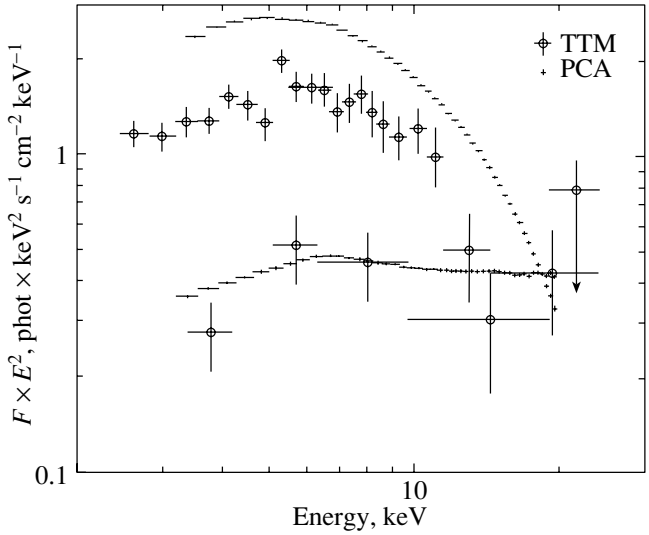

Fig. 5. The high- and low-state energy spectra of KS 1731–260 constructed from the TTM and PCA data

perature parameter increases to 10 keV and has virtually no upper TTM limit. A similar low/hard spectral state of the source was observed by the RXTE observatory, for example, on October 2, 1998 (Fig. 5). Thus, the TTM data confirm the bimodal behavior of KS 1731–260, which is similar to that observed for the sources 4U 1705–44, 4U 1608–52, GX 354–0, Terzan 1, etc. (Barret *et al.* 2000; Pavlinsky *et al.* 2001). Note that the SIGMA telescope, which detected hard (50–150 keV) X-ray emission from this burster in 1991 (Barret *et al.* 1992), to all appearances observed KS 1731–260 precisely in the low/hard spectral state.

DISCUSSION

Here, we presented the long-term TTM observations of the X-ray burster KS 1731–260. As was already noted above, the light curve of the source over a period of ~11 years exhibits an interesting pattern: the higher the mean flux from the source (averaged, e.g., over three or four months), the lower its variability amplitude. This is particularly clearly seen during

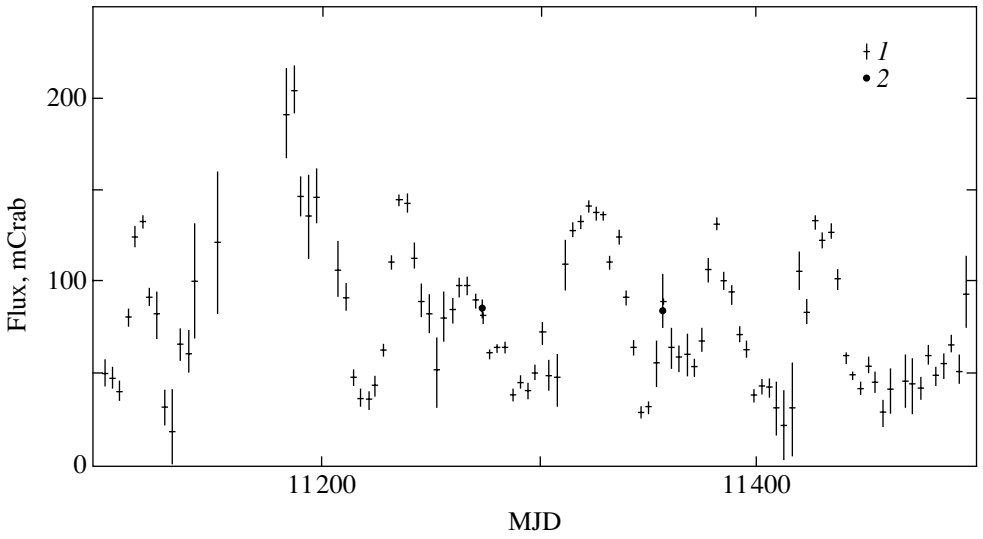

Fig. 6. The ASM/RXTE 2–12 keV light curve of KS 1731–260 from October 1998 through November 1999: (*1*) the ASM data averaged over ~3 days; (*2*) the TTM 2–27 keV data.

1996–2001, because the ASM flux measurements are much more regular than the TTM flux measurements for the source. We see erratic flux variations in the source on a time scale of several months (Fig. 6).

In this connection, note the long-period variability model for X-ray sources in low-mass X-ray binaries proposed by Meyer and Meyer-Hofmeister (1990). These authors showed that when the far parts of the accretion disk are significantly irradiated by an intense central X-ray source, the so-called diffusive instability could arise. At a stable rate of mass outflow from the surface of the companion star in a binary system, quasi-periodic variations in the accretion rate can arise inside the accretion disk. This is because there is a positive feedback between the accretion-rate variations in the disk and the irradiation of its outer parts. Meyer and Meyer-Hofmeister (1990) showed this regime to arise only at certain accretion rates ($\sim 10^{-9}$–$10^{-11} M_\odot$ per year); at higher accretion rates, the diffusive instability is quenched.

Note that we see a similar behavior in the long-period variability of KS 1731–260. Given that the distance to the source is ~8 kpc (Smith *et al.* 1997), its luminosity (10^{36}–10^{37} erg s^{-1}) roughly corresponds to the accretion rates at which the diffusive instability can arise. At a mean flux of ~50–100 mCrab from the source, we observe significant flux variations on time scales of several months, while at a mean flux of ~200 mCrab, these large variations disappear. For the typical neutron-star accretion rates and accretion-disk sizes from Meyer and Meyer-Hofmeister (1990), we obtained the characteristic period of the variations attributable to diffusive instability, ~20–50 days; i.e., it roughly corresponds to the time scales observed for KS 1731–260.

Another peculiarity of KS 1731–260 is the existence of two (hard and soft) spectral states that correspond to different fluxes from the source. KS 1731–260 was in the hard spectral state at a low flux (up to 50 mCrab) and passed to the soft spectral state at a flux above ~100 mCrab. Such bimodal behavior of sources in binary systems is commonly encountered both in black-hole candidates and in neutron stars. Therefore, we may assume that such behavior is related to intrinsic accreted-flow parameters rather than to accreting-object properties.

ACKNOWLEDGMENTS

We wish to thank M.R. Gilfanov and E.M. Churazov, who kindly permitted us to use their TTM data processing software, and V.G. Rodin, A.V. Prudkoglyad, and the staff of the Flight Control Center, who controlled the satellite and the instrumentation. We are also grateful to A.N. Anenkova for preliminary data preparation. This study was supported in part by the Program "Astronomy: Nonstationary Astronomical Objects" of the Russian Academy of Sciences and the Russian Foundation for Basic Research (project no. 00-15-96649).

REFERENCES

1. D. Barret, L. Bouchet, P. Mandrou, *et al.*, Astrophys. J. **394**, 615 (1992).
2. D. Barret, C. Motch, and P. Predehl, Astron. Astrophys. **329**, 965 (1998).
3. D. Barret, J. F. Olive, L. Boirin, *et al.*, Astrophys. J. **533**, 329 (2000).

4. A. C. Brinkman, J. Dam, W. A. Mels, *et al.*, in *Non-thermal and Very High Temperature Phenomena in X-ray Astronomy,* Ed. by G. C. Perola and M. Salvati (Institute Astronomico, Rome, 1983), p. 263.
5. E. Kuulkers, J. J. M. in't Zand, M. H. van Kerkwijk, *et al.*, astro-ph/0111261 (2001).
6. N. R. Lomb, Astrophys. Space Sci. **39**, 447 (1976).
7. F. Meyer and E. Meyer-Hofmeister, Astron. Astrophys. **239**, 214 (1990).
8. K. Mitsuda, H. Inoue, K. Koyama, *et al.*, Publ. Astron. Soc. Jpn. **36**, 741 (1984).
9. J. A. Orosz, C. D. Bailyn, and K. Whitman, Astron. Telegram, No. 75 (2001); http://atel.caltech.edu.
10. M. N. Pavlinsky, S. A. Grebenev, A. A. Lutovinov, *et al.*, Pis'ma Astron. Zh. **27**, 345 (2001) [Astron. Lett. **27**, 297 (2001)].
11. M. Revnivtsev and R. Sunyaev, astro-ph/0108120 (2001).
12. J. D. Scargle, Astrophys. J. **263**, 835 (1982).
13. N. I. Shakura and R. A. Suniaev, Astron. Astrophys. **24**, 337 (1973).
14. D. A. Smith, E. H. Morgan, and H. Bradt, Astrophys. J. Lett. **479**, L137 (1997).
15. R. Sunyaev, IAU Circ., No. 4839 (1989).
16. R. A. Sunyaev, M. R. Gilfanov, E. M. Churazov, *et al.*, Pis'ma Astron. Zh. **16**, 136 (1990) [Sov. Astron. Lett. **16**, 59 (1990)].
17. Y. Tanaka, in *Ginga Memorial Symposium, ISAS, Sagamihara, 1992,* Ed. by F. Makino and F. Nagase, p. 19.
18. Y. Tanaka and N. Shibazaki, Annu. Rev. Astron. Astrophys. **34**, 607 (1996).
19. N. E. White, L. Stella, and A. N. Parmar, Astrophys. J. **324**, 363 (1988).
20. R. Wijnands, P. J. Groot, J. Miller, *et al.*, Astron. Telegram, No. 72 (2001); http://atel.caltech.edu.

Translated by V. Astakhov

Astronomy Letters, Vol. 28, No. 5, 2002, pp. 287–295. Translated from Pis'ma v Astronomicheskiĭ Zhurnal, Vol. 28, No. 5, 2002, pp. 331–340.

Statistics of Faint Gamma-Ray Bursts from the GRIF Experiment on the Mir Orbiting Station

M. I. Kudryavtsev[1], S. I. Svertilov[2*], and O. V. Morozov[2]

[1] *Space Research Institute, Russian Academy of Sciences, ul. Profsoyuznaya 84/32, Moscow, 117810 Russia*

[2] *Institute of Nuclear Physics, Moscow State University, Vorob'evy gory, Moscow, 119899 Russia*

Received October 24, 2001

Abstract—During the GRIF experiment onboard the Mir orbiting station, cosmic gamma-ray bursts (GRBs) were observed in the photon energy range 10–300 keV. We developed a technique for selecting events, cosmic GRB candidates, based on output readings from the PX-2 scintillation spectrometer, the main astrophysical instrument. Six events interpreted as cosmic GRBs were identified at a threshold sensitivity level of $\geq 10^{-7}$ erg cm^{-2}. The GRIF burst detection rate recalculated to all the sky is $\sim 10^3$ yr^{-1} (fluence $\geq 10^{-7}$ erg cm^{-2}). This rate matches the BATSE/CGRO estimate and significantly differs from the value predicted by the $S^{-3/2}$ dependence, which holds for a spatially uniform source distribution. The GRB detection rate at low peak fluxes is compared with the results of analysis for BATSE/CGRO "nontriggered" events and with predictions of major cosmological models. We conclude that the PX-2 observational data on faint cosmic GRBs are consistent with predictions of models with the highest frequency of GRB occurrence at $z \geq 1.5$–2. © *2002 MAIK "Nauka/Interperiodica".*

Key words: *X-ray and gamma-ray sources, spaceborne observatories, cosmic gamma-ray bursts, star formation, compact-object mergers*

INTRODUCTION

Despite the progress in studying cosmic gamma-ray bursts (GRBs) through observations of radio, optical, and X-ray afterglows (Costa *et al.* 1997; van Paradijs *et al.* 1997; Frail *et al.* 1997), the cosmological nature of GRBs requires further confirmation. For some events, the cosmological redshift z is known to have been measured either for the corresponding optical transient or for the so-called host galaxy in which the GRB source is assumed to be located (Metzger *et al.* 1997; Kulkarni *et al.* 1998; Djorgovski *et al.* 1998). This was compelling evidence for the cosmological models of GRBs, according to which their sources lie at great distances. However, the main problem of currently available cosmological models for GRBs is the need to explain the large spread in luminosities in the source for events with identified host galaxies. If the identification is correct, then no correlation of fainter bursts with more distant objects shows up, which would have to be the case for standard-candle sources. The spread in luminosities in the source is many orders of magnitude, from $\sim 10^{47}$ to $\sim 10^{54}$ erg s^{-1}, which may suggest that the GRB population is not homogeneous; i.e., individual events could be different in nature.

Information that is important in understanding the physical processes in GRB sources can be obtained from their spatial distribution and the luminosity distribution in the source. Before the launch of the BeppoSax spaceborne observatory (see, e.g., Feroci *et al.* 1997), during the flight of which the first afterglow is known to have been discovered, such information could only be obtained by analyzing statistical GRB characteristics, such as the source sky distribution and the observed intensity or fluence distribution (the so-called $\log N$–$\log S$ distribution). A comparison of these distributions can yield information on the source spatial distribution. In particular, through such an analysis of the cosmic GRB observations in the KONUS experiments on the Venera spacecraft (Masetz and Golenetski 1981) and, subsequently, in the BATSE experiment on the Compton gamma-ray observatory (CGRO) (Meegan *et al.* 1992, 1996), the GRB sources were found to form a spherically symmetric, spatially bounded population. This population fits neatly into the picture predicted by most currently available cosmological models. Based on the observed intensity distribution and using the specified source spatial distribution, we can obtain information on the intrinsic luminosity in the source and optimize the parameters of the model that describes the GRB intrinsic-luminosity

*E-mail: sis@srdlan.npi.msu.su

distribution (Fenimore *et al.* 1993; Rutledge *et al.* 1995; Hakkila *et al.* 1996). Analysis of statistical characteristics for cosmic GRBs, in particular, the $\log N$–$\log S$ distributions, is still of current interest. The redshifts of the GRB sources were determined for only a few events. At the same time, statistical characteristics provide information on the population of GRB sources as a whole. In addition, if the cosmological model is valid, then statistical characteristics can be used to obtain information on the processes at early evolutionary stages of the Universe. In particular, the observed intensity distribution of GRBs reflects the redshift z distribution of their sources. Thus, the history of global star formation in the Universe can be traced by using this distribution (Totani 1997; Wijers *et al.* 1998; Krumholz *et al.* 1998; Mao and Mo 1998). The idea that GRBs are related to neutron-star or black-hole mergers, whose probability is determined by the star-formation rate as a whole, underlies this hypothesis. In this respect, an analysis of the $\log N$–$\log S$ distributions at low fluences, $S \leq 10^{-7}$ erg cm^{-2}, is of particular interest. According to some data, the observed fluences $S \sim 10^{-7}$ erg cm^{-2} correspond to $z \geq 1$ or even $z \geq 3$ (Wijers *et al.* 1998). Therefore, the detection rate of faint GRBs may also be of critical importance both for the cosmological models of their sources and for the models of primordial star formation in the Universe.

The best current data on GRB statistics are known to have been obtained in the BATSE CGRO experiment (Paciesas *et al.* 2001). However, the above fluence $S \sim 10^{-7}$ erg cm^{-2} is close to the BATSE GRB detection threshold. Therefore, in light of the above discussion, it seems necessary to use all possibilities to independently estimate the detection rate of faint GRBs. In this paper, we present the GRIF observations of cosmic GRBs on the Mir orbiting station and estimate the detection rate of events with fluences $S \geq 10^{-7}$ erg cm^{-2}.

EXPERIMENTAL CONDITIONS

The GRIF experiment was carried out on the Spectrum module of the Mir station (an average altitude of ~400 km, an orbital inclination of 51°, and a revolution period of ~90 min) from October 1995 through June 1997. Its objectives covered both astrophysical observations (cosmic GRBs, X-ray binaries, and pulsars) and analysis of the spatial distributions and variations of charged-particle and neutron fluxes in circumterrestrial space (Kudryavtsev *et al.* 1995, 1996; Bogomolov *et al.* 1997), as well as methodological issues related to the background in gamma-ray astronomical experiments (Bogomolov *et al.* 1999, 2000).

The GRIF instrumentation included four instruments:

(1) The PX-2 oriented hard X-ray and gamma-ray scintillation spectrometer (the observed photon energy range $\Delta E_\gamma = 10$–300 keV, the effective area $S \sim 300$ cm^2, and the field of view $\Omega \sim 1$ sr). The instrument was designed mainly for astrophysical observations, including patrols of solar flare activity.

(2) The NEGA-1 omnidirectional gamma-ray and neutron spectrometer ($\Delta E_\gamma = 0.15$–50 MeV, $E_n > 20$ MeV, $S_\gamma \sim 250$ cm^2, $S_n \sim 20$ cm^2). The instrument was designed to study the background gamma-ray and neutron fluxes on Mir orbits.

(3) The FON-1 charged-particle spectrometer ($\Delta E_e = 40$–500 keV, $\Delta E_p = 1$–3 MeV) with a large geometric factor, $\Gamma \sim 80$ cm^2 sr. The instrument was designed to measure low charged-particle fluxes outside the Earth's radiation belts.

(4) The FON-2 charged-particle spectrometer ($\Delta E_e = 0.04$–1.5 MeV, $\Delta E_p = 2$–200 MeV) with a small geometric factor, $\Gamma \sim 0.5$ cm^2 sr. The instrument was designed to measure high charged-particle fluxes in the radiation belts.

The PX-2 data were used to search for and analyze hard X-ray and gamma-ray bursts from astrophysical objects. The PX-2 instrument consisted of seven identical detector units and an electronic data processing and transformation system. The main recording element in each detector unit was a CsI(Na) crystal (0.35 cm in thickness, 8.0 cm in diameter). Passive shield was used to suppress the background X-ray and gamma-ray radiation. This shield included an azimuthally symmetric lead collimator, as well as lead (8 cm in diameter, 1.0 cm in thickness) and barium (8 cm in diameter, 0.5 cm in thickness) glasses that absorbed the local radiation from the spacecraft (the barium glass was intended to absorb the characteristic X-ray radiation from lead). The recording of charged particles by the PX-2 detector units was eliminated by the phoswich method: the main detector, the passive shield elements, and the collimator were placed under an anticoincidence cup made of plastic scintillator, which was viewed (from the lead glass) by the same photomultiplier as the CsI(Na) crystal. The events related to the recording of charged particles in the plastic scintillator were identified by analyzing the time profile of the photomultiplier output current pulse. When the photomultiplier output signal contained a short (~5 ns duration, which corresponds to the characteristic decay time of the plastic scintillator) component of sufficient intensity, a special electronic circuit generated a logic inhibit signal, which was fed to the anticoincidence circuits. The triggering threshold of this phoswich circuit was chosen to ensure that no charged particles would be

recorded in the entire PX-2 energy range from 10 to 300 keV with 99% efficiency. The count rate of inhibit signals was measured in a separate charged-particle channel.

During the entire experiment, we measured the 5-s-averaged count rates of X-ray photons in the energy ranges 10–50, 25–50, 50–100, 100–200, and 200–300 keV and of accompanying charged particles. Additional data output was provided in the 10–50, 25–50, and 50–100 keV channels, which made it possible to measure the count rates with a time resolution of 2.5 s.

Each PX-2 detector unit had a wide ($\sim$0.7 sr) field of view. Its beam formed by the azimuthally symmetric collimator was isotropic in azimuthal angle and linearly fell off from maximum ($\theta = 0°$) to zero ($\theta = 45°$) in offset from the detector axis.

A major peculiarity of the GRIF experiment was the possibility of simultaneously monitoring all the principal components of the background-producing emissions in circumterrestrial space on Mir orbits. In particular, the sensitive FON-1 electron detector was used to check the sporadic increases in X-ray flux attributable to the recording of bremsstrahlung from precipitating energetic magnetospheric electrons, which could imitate cosmic GRBs. Having a large geometric factor, FON-1 could detect even relatively small electron flux variations outside the zones of trapped radiation.

THE OBSERVING TECHNIQUE FOR COSMIC GRBs IN THE GRIF EXPERIMENT

The PX-2 detector units were positioned on the external panel of the Mir module in such a way that six units were located symmetrically around one central (seventh) unit. The axes of all seven detectors were separated by 5°. This arrangement and the large field of view of each detector unit, on the one hand, provided an overlap (within 35° of the central-detector axis) of the fields of view of all units (in practice, this made it possible to use the total working area of all detectors when observing a given source) and, on the other hand, allowed the angular coordinates of sources to be estimated by a comparative analysis of the output data from individual detectors. Thus, the total field of view of the entire instrument was $\sim$1 sr.

The PX-2 instrument was rigidly fixed to the module surface in such a way that the axis of its central detector (which coincided with the axis of the entire instrument) made an angle of 45° both with the Spectrum axis (the Mir $-Y$ axis) and with the Mir principal ($+X$) axis. During the flight, there were two main orientation modes: stabilization along three axes and orbital (gravitational) mode. In the former case, the Mir axes (and, accordingly, the PX-2 axes) had a fixed direction in space; i.e., the instrument was directed toward a fixed point in the sky. The angle between the PX-2 axis and the nadir–zenith direction along the orbital turn varied over the range 0° (the direction toward zenith, i.e., the sky) to 180° (the direction toward nadir, i.e., the Earth), and, accordingly, the PX-2 field of view was regularly eclipsed by the Earth. For this orientation, the effective sky exposure time by the entire PX-2 field of view was, on average, half the turn (the PX-2 field of view was not shadowed during $\sim$1/4 of the turn; subsequently, during 1/2 of the turn, the fraction of the unshadowed part almost uniformly decreased from 100% to 0). In the latter case, the PX-2 axis was always directed at 45° to the zenith–nadir axis (i.e., the field of view of some of the detectors was shadowed by the Earth's atmosphere only slightly), and it slowly turned in space with the Mir station during the flight in each turn. Thus, the sky was slowly ($\sim 4°$ min^{-1}) scanned. During the entire experiment, various regions of the sky, including the Galactic-anticenter region, areas offset from the Galactic equator, and the Galactic-center region, could be observed.

Information was transmitted to the Earth, as a rule, in 16-h-long sessions of continuous observations; the interval between them typically ranged from several hours to several days. A total of 200 sessions were conducted during the experiment, from which $\sim$150 were chosen for the subsequent analyses (sessions with many telemetry failures, incorrect write times of output data, and the like were filtered out). Given the duration of the observations under the above conditions of different PX-2 orientations in individual sessions and that some of the observing time in each turn was spent on the regions of captured radiation (the corresponding output data were excluded from the subsequent analysis), the total effective sky exposure time by the entire PX-2 field of view was $\sim$850 h.

The GRIF possibilities to detect cosmic GRBs can be evaluated from background readings in various PX-2 channels. The threshold count M that corresponds to GRB detection can be determined from the formula

$$M = n\frac{\sqrt{N\Delta t}}{S_{\text{eff}}}, \qquad (1)$$

where n is the chosen number of standard deviations (σ); N is the background count rate, in counts s^{-1}; Δt is the length of the time interval in which the events were selected; and S_{eff} is the PX-2 effective area. The 5σ criterion was chosen for GRB selection. For the measured background count rates N $\sim$100 counts s^{-1} in the energy range 25–100 keV, $\Delta t = 5$ s, and $S_{\text{eff}} = 300$ cm^2, we have M

$\sim$0.35 counts cm^{-2}. Based on the derived threshold count, we can estimate the corresponding threshold fluences S_T. For a burst with a standard duration of 5 s (i.e., ignoring the corrections attributable to the shape of the actual time profiles) and with an optically thin plasma spectrum,

$$\frac{dJ}{dE} = J_0 \left(\frac{E_0}{E}\right) \exp\left(-\frac{E}{kT}\right), \qquad (2)$$

and given the mean detector efficiency in the energy range 25–100 keV ($\sim$75%), S_T are 4×10^{-8} erg cm^{-2} ($kT = 50$ keV) and 10^{-7} erg cm^{-2} ($kT = 200$ keV). These estimates were made for the most favorable observing conditions, i.e., by disregarding the reduction in the effective exposed detector area when photons are recorded from sources offset from the PX-2 axis.

Our estimates lead us to conclude that, in comparison with the BATSE experiment, lower threshold peak fluxes and fluences during the burst were achieved in the PX-2 experiment, particularly for soft ($kT < 50$ keV) bursts. This is mainly attributable to the following three factors: first, the use of relatively thin (0.35 cm) CsI(Na) crystals as the detecting elements in the PX-2 instrument, which provided a low level of intrinsic noise and which allowed the detection energy threshold to be significantly reduced (down to 10 keV) compared to BATSE; second, the use of a combination of active and passive shield, which allowed the PX-2 instrumental background to be considerably reduced; and, third, the introduction of a collimator, which also reduced the background count rate in the event selection channels.

RESULTS AND DISCUSSION

Apart from the 5σ criterion for the peak 25–100 keV intensity, we used the following two additional conditions when selecting candidates for astrophysical bursts: (1) an increase in the X-ray channels should not be accompanied by an increase in the accompanying electron fluxes, and (2) a statistically significant increase in the count rate must be recorded by at least two of the seven detectors. The first condition eliminated the imitations of astrophysical X-ray and gamma-ray bursts by bremsstrahlung from precipitating magnetospheric electrons. As was pointed out above, such precipitations were checked with the FON-1 sensitive energetic-electron detector, which could record electron fluxes with energies of several hundred keV at a level of $\geq 10^{-1}$ cm^{-1} s^{-1} sr^{-1} in all segments of the Mir orbit outside the zones of captured radiation. The second condition removed the burst imitations attributable to the exposure of the scintillation crystals to strongly ionized particles, mostly heavy nuclei (since the arrangement of the PX-2 detectors is virtually planar, the probability of nucleus passage through at least two detectors is negligible).

As a result, we selected several tens of events that satisfied the above criteria for which the spectral representation (2) was chosen. To determine the parameter kT, the peak flux I_i in a given energy range, and the spectral flux density at a given energy $J(E = E_0)$, we computed the special instrumental functions that related the spectral parameters and count rates N_i in different PX-2 channels:

$$\frac{N_i}{N_j} = F(kT), \quad I_i = N_i \Phi(kT), \qquad (3)$$
$$J(e = E_0) = N_i \Psi(kT).$$

Functions (3) were determined by modeling the transformations of the initial spectra (2) in the instrument for various kT. The function $F(kT)$ allows the spectral parameter kT to be determined from the ratio of the count rates in adjacent energy ranges. The functions $\Phi(kT)$ and $\Psi(kT)$ relate the peak intensity in a given energy range and the spectral flux density at a certain energy to the count rates in the PX-2 channels for the specified spectral representation. Selected bursts unrelated to charged particles are characterized by kT in a wide range from $\sim$5 to $\sim$500 keV. Since the single (i.e., unrelated to recurrent soft gamma-ray repeater sources) GRBs that constitute the main population of events recorded both in the BATSE CGRO experiment and in most other experiments (e.g., KONUS) are characterized by $kT \geq 30$–40 keV in the spectral representation (2); below, we call the bursts with such spectra conventional. Therefore, we chose the condition $kT \geq 40$ keV as the main parameter for selecting candidates for conventional GRBs in the experiment under consideration. A total of six such events were recorded. The solar origin of these bursts can be ruled out, because no manifestations of solar flaring activity were observed when the events were recorded (Coffey 2001). The main GRB parameters are given in the table.

In those cases where an event was covered by one bin in the time series (i.e., its duration was < 5.1 s), we estimated the duration by comparing the count rates measured by the following two independent methods: using a digital-to-analog converter whose output readings directly gave the number of counts in a specified time interval ($N_{\rm DAC}$) and using a log-counting ratemeter (frequency meter) whose readings $N_{\rm RATE}$ are related to $N_{\rm DAC}$ by $N_{\rm RATE} = N_{\rm DAC}(1 - \exp(-\Delta t/\tau))$, where Δt is the duration of the increase and $\tau \sim 5$ s is a parameter that characterizes the temporal properties of the ratemeter.

The fluence $S(>25$ keV) was determined from the spectral flux density at energy 25 keV integrated over

Table

Burst detection date, UT	Duration, s	kT, keV	Fluence at >25 keV, erg cm^{-2}	Peak 50–300 keV flux, phot. cm^{-2} s^{-1}	Burst detection date in other experiments
951108 $11^h35^m03^s$	~8.7	70 ± 30	$(1.0 \pm 0.4) \times 10^{-7}$	$(6.0 \pm 1.2) \times 10^{-2}$	–
951111 $09^h42^m06^s$	15–20	500 ± 200	$(2.1^{+2.0}_{-1.0}) \times 10^{-5}$	$(3.4^{+3.4}_{-1.7}) \times 10^{0}$	KONUS WIND, 951111 $09^h42^m40^s$
960117 $07^h45^m46^s$	~1.4	60 ± 10	$(1.7^{+1.7}_{-0.8}) \times 10^{-5}$	$(4.8^{+4.8}_{-2.4}) \times 10^{1}$	–
960123 $12^h06^m42^s$	~20.4	300 ± 100	$(5.0 \pm 1.0) \times 10^{-6}$	$(1.8 \pm 0.1) \times 10^{0}$	KONUS WIND, 961123 $12^h07^m21^s$ BATSE CGRO (nontriggered event), 961123 $12^h07^m18^s$
960128 $18^h18^m13^s$	~2.2	125 ± 40	$(1.9 \pm 0.6) \times 10^{-7}$	$(2.0 \pm 0.2) \times 10^{-1}$	–
970601 $19^h19^m02^s$	~51	100 ± 10	$(3.5 \pm 2.0) \times 10^{-5}$	$(2.7 \pm 1.6) \times 10^{0}$	KONUS WIND, 970601 $19^h19^m30^s$

the burst duration and from the parameter kT. For a more accurate determination of S, we estimated the offset θ of the burst sources from the PX-2 axis. The ratio of the dispersion σ_i of count rates measured from the readings of individual detectors to the value of $\bar{N}$ averaged over all detectors may be used as a measure of this offset. This ratio was calculated for various offsets and various azimuthal directions by assuming that the difference between the readings of individual detectors was attributable to geometric factors alone (different relative exposed areas). After averaging over the various azimuthal directions, we derived the function $\sigma_i/\bar{N}(\theta)$ that was used to determine the offset θ.

As follows from the table, among the selected GRB candidates, at least three were observed in other experiments: BATSE CGRO (Kommers *et al.* 2001) and KONUS WIND (Golenetski 2001). Among these events, GRB 970601 with a distinct time structure deserves particular attention. The corresponding time profiles in different PX-2 and NEGA channels are shown in Fig. 1. As we see from the figure, this burst consisted of two consecutive peaks of approximately equal intensity spaced ~25 s apart. The second peak exhibits a slower decay, while the first peak is virtually symmetric. For the time intervals marked by numbers in Fig. 1, we constructed the mean energy spectra from the PX-2 and NEGA data (see Fig. 2). It follows from Fig. 2 that the spectra of both peaks at energies >100 keV clearly show nonthermal components, which can be fitted by a power law. The first peak is characterized by a harder spectrum in the energy range 0.1–1.0 MeV.

The number of GRBs detected with the PX-2 instrument can be used to estimate the expected detection rate of faint GRBs (with fluences $\leq 10^{-7}$ erg cm^{-2}) in all the sky. To this end, we calculated the function that characterizes the GRB detection efficiency in all the sky during the experiment:

$$\varepsilon(S) = \int \varepsilon_T(S, kT) f(kT) d(kT) = \varepsilon_{kT}(\eta). \quad (4)$$

Here, $\eta \equiv S_T/S$, S is the fluence, S_T is the threshold fluence, $f(kT)$ is the burst distribution in spectral parameter kT [the KONUS data were used (Masetz *et al.* 1981)], and $\varepsilon_T(S, kT)$ is the detection probability of a burst with a given spectral shape (kT) and fluence S integrated over its duration. The dependence $\varepsilon_T(S, kT)$ can be represented as $\varepsilon_T(S, kT) = \varepsilon_T(S/S_T) \times F(S_T/S)$, where $F(S_T/S) \equiv F(\eta)$ is the PX-2 beam and the function $\varepsilon_T(S/S_T)$ is determined by the event-selection efficiency (most of the recorded bursts with duration $\leq$10 s were actually selected by their fluence) and the detector efficiency. It should be noted that the dependence of the detection efficiency $\varepsilon_T(S/S_T)$ on kT is actually contained in the threshold fluence, which is largely determined by the spectral hardness of the recorded burst. Examples of the functions $\varepsilon_T(S, kT)$ that characterize the detection efficiency of bursts with various kT and the kT-averaged dependence (4) are shown in Fig. 3.

To estimate the GRB detection rate in all the sky per year $N(>S)$ from the PX-2 distribution in observed fluence $N^*(>S^*)$, the burst detection efficiency (4) in the entire sky during this experiment should be taken into account. The following relation between the $N(>S)$ and $N^*(>S^*)$ distribution can be written:

$$N^*(>S^*) = (\Delta T/\text{year}) \quad (5)$$

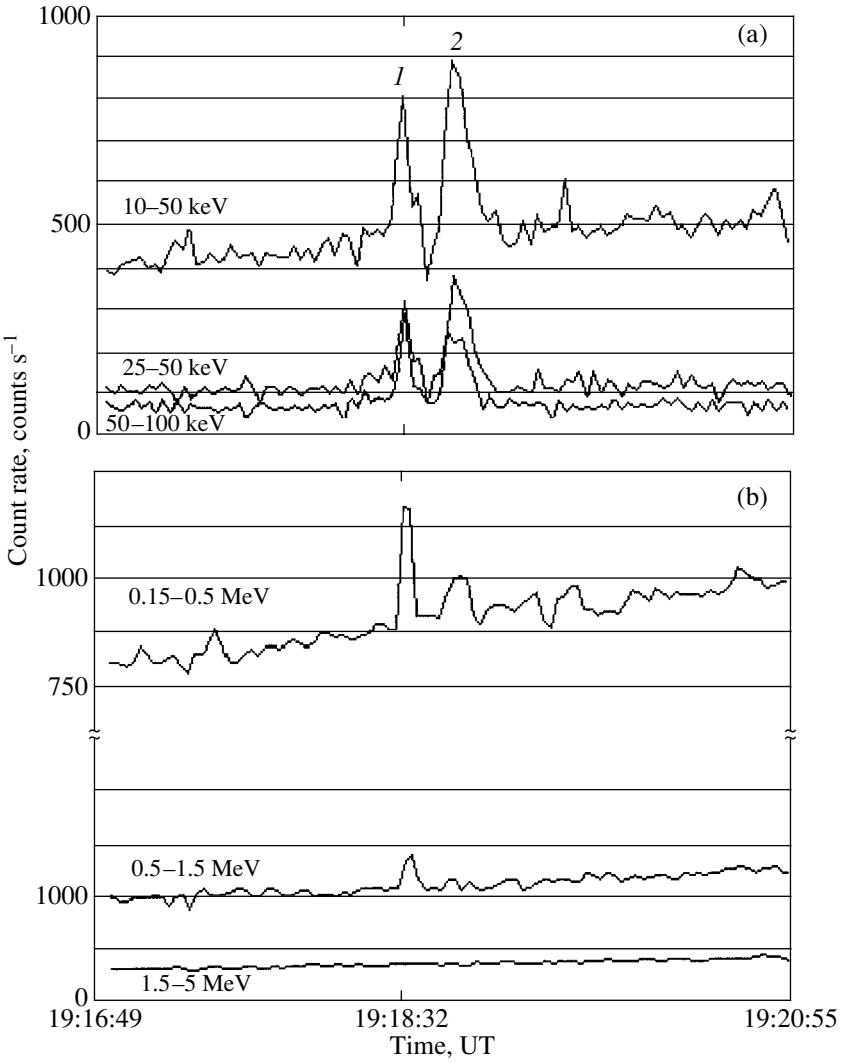

Fig. 1. Time profiles for GRB 970601 in various (a) PX-2 and (b) NEGA energy ranges. The numbers mark the averaging intervals for which the energy spectra were constructed.

$$\times \iint \varepsilon_{kT}(\eta) N(>S) \delta(S^* - \eta S) dS d\eta$$
$$= (\Delta T/\text{year}) \int \varepsilon_{kT}(\eta) N(>S^*/\eta) d\eta.$$

Here, $\Delta T \sim 850$ h is the total exposure time in the experiment; η ranges from 0 to 1. Clearly, to reconstruct the initial $N(>S)$ distribution generally requires solving the inverse problem, i.e., the integral equation (5). Note that, as we see from Fig. 3, dependence (4) may well be fitted by a threshold function of the type $\varepsilon_0 \theta(\eta - \eta_0)$, where $\eta_0 \sim 0.4$ characterizes the effective threshold (for $S_T \sim 4 \times 10^{-8}$ erg cm^{-2}), $\varepsilon_0 \sim 0.06$ gives the fraction of the PX-2 field of view ($\sim$1 sr) relative to the entire sky (4π sr) with allowance for the detector efficiency, $\theta(\eta - \eta_0) = 1$ if $0 < \eta < \eta_0$, and $\theta(\eta - \eta_0) = 0$ if $\eta_0 < \eta < 1$. Clearly, as follows from formula (5), the initial and measured fluence distributions at sufficiently large fluences far from the threshold ($\eta \ll \eta_0$) are similar to within the factor ε_0, which allows for recalculation of the number of events to all the sky.

As follows from formula (5), at fluences near the threshold, the shape of the initial distribution must be taken into account when recalculating the number of recorded events to all the sky. If we specify this distribution in the form of a power law $N(>S) = N_0 S^{-\gamma}$, then we derive the obvious relation

$$N^*(>S^*) = (\Delta T/\text{year}) \varepsilon_0 \frac{\eta_0}{\gamma + 1} N(>S); \quad (6)$$

i.e., the recalculation coefficient of the number of recorded events to all the sky generally depends on the assumed slope of the initial $N(>S)$ distribution.

We cannot construct the intrinsic $N(>S)$ distribution and analyze its shape because of the small

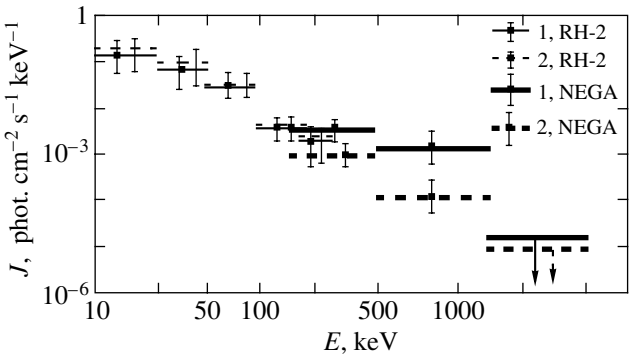

Fig. 2. The energy spectra corresponding to various regions of the time profile for GRB 970601 (marked by numbers in Fig. 1) constructed from readings of the PX-2/GRIF and NEGA/GRIF instruments on the Mir station.

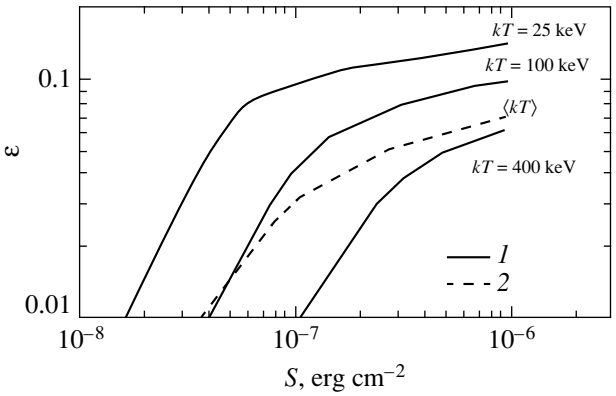

Fig. 3. The fluence dependences of the PX-2 GRB detection efficiency for all the sky computed for bursts with various kT with an optically thin plasma spectrum (*1*) and the average dependence constructed with allowance for the GRB distribution in kT (Masetz *et al.* 1981) (*2*).

GRIF event statistics. However, based on the available statistics, we can estimate the detection rate of bursts from all the sky with fluences larger than the threshold level, i.e., $\sim 10^{-7}$ erg cm^{-2}. The corresponding estimates are illustrated by the dependences $N^*(>S^*)$ (the distribution directly obtained in the experiment) and $N(>S)$ [the distribution recalculated to all the sky according to (6)], which are shown in the $\log N - \log S$ diagram in Fig. 4. Our estimates of the expected GRB detection rate for all the sky near the threshold fluence are given for a flat distribution ($\gamma = 0$) and for another extreme case ($\gamma = 3/2$). We see from the figure that despite the large statistical error, the expected detection rate of GRBs with fluences $>10^{-7}$ erg cm^{-2} agrees, within the error limits, with the BATSE CGRO detection rate (Paciesas *et al.* 1999a, 1999b) if a flat $N(>S)$ distribution is assumed in this range of S [the $N(>S)$ distribution shown in Fig. 4 was constructed from the fluences at energies >20 keV for 1306 events from an improved fourth BATSE catalog (Paciesas *et al.* 2001)]. At the same time, the estimate of $N(>S)$ for $S \sim 10^{-7}$ erg cm^{-2} differs significantly from that predicted by the $S^{-3/2}$ dependence, which holds for a uniform distribution of sources in space, if this dependence is constructed by taking into account the burst detection rate at large fluences from the entire set of available observational data. The fact that the estimated GRB detection rates are slightly larger than the KONUS values may result from the temporal selection effect that took place in this experiment.

Figure 4 also shows the curves that characterize the expected detection rate of faint GRBs obtained in terms of a flat cosmological model for mergers of two compact objects for various cosmological redshifts z corresponding to the epoch of primordial star formation (Lipunov *et al.* 1995). As follows from the figure, the GRIF detection rate of GRBs with fluences $S \sim 10^{-7}$ erg cm^{-2} is consistent with this model for all the z under consideration ($z \geq 2.25$).

It is also of interest to compare the PX-2 estimate for the detection rate of faint GRBs with the corresponding estimate that was obtained by analyzing the so-called BATSE CGRO nontriggered events (Kommers *et al.* 2001). The population of nontriggered events increased the BATSE CGRO burst statistics

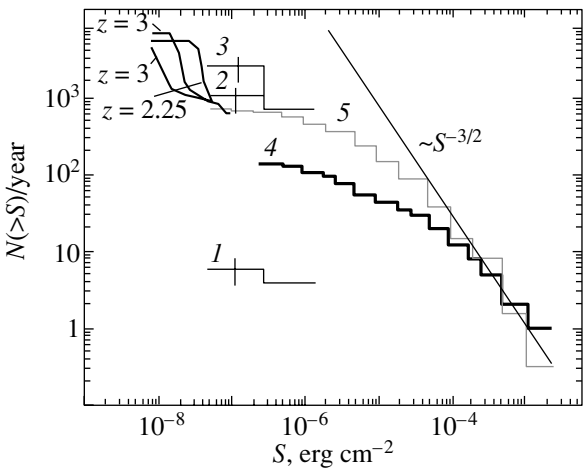

Fig. 4. The integral PX-2 GRB fluence S distribution (*1*); the $\log N - \log S$ relation for the GRB detection rate in all the sky constructed from the PX-2 data by assuming flat (*2*) and $S^{-3/2}$ (*3*) initial $N(>S)$ distributions. Also shown are the corresponding KONUS (*4*) and BATSE CGRO (*5*) data, as well as the dependence $N(>S) \sim S^{-3/2}$, which holds for a uniform distribution of sources in space, and the dependences computed in terms of cosmological models for mergers of two compact objects for various cosmological redshifts z corresponding to the epoch of primordial star formation (Lipunov *et al.* 1995).

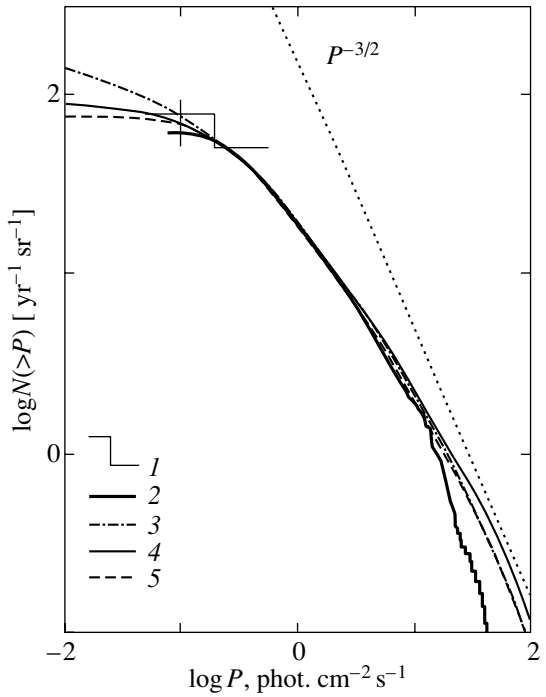

Fig. 5. The integral GRB distribution in peak 50–300 keV flux P constructed from the PX-2 data (*1*) and the distribution of BATSE CGRO nontriggered events (*2*). Also shown are the $\log N$–$\log P$ relations computed in terms of cosmological models with various redshift distributions of sources $\rho(z)$: $\rho(z) \sim$ const (*3*), $\rho(z)$ has a maximum at $z = 1.5$–2 (*4*), and $\rho(z)$ has a maximum at $z = 2$–3 (*5*).

by a factor of almost 1.5. In addition, the detection threshold of nontriggered events is almost a factor of 2 smaller than the detection threshold of normal triggered bursts and thus closer to the GRIF detection threshold. Figure 5 shows the integral distribution of the detection rate of nontriggered events $N(>P)$ in peak 50–300 keV flux P (Kommers *et al.* 2000). The corresponding PX-2 results (assuming a flat initial distribution) are also plotted on these diagrams. As we see from the figure, the GRIF and BATSE CGRO results are in agreement in the overlapped region.

Figure 5 also shows the results of our calculations in terms of major cosmological models: with a uniform (in z) star-formation rate, with a maximum of the star-formation rate at $z = 1.5$–2 (Madau *et al.* 1998), and with a maximum of the star-formation rate at $z = 2$–3 (Hughes *et al.* 1998; Dunlop 1998). As we see from Fig. 5, the PX-2 data are consistent with all of these models, but they are in best agreement with the hypotheses that imply a nonuniform (in z) distribution of the star-formation rate and the frequency of GRB occurrence.

ACKNOWLEDGMENTS

We wish to thank V.V. Bogomolov and A.V. Bogomolov for help in preparing the materials for this study.

REFERENCES

1. A. V. Bogomolov, Yu. I. Logachev, M. I. Kudryavtsev, *et al.*, Izv. Akad. Nauk, Ser. Fiz. **61**, 1130 (1997).
2. A. V. Bogomolov, V. V. Bogomolov, Yu. I. Denisov, *et al.*, Izv. Akad. Nauk, Ser. Fiz. **63**, 1665 (1999).
3. A. V. Bogomolov, V. V. Bogomolov, Yu. I. Denisov, *et al.*, Kosm. Issled. **38**, 377 (2000).
4. H. E. Coffey, http://www.ngdc.noaa.gov/stp/SOLAR/getdata.html (2001).
5. E. Costa, F. Frontera, J. Heise, *et al.*, Nature **387**, 783 (1997).
6. S. G. Djorgovski, S. R. Kulkarni, J. B. Bloom, *et al.*, Astrophys. J. Lett. **508**, L17 (1998).
7. J. S. Dunlop, in *Observational Cosmology with the New Radio Surveys,* Ed. by M. N. Bremer *et al.* (Kluwer, Dordrecht, 1998), p. 157.
8. E. E. Fenimore, R. I. Epstein, C. Ho, *et al.*, Nature **366**, 40 (1993).
9. M. Feroci, F. Frontera, E. Costa, *et al.*, Proc. SPIE **31M**, 186F (1997).
10. D. A. Frail, S. R. Kulkarni, S. R. Nicastro, *et al.*, Nature **389**, 261 (1997).
11. S. V. Golenetski, private communication (2001).
12. J. Hakkila, C. A. Meegan, J. M. Horach, *et al.*, Astrophys. J. **462**, 125 (1996).
13. D. H. Hughes, S. Serjeant, J. S. Dunlop, *et al.*, Nature **394**, 241 (1998).
14. J. M. Kommers, W. H. G. Lewin, C. Kouvelioyou, *et al.*, Astrophys. J. **533**, 696 (2000).
15. J. M. Kommers, W. H. G. Lewin, C. Kouvelioyou, *et al.*, Astrophys. J., Suppl. Ser. **134**, 385 (2001).
16. M. Krumholz, S. E. Thorsett, and F. A. Harrison, Astrophys. J. Lett. **506**, L81 (1998).
17. M. I. Kudryavtsev, V. M. Pankov, A. V. Bogomolov, *et al.*, in *Proceedings of the 24th International Cosmic Ray Conference, 1995,* Vol. 3, p. 567.
18. M. I. Kudryavtsev, V. M. Pankov, A. V. Bogomolov, *et al.*, Izv. Vyssh. Uchebn. Zaved., Radiofiz. **39**, 1539 (1996).
19. S. R. Kulkarni, S. G. Djorgovski, D. A. Frail, *et al.*, Nature **393**, 35 (1998).
20. V. M. Lipunov, K. A. Postnov, M. E. Prokhorov, *et al.*, Astrophys. J. **454**, 593 (1995).
21. P. Madau, M. Della Valle, and N. Panagia, Mon. Not. R. Astron. Soc. **297**, L17 (1998).
22. S. Mao and H. J. Mo, Astron. Astrophys. **339**, L1 (1998).
23. E. P. Masetz and S. V. Golenetski, Astrophys. Space Sci. **75**, 47 (1981).
24. E. P. Masetz, S. V. Golenetski, V. N. Il'inski, *et al.*, Preprint No. 719, FTI AN SSSR (Leningrad, 1981).
25. C. A. Meegan, G. J. Fishman, R. B. Wilson, *et al.*, Nature **355**, 143 (1992).

26. C. A. Meegan, G. N. Pendleton, M. S. Briggs, *et al.*, Astrophys. J., Suppl. Ser. **106**, 65 (1996).
27. M. Metzger, S. G. Djorgovski, S. R. Kulkarni, *et al.*, Nature **387**, 879 (1997).
28. W. S. Paciesas, C. A. Meegan, G. N. Pendleton, *et al.*, Astrophys. J., Suppl. Ser. **122**, 465 (1999a).
29. W. S. Paciesas, C. A. Meegan, G. N. Pendleton, *et al.*, Astrophys. J., Suppl. Ser. **122**, 497 (1999b).
30. W. S. Paciesas, C. A. Meegan, G. N. Pendleton, *et al.*, Vizie R. On-line Data Catalog: IX 120A, http://www.batse.msfc.nasa.gov/batse/grb/catalog/4b/ (2001).
31. R. E. Rutledge, L. Hui, and W. H. C. Lewin, Mon. Not. R. Astron. Soc. **276**, 753 (1995).
32. T. Totani, Astrophys. J. Lett. **486**, L71 (1997).
33. J. van Paradijs, P. J. Groot, T. Galama, *et al.*, Nature **386**, 686 (1997).
34. R. A. M. J. Wijers, J. S. Bloom, J. B. Bagla, and P. Natarajan, Mon. Not. R. Astron. Soc. **294**, L13 (1998).

Translated by V. Astakhov

Astronomy Letters, Vol. 28, No. 5, 2002, pp. 296–302. Translated from Pis'ma v Astronomicheskiĭ Zhurnal, Vol. 28, No. 5, 2002, pp. 341–347.

Searches for the Sources of Cosmic Rays with Energies $(1–4) \times 10^{17}$ eV Using the Yakutsk EAS Array

A. V. Glushkov* **and M. I. Pravdin**

Institute of Cosmophysical Research and Aeronomy, Siberian Division, Russian Academy of Sciences, pr. Lenina 31, Yakutsk, 677007 Russia

Received December 17, 2001

Abstract—We analyze the arrival directions of cosmic rays with energies $E_0 \approx (1–4) \times 10^{17}$ eV and zenith angles $\theta \leq 53°$ detected with the Yakutsk extensive air shower (EAS) array during 1974–2001. We show that ~10% of them form many clusters correlated with the Supergalactic plane. Enhanced particle fluxes arrive from the Supergalactic plane and the regions that are symmetrically adjacent to it at angles $\pm b_{SG} \approx 6.^{\circ}5$. The relatively high concentrations of clusters of galaxies and quasars that bear a relationship to the large-scale structure of the Universe are observed in these regions. © *2002 MAIK "Nauka/Interperiodica".*

Key words: *cosmic rays, nonthermal radiation, large-scale structure of Universe*

INTRODUCTION

Some researchers believe that very high-energy primary cosmic rays ($E_0 > 10^{17}$ eV) consist mostly of charged particles: protons and nuclei of various chemical elements. These particles are strongly mixed by the Galactic magnetic field and have an almost isotropic sky distribution, making local sources of primary cosmic rays rather difficult to identify. This view is by no means indisputable, because so far no direct measurements have been made of the composition of ultrahigh-energy PCR, and the conclusions based on extensive air shower data are ambiguous and inconsistent.

Stanev *et al.* (1995) found that the directions of arrival of PCR in the EAS energy range ($E_0 \geq 10^{19}$ eV) correlated with the plane of the Local Supercluster of galaxies (the Supergalaxy). This result was corroborated by those obtained by Glushkov and Sleptsov (2001), Glushkov and Pravdin (2001a, 2001b), and Glushkov (2001) based on observations made with the Yakutsk EAS array. Mikhaĭlov (1999) and the AGASA group (Takeda *et al.*, 1999) reported observations of individual clusters in the directions of arrival of giant EAS. Glushkov and Pravdin (2001b) pointed out multiple formation of clusters, which takes place not only at $E_0 \geq 10^{19}$ eV, but also at lower PCR energies ($E_0 \approx (3–10) \times 10^{18}$ eV).

Earlier, Glushkov (1988) reported that the distribution of arrival directions of PCR with $E_0 \geq 4 \times 10^{17}$ eV exhibits a considerable number of shower groups within narrow solid angles. The sky distribution of these shower groups exhibits a regular small-scale pattern, which cannot be explained by random statistical processes. The author believes that this pattern may be due to the distribution of extragalactic PCR point sources, which generate neutral particles. Below we report new evidence corroborating this hypothesis.

PARAMETERS STUDIED AND DISCUSSION

In this paper, we analyze extensive air showers with energies $E_0 \approx (1.3–4) \times 10^{17}$ eV and zenith angles $\cos\theta \geq 0.6$ recorded by the Yakutsk array during 1974–2001. We analyzed the small-scale anisotropy, i.e., local PCR inhomogeneities, on angular scales ~5°–10°. Our analysis included EAS whose directions of arrival were inferred from the data from ≥4 stations and whose axes were located within the central array circle of radius ≤1000 m. We determined the energy E_0 of primary particles from the following formulas:

$$E_0 = (4.8 \pm 1.6) \times 10^{17} (\rho_{s,600}(0°))^{1.0 \pm 0.02}, \text{ eV}; \quad (1)$$

$$\rho_{s,600}(0°) = \rho_{s,600}(\theta) \times \exp((\sec\theta - 1) \times 1020/\lambda_\rho), \text{ m}^{-2}; \quad (2)$$

$$\lambda_\rho = (450 \pm 44) + (32 \pm 15) \log(\rho_{s,600}(0°)), \text{ g/cm}^2, \quad (3)$$

*E-mail: a.v.glushkov@ikfia.ysn.ru

1063-7737/02/2805-0296$22.00

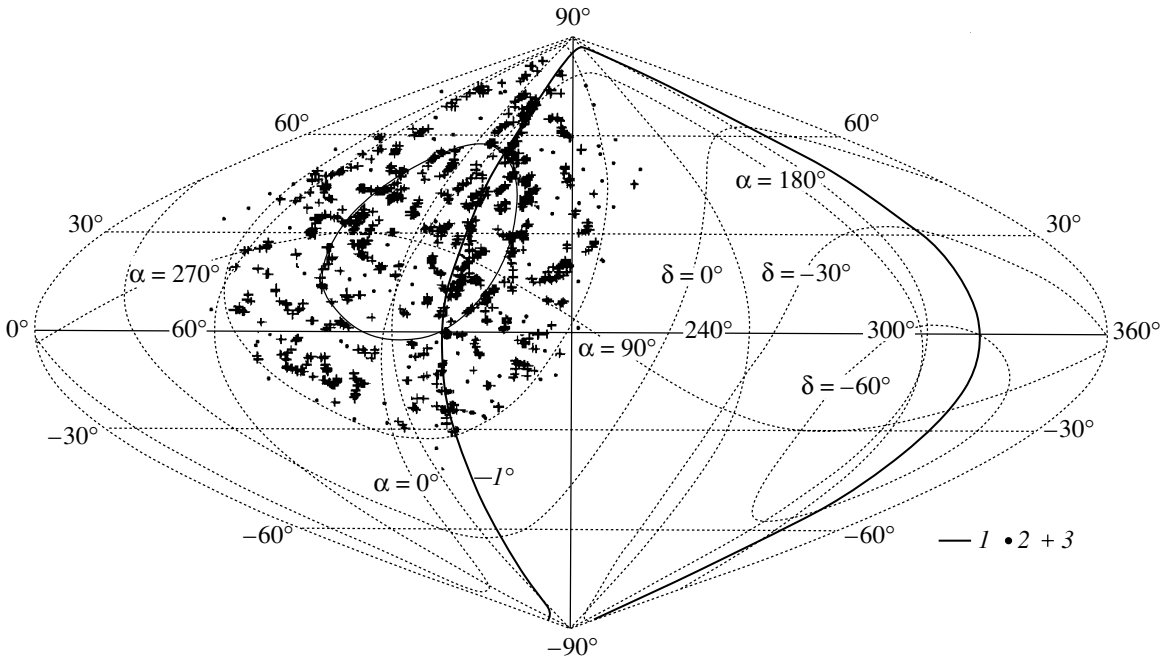

Fig. 1. The map of nodes and clusters of 1882 showers with $E_0 = 10^{17.2-17.3}$ eV and $\theta \leq 53°$ in Galactic coordinates according to the data from Yakutsk EAS array: (*1*) the Supergalactic disk; (*2*) nodes with $m = 1$; (*3*) clusters with $m \geq 2$ nodes within circles of radius $d = 3°$.

where $\rho_{s,600}(\theta)$ is the density of charged particles as measured by ground-based scintillation facilities at a distance of $R = 600$ m from the shower axis.

We analyzed a total of 36 825 showers in five energy intervals within steps of $\Delta \log E_0 = 0.1$. From these intervals, we drew seven independent samples with an approximately equal number of events ≈ 1000, which differed only in that their axes were located in different annular areas inside the central array circle. We analyzed each of the $35 = 5 \times 7$ samples individually in order to identify whether it contained any local shower groups on the sky sphere by proceeding in the same way as in our earlier work (Glushkov and Pravdin 2001b). We found all "neighbors" within $d \leq 3°$ of the arrival direction of each shower. If we found $n \geq 3$ showers within the circle, we averaged their coordinates and used them as new data points (hereafter referred to as nodes) in subsequent analysis.

We then analyzed the nodes separately in all five energy intervals in order to identify mutual $m \geq 2$ intersections in any of the seven samples, provided that their centers were located within $d \leq 3°$ of each other. Upon finding such nodes, we again averaged the arrival directions of their constituent showers and used the resulting larger node (hereafter referred to as a cluster) in subsequent analysis.

Figure 1 shows a Galactic-coordinate map of clusters on the projected sky sphere for showers with energies $E_0 = 10^{17.2-17.3}$ eV. This map is constructed in such a way that equal areas correspond to equal areas on the sky. The solid line shows the Supergalactic plane with its North Pole at $\alpha = 286.2°$ and $\delta = 14.1°$ (equatorial coordinates). Equatorial coordinates are also shown on this map for better visualization. Nodes with $m = 1$ and clusters with c $m \geq 2$ are shown by dots and crosses, respectively.

One immediately sees that most of clusters form local features. A similar pattern is observed at other PCR energies. The locations of clusters with different energies often coincide. Figure 2 shows the map of clusters that are common to all five groups mentioned above with $E_0 = 10^{17.1-17.2}$, $10^{17.2-17.3}$, $10^{17.3-17.4}$, $10^{17.4-17.5}$, and $10^{17.5-17.6}$ eV. These clusters were identified as locations where the angular coordinates of 10 to 18 nodes drawn from 35 independent samples coincide, each consisting of ≈ 1000 showers. The cluster density near the Galactic disk proved to be lower than at higher latitudes. It can also be noted that the number of events within the $|b_G| \leq 10°$ band is much smaller than near the Supergalactic disk region of the same area.

The negative correlation of clusters with the Galactic disk and their positive correlation with the Supergalactic disk is immediately apparent from Fig. 3, which shows the distributions of the directions of arrival of 2969 showers (clusters in Fig. 2) in Galactic (G) and Supergalactic (SG) coordinates as

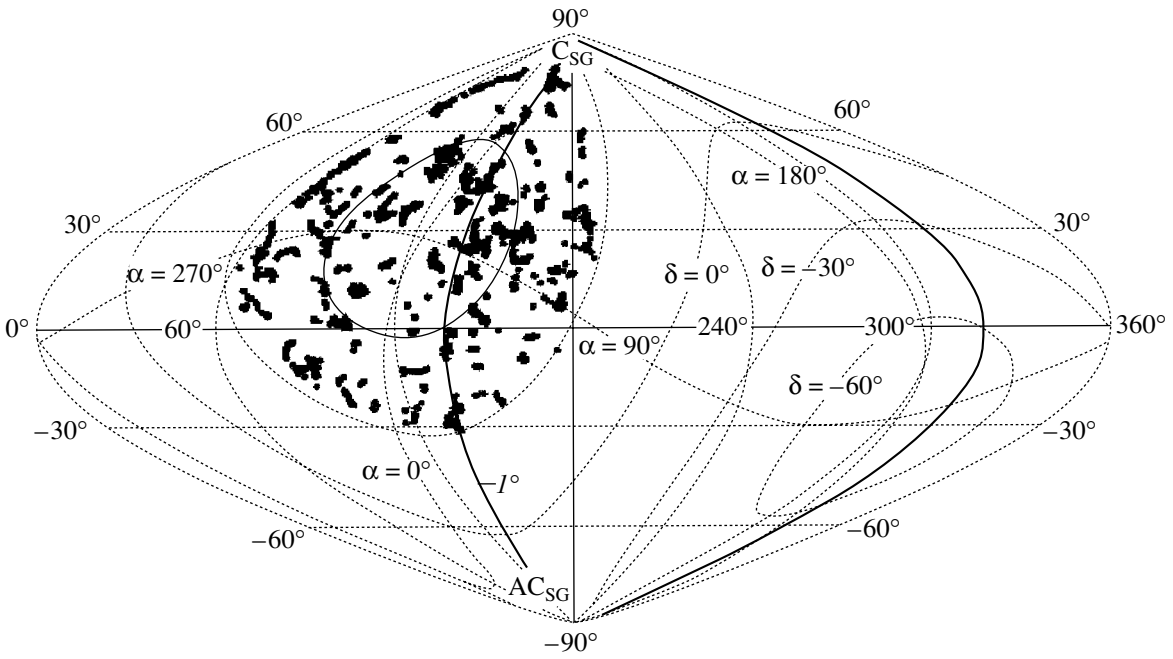

Fig. 2. The Galactic-coordinate map of clusters identified among 2969 showers that are common to five groups with $E_0 = 10^{17.1-17.2}$, $10^{17.2-17.3}$, $10^{17.3-17.4}$, $10^{17.4-17.5}$, and $10^{17.5-17.6}$ eV: Curve *1* shows the Supergalactic disk; C_{SG} and AC_{SG} are the Supergalactic center and anticenter, respectively.

a function of the latitude of the direction of arrival (in steps of $\Delta b = 2°$). The curves show the distributions expected for an isotropic flux computed using the Monte Carlo method.

Figure 3 (position G) shows a conspicuous gap at $|b_G| \leq 10°$. The deficit of events in this region amounts to $(395 - 625)/\sqrt{625} = 9.2\sigma$. At the same time, one can see in Fig. 3 (position SG(a) a series of statistically significant peaks. Peak *2* can be seen to lie exactly in the Supergalactic disk. Its excess over the expected curve amounts to $\approx 6.6\sigma$. However, its statistical significance is even higher given the two gaps on its sides. Another series of peaks is located symmetrically with respect to the Supergalactic plane. Peaks *1* and *3* are thus located at an angular distance of $\approx 6.^\circ 5$ from this plane; peaks *4* and *5*, at a distance of $\approx 20°$; and peaks *6* and *7*, at a distance of $\approx 33°$. In principle, all peaks marked by arrows are consistent with a discrete distribution with a step of $\approx 6.^\circ 5$.

Both distributions in Fig. 3 have chance probabilities of $< 10^{-6}$. These results can be interpreted as indicative of the extragalactic nature of the fraction of PCR that is contained in clusters. It appears that the Galaxy only absorbs this radiation and this absorption is stronger in the disk. Other statistically significant peaks in Fig. 3 (position SG(a)) appear to be indicative of the complex and inhomogeneous structure of the extragalactic space in the regions where the constituent PCR sources of the clusters are located.

We now analyze in more detail the events that make the principal contribution to peaks *1–3*. Figure 4 shows the distributions of the showers that make up these peaks in the latitude bands $6° < b_{SG} < 10°$ (*1*), $-2° < b_{SG} < 4°$ (*2*), and $-12° < b_{SG} < -6°$ (*3*) as a function of the Supergalactic longitude (with a step of $\Delta l_{SG} = 2°$) counted counterclockwise from the anticenter direction. Letters indicate the most powerful peaks: *a*—$l_{SG} \approx 76°$; *b*—$l_{SG} \approx 101°$; *c*—$l_{SG} \approx 117°$; *d*—$l_{SG} \approx 121°$; *e*—$l_{SG} \approx 127°$; *g*—$l_{SG} \approx 140°$; *f*—$l_{SG} \approx 145°$; *h*—$l_{SG} \approx 171°$. Individual peaks have almost coincident locations and all of them (and other less significant peaks) fit into a sequence with a step of $\approx 6.^\circ 5$.

Note a curious point. Glushkov (2001) showed that peaks *1–3* are also observed at $E_0 \geq 10^{19}$ eV. We show these data in Fig. 3 (position SG(b)) for comparison. One can see a remarkable similarity between the Supergalactic-coordinate distributions with $E_0 \approx (1.3–4) \times 10^{17}$ eV and $E_0 \geq 10^{19}$ eV in the region $|b_{SG}| \leq 30°$. Here the distributions match each other even in their individual features. It is our opinion that all these peaks are by no means accidental.

Observations and theory imply (see, e.g., Vorontsov-Vel'yaminov *et al.* 1978) the existence in the Universe of large 100–130 Mpc black holes separated by relatively thin (20–30 Mpc) layers. In these

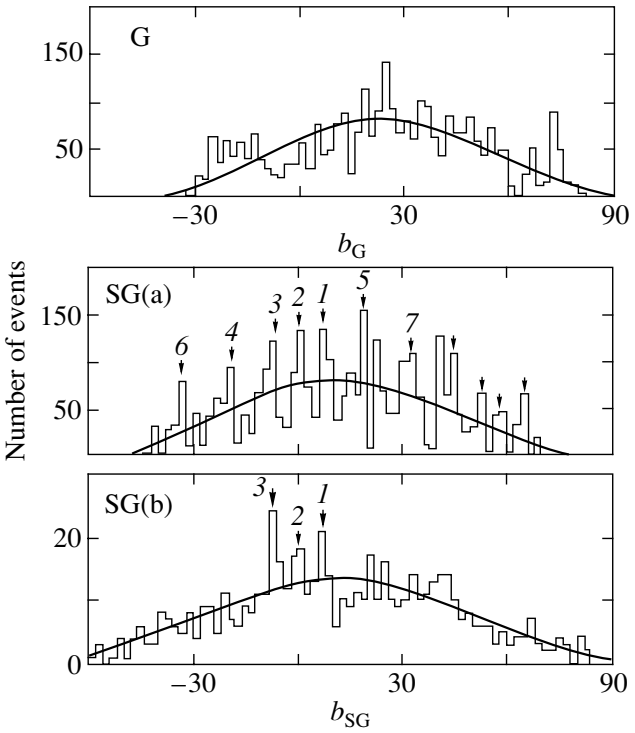

Fig. 3. Distributions of directions of arrival of 2969 showers in clusters shown in Fig. 2 as a function of their Galactic (G) and Supergalactic (SG) latitude: (b) the data of Glushkov (2001) for EAS with $E_0 \geq 10^{19}$ eV. Smooth curves show the expected distributions for an isotropic PCR flux.

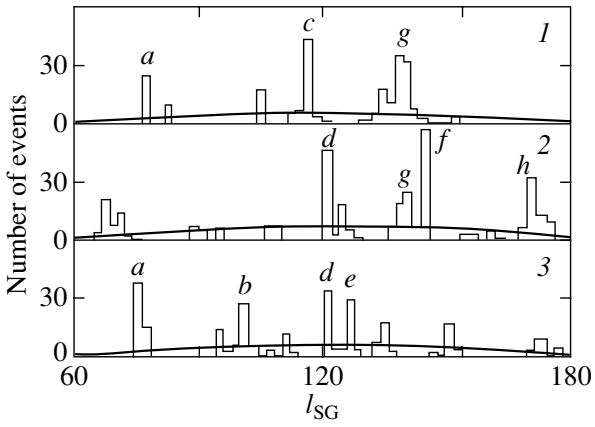

Fig. 4. Distribution of showers that make up peaks *1*–*3* in Fig. 3 (positions SG(a)), in the bands $6^\circ < b_{SG} < 10^\circ$ (*1*), $-2^\circ < b_{SG} < 4^\circ$ (*2*), and $-12^\circ < b_{SG} < -6^\circ$ (*3*) as a function of Supergalactic longitude: *a*—$l_{SG} \approx 76^\circ$; *b*—$l_{SG} \approx 101^\circ$; *c*—$l_{SG} \approx 117^\circ$; *d*—$l_{SG} \approx 121^\circ$; *e*—$l_{SG} \approx 127^\circ$; *g*—$l_{SG} \approx 140^\circ$; *f*—$l_{SG} \approx 145^\circ$; *h*—$l_{SG} \approx 171^\circ$. Smooth curves show the expected distributions for isotropic PCR flux.

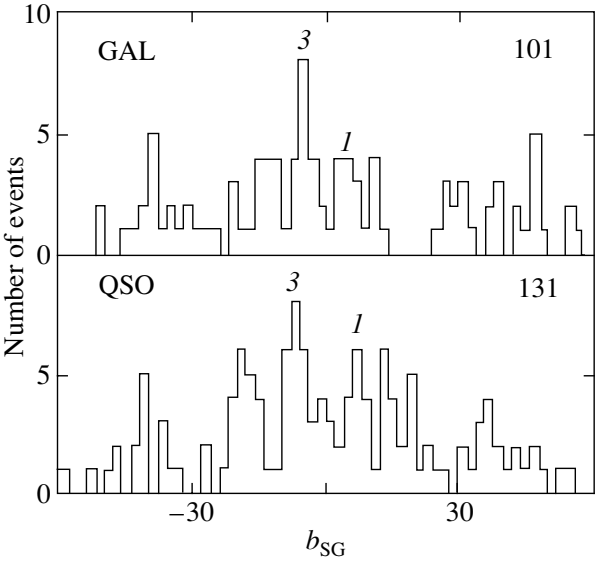

Fig. 5. Supergalactic latitude distributions of 49 superclusters (Lebedev and Lebedeva 1988), 52 clusters (Abalakin 1981), and bright galaxies (Zombeck 1982) at heliocentric distances $\geq$10 Mpc (GAL), as well as 131 quasars (QSO) with redshifts $z \leq 0.2$ (Hewitt and Burbidge 1987). For peaks *1* and *3*, see Fig. 3 (SG).

layers are concentrated more than 60–80% of the galaxies that tend to gather into prolate and oblate superclusters. The Supergalaxy considered here (its diameter is 50–60 Mpc) is just one such supercluster. Many superclusters appear to join each other, forming a single cellular structure of the Universe (Vorontsov-Vel'yaminov *et al.* 1978).

The fact that the directions of arrival of PCR "break" into peaks in Fig. 3 (position SG) and Fig. 4 can be interpreted as evidence for the adiabatic ("pancake") theory of Zel'dovich (1982), where the geometry of metagalactic structures is characterized by giant flat formations separated by large ($\sim 10^5$ Mpc^3) and almost galaxy-free volumes.

We now analyze in more detail peaks *1*–*3*, leaving other peaks aside. Now consider certain objects in the Universe that can shed additional light on the nature of these peaks. Figure 5 (GAL) shows the Supergalactic latitude distribution of 49 superclusters (located in the Galactic latitude interval $b_G > 30^\circ$) with distances 100–500 Mpc (Lebedev and Lebedeva 1988). We supplemented this sample with 52 randomly selected clusters (Abalakin 1981) and bright galaxies (Zombeck 1982) located at distances $\geq$10 Mpc. One can also see in this figure peaks *1* and *3* that are located in the vicinity of the Supergalactic plane. Their locations approximately coincide with those of similar peaks in Fig. 3 (position SG) (although they may be $\approx 1\overset{\circ}{.}5$ closer to the Supergalactic plane). Note that peak *3* includes the central part of the Virgo supercluster and peak *1*, the Coma supercluster, which contain several clusters of galaxies at

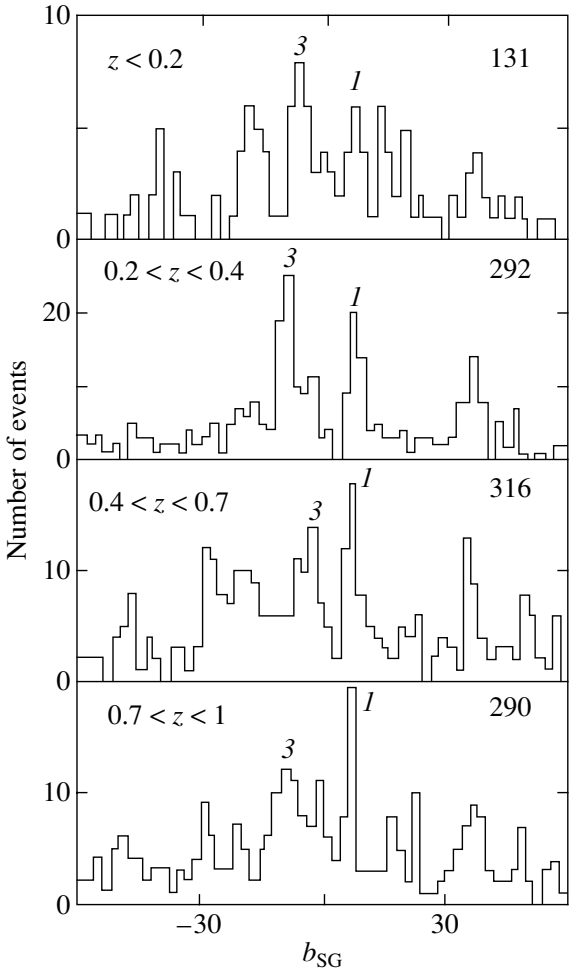

Fig. 6. Supergalactic latitude distributions of quasars (Hewitt and Burbidge 1987) with different redshifts z (numerals on the right indicate the number of objects). See Fig. 3 (SG) for peaks *1* and *3*.

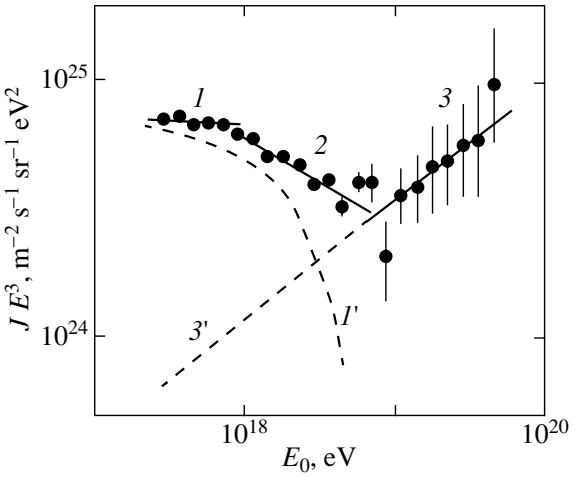

Fig. 7. The energy spectrum of primary particles $J(E_0) \propto E_0^{-\gamma}$ measured by the Yakutsk array (Pravdin *et al.* 1999). Power-law variations of intensities: *1*—$E_0 < 10^{18.0}$ eV ($\gamma_1 = -3.05 \pm 0.04$), *2*—$10^{18} \le E_0 < 10^{19.0}$ eV ($\gamma_2 = -3.34 \pm 0.05$), *3*—$E_0 \ge 10^{19.0}$ eV ($\gamma_3 = -2.53 \pm 0.25$); *1′* and *3′*—are the assumed Galactic and extragalactic components, respectively.

different heliocentric distances of up to ∼1000 Mpc (Vorontsov-Vel'yaminov *et al.* 1978).

Figure 5 (QSO) shows the distribution of 131 quasars in the same coordinates (Hewitt and Burbidge 1987) with $z \le 0.2$ (at heliocentric distances ≤800 Mpc for the adopted Hubble constant of $H_0 =$ 75 km/s Mpc). Here, peaks *1* and *3*, which are located at the same places as in Fig. 3 (position SG) are immediately apparent. This fact can be interpreted as evidence for quasars being one of the possible sources of PCR in the energy interval considered. The absence of peak *2* in this figure may be due to the absorption of optical quasar radiation by denser matter in the Supergalactic plane. The structure of the Universe is more transparent for ultrahigh-energy PCR.

The data analyzed here confirm the presence in the Universe of a material structure that has a certain regularity on a cosmological scale. Some researchers believe (Einasto *et al.* 1997) that this may be a "chessboard"-type pattern. Peaks *1* and *3* indicate that ≈6°–7° from the Supergalactic plane (on both sides of the latter) appreciable concentrations of galaxies and quasars can be found that may be the places where a certain fraction of ultrahigh-energy PCR is generated.

We now estimate the transversal sizes of these structures (which maybe associated with peaks *1* and *3*) from the formula $D \approx 2r \tan 6.^\circ 5$ for quasars. According to Khodyachikh (1996), the distribution of structure sizes for our sample of quasars with $z \le 0.2$ peaks at $\langle z \rangle = 0.14$. We find from this that $r = c\langle z \rangle / H_0 = 560$ Mpc (here c is the speed of light and $H_0 = 75$ km/s Mpc). The resulting quantity $D \approx 127$ Mpc agrees with the above-mentioned sizes of voids in the cellular structure of the Universe (Vorontsov-Vel'yaminov *et al.* 1978).

Note that peaks *1* and *3* in Fig. 5 (QSO) are observed at different quasar redshifts (Fig. 6). This fact must be indicative of the global scale of the directions in the Universe identified in the vicinity of the Supergalactic plane. In addition, Fig. 6 also shows peaks that must be associated with some other fragments of the large-scale structure of the Universe.

According to the data from the Yakutsk EAS array (Pravdin *et al.* 2001), the total flux of PCR with energies $E_0 \approx (1–4) \times 10^{17}$ eV exhibits no statistically significant anisotropy. The amplitude of the first-order harmonic in right ascension as inferred using the traditional harmonic analysis technique is equal to

$(0.45 \pm 0.55)\%$. However, the phase of the first harmonic inferred by the above authors deserves special attention: it is equal to $\varphi_1 = 192^\circ \pm 70^\circ$. This phase, albeit highly uncertain because of the anisotropy of PCR, points nevertheless to the Supergalactic center (C_{SG} in Fig. 2).

The results of Pravdin *et al.* (2001) obtained in this work can be explained by assuming that PCR consist of two components. One of these components is ≈10 times more intense that the other component, and it probably includes charged particles that are strongly mixed by the Galactic magnetic field. The second component, which forms clusters, must consist of extragalactic neutral particles. The latter component, albeit strongly "diluted" by the isotropic flux of the first component, nevertheless manifests itself in the results of Pravdin *et al.* (2001).

CONCLUSIONS

It follows from the data presented above that a certain fraction of cosmic rays with energies $E_0 \approx (1-4) \times 10^{17}$ eV forms numerous clusters within solid angles $d \leq 3^\circ$ (Figs. 1, 2). They show a negative correlation with the Galactic disk and a positive correlation with the Supergalactic disk (Fig. 3). It might be supposed that clusters indicate some extragalactic PCR point sources that are in a certain way related to the large-scale structure of the Universe.

Here we have for the first time also discovered a "finer" structure in the distribution of ultrahigh-energy PCR (peaks *1–3* and others). Peaks *1* and *3*, which are adjacent to the Supergalactic plane at angles $\pm b_{SG} \approx 6^\circ - 7^\circ$, can also be observed in clusters of galaxies and quasars. Coincident peaks can also be found in other places in the distributions. It is immediately evident that most of these peaks are consistent with angular separations forming a discrete pattern with a step of $\approx 6\overset{\circ}{.}5$. This step might well be associated in one way or another with the apparent scale length of the cellular structure of the Universe.

The primary particles that form clusters are in all probability electrically neutral, because otherwise they would have lost the connection between their source directions. The fraction of these particles in the total flux of PCR with energies $E_0 \approx (1.3 \times 4) \times 10^{17}$ eV is approximately equal to $2969/36\,825 \approx 0.08$ and should be close to unity at $E_0 \geq 10^{19}$ eV, according to Glushkov and Sleptsov (2001), Glushkov and Pravdin (2001a, 2001b), and Glushkov (2001). This hypothesis is illustrated in Fig. 7, where curves *1* and *3* show, respectively, our assumed Galactic and extragalactic components and the energy spectrum of ultrahigh-energy PCR as measured by Pravdin *et al.* (1999) with the Yakutsk array.

The remaining events, which do not belong to clusters, are distributed almost isotropically in the sky. This part of PCR may consist of charged particles (protons and nuclei of chemical elements) with a diffuse propagation pattern in the Galaxy. One powerful source of such events is located near the Galactic center (Hayashida *et al.* 1999; Bellido *et al.* 2000; Teshima *et al.* 2001). Other sources of charged particles are so far difficult to find, because their locations are greatly smeared by the Galactic magnetic field.

ACKNOWLEDGMENTS

This work was carried out owing to the financial support granted by the Ministry of Science of the Russian Federation to the Yakutsk EAS array (registration no. 01-30) included into the "List of Unique Research and Experimental Facilities of National Importance" and the Russian Foundation for Basic Research (project no. 00-15-96787).

REFERENCES

1. V. K. Abalakin, *Astronomical Calendar. Permanent Part* (Nauka, Moscow, 1981).
2. J. A. Bellido, B. W. Clay, R. B. Dawson, and M. Johnston-Hollitt, astro-ph/0009039 (2000).
3. J. Einasto *et al.*, Nature **385**, 139 (1997).
4. A. V. Glushkov, Pis'ma Zh. Éksp. Teor. Fiz. **48**, 513 (1988) [JETP Lett. **48**, 555 (1988)].
5. A. V. Glushkov, Pis'ma Zh. Éksp. Teor. Fiz. **73**, 355 (2001) [JETP Lett. **73**, 313 (2001)].
6. A. V. Glushkov and I. E. Sleptsov, Izv. Akad. Nauk, Ser. Fiz. **65**, 437 (2001).
7. A. V. Glushkov and M. I. Pravdin, Zh. Éksp. Teor. Fiz. **119**, 1029 (2001a) [JETP **92**, 887 (2001a)].
8. A. V. Glushkov and M. I. Pravdin, Pis'ma Astron. Zh. **27**, 577 (2001b) [Astron. Lett. **27**, 493 (2001b)].
9. N. Hayashida, M. Nagano, D. Nishikawa, *et al.*, Astropart. Phys. **10**, 303 (1999).
10. A. Hewitt and G. Burbidge, Astrophys. J., Suppl. Ser. **63**, 1 (1987).
11. M. F. Khodyachikh, Astron. Zh. **73**, 11 (1996) [Astron. Rep. **40**, 6 (1996)].
12. V. S. Lebedev and I. A. Lebedeva, Pis'ma Astron. Zh. **14**, 18 (1988) [Sov. Astron. Lett. **14**, 7 (1988)].
13. A. A. Mikhaĭlov, Izv. Akad. Nauk, Ser. Fiz. **63**, 557 (1999).
14. M. I. Pravdin, M. N. Dyakonov, A. V. Glushkov, *et al.*, in *Proceedings of the 26th International Cosmic Ray Conference, Salt Lake City, 1999,* Vol. 3, p. 292.
15. M. I. Pravdin, A. A. Ivanov, A. D. Krasil'nikov, *et al.*, Zh. Éksp. Teor. Fiz. **119**, 881 (2001) [JETP **92**, 766 (2001)].
16. T. Stanev, P. L. Biermann, J. Lloyd-Evans, *et al.*, Phys. Rev. Lett. **75**, 3056 (1995).
17. M. Takeda, N. Hayashida, K. Honda, *et al.*, Astrophys. J. **522**, 225 (1999).

18. M. Teshima, M. Shikawa, M. Fukushima, *et al.*, in *Proceedings of the 27th International Cosmic Ray Conference, Hamburg, 2001,* Vol. 3, p. 337.
19. B. A. Vorontsov-Vel'yaminov, I. D. Karachentsev, E. L. Turner, *et al.*, in *The Large Scale Structure of the Universe: International Astronomical Union Symposium No. 79, Tallinn, 1977,* Ed. by M. S. Longair and J. Einasto (D. Reidel, Dordrecht, 1978; Mir, Moscow, 1981).
20. Ya. B. Zel'dovich, Pis'ma Astron. Zh. **8**, 195 (1982) [Sov. Astron. Lett. **8**, 102 (1982)].
21. M. V. Zombeck, *Handbook of Space Astronomy and Astrophysics* (Cambridge Univ. Press, Cambridge, 1982).

Translated by A. Dambis

Astronomy Letters, Vol. 28, No. 5, 2002, pp. 303–309. Translated from Pis'ma v Astronomicheskiĭ Zhurnal, Vol. 28, No. 5, 2002, pp. 348–355.

Interaction of the Supernova Remnant S 147 with the Ambient Interstellar Gas

I. V. Gosachinskij*

Special Astrophysical Observatory, St. Petersburg Branch, Russian Academy of Sciences, Pulkovo, St. Petersburg, 196140 Russia

Received November 15, 2001

Abstract—Based on RATAN-600 21-cm H I line observations with an angular resolution of 2.4′, we studied the neutral-hydrogen distribution in the region of the supernova remnant (SNR) S 147 (G180.0–1.7). We detected a rotating shell of neutral gas immediately adjacent to the SNR that is expanding at a velocity of 20 km s^{-1}. The H I shell is less distinct in the southeastern part and at negative radial velocities. The outer shell diameter is 90 pc; the H I mass in the shell is $2.2 \times 10^4 M_\odot$. These data allowed us to estimate the SNR age, 6.5×10^5 yr, and the initial explosion energy, 2.2×10^{51} erg. © *2002 MAIK "Nauka/Interperiodica".*

Key words: *supernovae, supernova remnants, interaction with ambient medium*

INTRODUCTION

The supernova remnant (SNR) S 147 located in the Galactic-anticenter region is believed to be the most evolved SNR in the Galaxy. Except for the so-called spurs whose nature is also associated with nearby SNRs, S 147 has the largest angular size among SNRs in the radio and optical ranges, more than 3°. In the radio range, it appears as an almost regular shell; in contrast to other SNRs, the spectral index of its radio emission clearly varies over the disk [see Fürst and Reich (1986) and references in Green (1993)]. In the optical range, the SNR appears as a tangle of filaments (van den Bergh *et al.* 1973), with bright radio features corresponding to the brightest filaments. Radial-velocity measurements of optical absorption lines in the spectra of stars projected onto this object revealed large radial velocities of the absorbing gas, which are assumed to be attributable to the expansion of nebular filaments (Silk and Wallerstein 1973; Phillips *et al.* 1981). Direct measurements of the H_α emission from the nebular filaments (Lozinskaya 1976) confirmed the presence of expansion velocities up to 100 km s^{-1}.

The interstellar-gas distribution around this SNR was investigated in the H I radio line by Assousa *et al.* (1973), who found a shell at negative radial velocities (from −47 to −24 km s^{-1}). Since this result was reported in a brief summary to the paper and since the complete paper has never been published, it is rather difficult to get an idea of these results. In the observatory report for 1975, it was mentioned that the expansion velocity of this shell is 25 km s^{-1}. In the only H I survey by Koo and Heiles (1991) aimed at searching for H I brightenings in SNR regions, this object has the lowest "reliability rank" and was not included in the list of objects with excess H I emission. The molecular-gas distribution has not been studied either, except by Gondhalekar and Phillips (1980) who reported the detection of an ultraviolet CO absorption line. Such a chilly attitude of observers to this object appears to be explained by its large size, so the background H I emission is difficult to separate from the features that could be associated with the SNR. The high sensitivity in brightness temperature and high (though one-dimensional) angular resolution of RATAN-600 allow such observational problems to be effectively solved. In this paper, we present the results of our RATAN-600 H I 21-cm study for the SNR S 147 region carried out in 1999–2000.

INSTRUMENTATION AND TECHNIQUES

To investigate the distribution of interstellar neutral hydrogen in the S 147 region, we obtained ten drift curves in right ascension at 0.6° intervals in declination over the declination range +25.0° to +31.5°. In this elevation range, the RATAN-600 antenna has an angular resolution of 2.4′ × 20′ and an effective area of about 950 m^2 (Esepkina *et al.* 1979). An uncooled HEMT amplifier was used at the input (Il'in *et al.* 1997). The system noise temperature was

*E-mail: gos@fsao.spb.su

$\sim$70 K; the 39-channel filter spectrum analyzer had a channel bandwidth of 30 kHz (6.3 km s^{-1}), and the separation between channels was also 30 kHz (Venger *et al.* 1982). The data acquisition and preprocessing were carried out using an IBM PC (Alferova *et al.* 1986).

The drift curve at each declination consisted of two series of three observations each obtained by shifting the receiver tuning frequency by half the channel bandwidth. As a result, each drift curve had 78 spectral channels that followed at 3.15 km s^{-1} intervals. This technique also allowed the interference to be effectively removed. The rms of the antenna-temperature fluctuations in spectral channels on an averaged record was 0.2 K. The antenna and equipment parameters were checked in each series of observations by measuring a set of reference sources (Venger *et al.* 1981).

Subsequently, we subtracted the extended background obtained by spline interpolation at the lower brightness-distribution level from the drift curves in each spectral channel and reduced the drift curves containing only features of small angular sizes. The subtracted background component of the drift curves apparently includes the following: (1) large-scale features of the interstellar-gas distribution, such as spiral arms or giant complexes; (2) emission from the intercloud medium, if present; (3) features of small angular sizes unresolved by the RATAN-600 beam; and (4) the spurious large-scale background produced by distant side lobes and the RATAN-600 stray field. It should also be noted that subtracting the background component by the above method can result in an underestimation of the brightness and angular sizes of the remaining small-scale features. We determined the parameters of the latter in each channel by Gaussian analysis and then attempted to establish a relationship between H I features at different radial velocities and at different declinations. Note that this is the only procedure where a significant subjective factor could be introduced.

The errors of the measured parameters have the following values. The radial velocity of an isolated medium-brightness H I feature is measured with an accuracy of at least ± 1 km s^{-1}. In some cases, the accuracy deteriorates because of the difficulties in separating the object from the background or from adjacent features. The measurement error of the H I line brightness temperature is $\sim$0.5 K, including the antenna calibration errors, and the estimation error of the angular size in right ascension is 0.1°. In declination, the antenna resolution is much lower and, accordingly, the accuracy of measuring the angular sizes is lower. The accuracy of estimating the distances depends on the method of their determination and must be considered separately in each case. As a result, the accuracy of estimating the H I mass in an isolated cloud is no higher than 0.5–1 order of magnitude.

RESULTS OF THE OBSERVATIONS AND DISCUSSION

The distribution of 21-cm H I radio line emission in the SNR S 147 region after subtracting the extended background in the right ascension–radial velocity (α–V) plane is shown in Fig. 1. All of the zero-level remnant is located between $5^{\rm h}30^{\rm m}$ and $5^{\rm h}43^{\rm m}$ (1950.0). The thin ring contours schematically indicate H I clouds in the α–V plane, which may represent an inhomogeneous shell immediately adjacent to the radio remnant in spatial coordinates. The isophotal pattern of this ring structure corresponds to the presence of large-scale motions in the shell—expansion and rotation. The ring-shaped pattern of isophotes in the α–V plane suggests the presence of radial motion; in our case, this can only be expansion. The inclination of the isophotes of the presumed shell in the α–V plane corresponds to a radial-velocity gradient across the object disk of $\approx$11 km s^{-1} per degree. Note that S 147 lies almost exactly at the Galactic anticenter, where the normal Galactic rotation gives a very small apparent effect: $\sim$0.4 km s^{-1} per kpc in the radial direction and $\sim$0.25 km s^{-1} per degree in the direction of Galactic longitude; in α, it is even smaller. Consequently, the most plausible explanation of the observed radial-velocity gradient across the disk is rotation. The observed parameters of the H I ring structure we identified are

coordinates of the center: $\alpha(1950.0) = 5^{\rm h}37^{\rm m}.7$, $\delta(1950.0) = +26.0°$;

angular size: 3.5° (outer) and 2.2° (inner);

mean line brightness temperature: 10 ± 0.5 K;

mean radial velocity: -10 ± 5 km s^{-1};

large-scale expansion velocity: $\approx$20 km s^{-1};

radial-velocity gradient: $\approx$11 km s^{-1} per degree.

To check whether the structure we identified is real, it would be appropriate to use data from other H I surveys. The survey by Westerhout and Wendlandt (1982), now accessible in the Strasbourg observational data archive (cdsarc.u-strasbg.fr/cats/VIII/47), is most suitable in resolution. While having a high radial-velocity resolution (2 km s^{-1}) and a sufficient angular resolution (13′), this survey covers a region of only $\pm 2°$ in Galactic latitude, which is too small for the S 147 source. However, we were able to use data from this survey for the drift curve in longitude at $b = -1.5°$ (virtually across the shell center) by transforming them from the FITS format to the common format we use, so that we

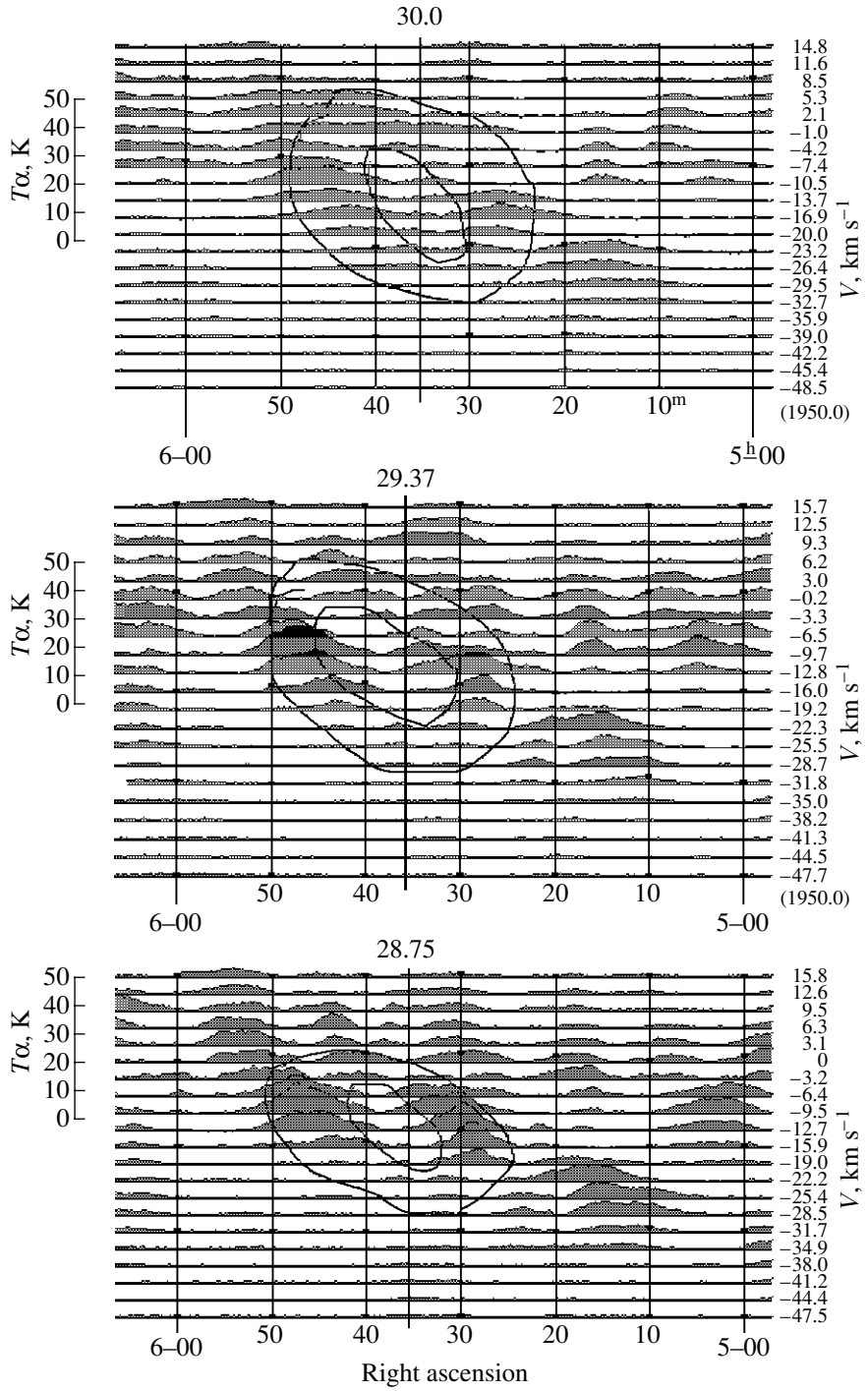

Fig. 1. The distribution of H I emission features in the vicinity of S 147 after subtracting the extended background. The radial velocities are given relative to the Local Standard of Rest; the declination is indicated at the top. The antenna temperature scale is given on the left. The thin lines schematically indicate the H I shell around the SNR. The thick vertical lines mark the SNR radio center in right ascension.

could also subtract the background H I line emission component. The result of our reduction is presented in Fig. 2, where the thin lines delineate a shell structure that is similar in its observed parameters to the shell revealed by the RATAN-600 data. Thus, the survey by Westerhout and Wendlandt (1982) confirms that the H I shell we detected is real.

The molecular-gas distribution in the vicinity of the SNR S 147 can be checked by using data from the CO surveys by Dame *et al.* (1987, 2001), which

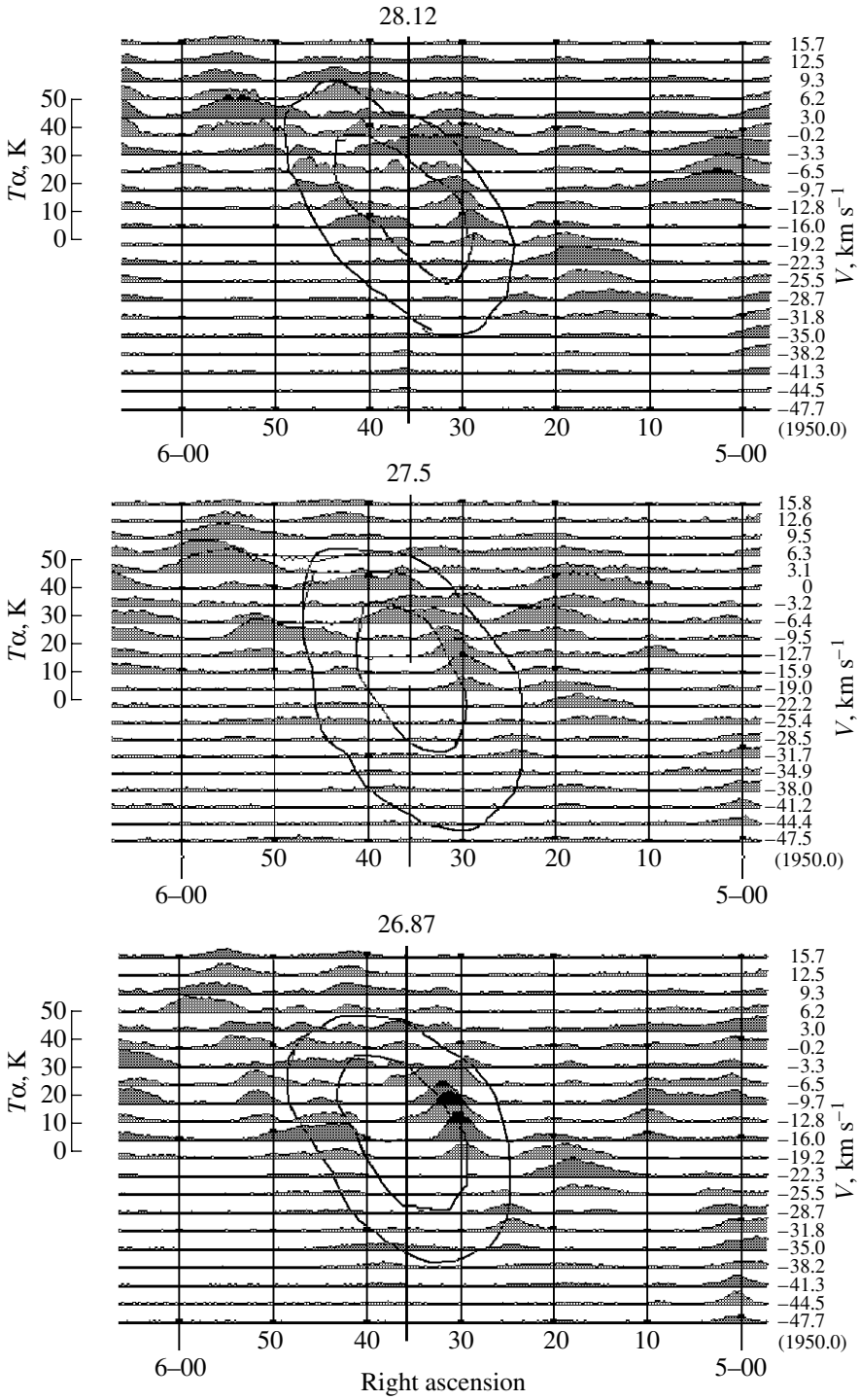

Fig. 1. (Contd.)

are also accessible in the Strasbourg database. In this region, two isolated CO clouds are clearly seen at radial velocities of −10 and +5 km s^{-1}. Unfortunately, we have no reasons to suggest an association of these molecular clouds with the H I shell or SNR.

To calculate the physical parameters of the shell, we must assume an SNR distance if we are sure that the H I features we detected are actually associated with the SNR, because the kinematic distance of the features cannot be determined from their radial velocities in the anticenter region. A summary of the previous distance estimates for this SNR based on the $\Sigma-D$ relation was given by Lozinskaya (1976). This distance is, on average, 1 kpc. After the detection

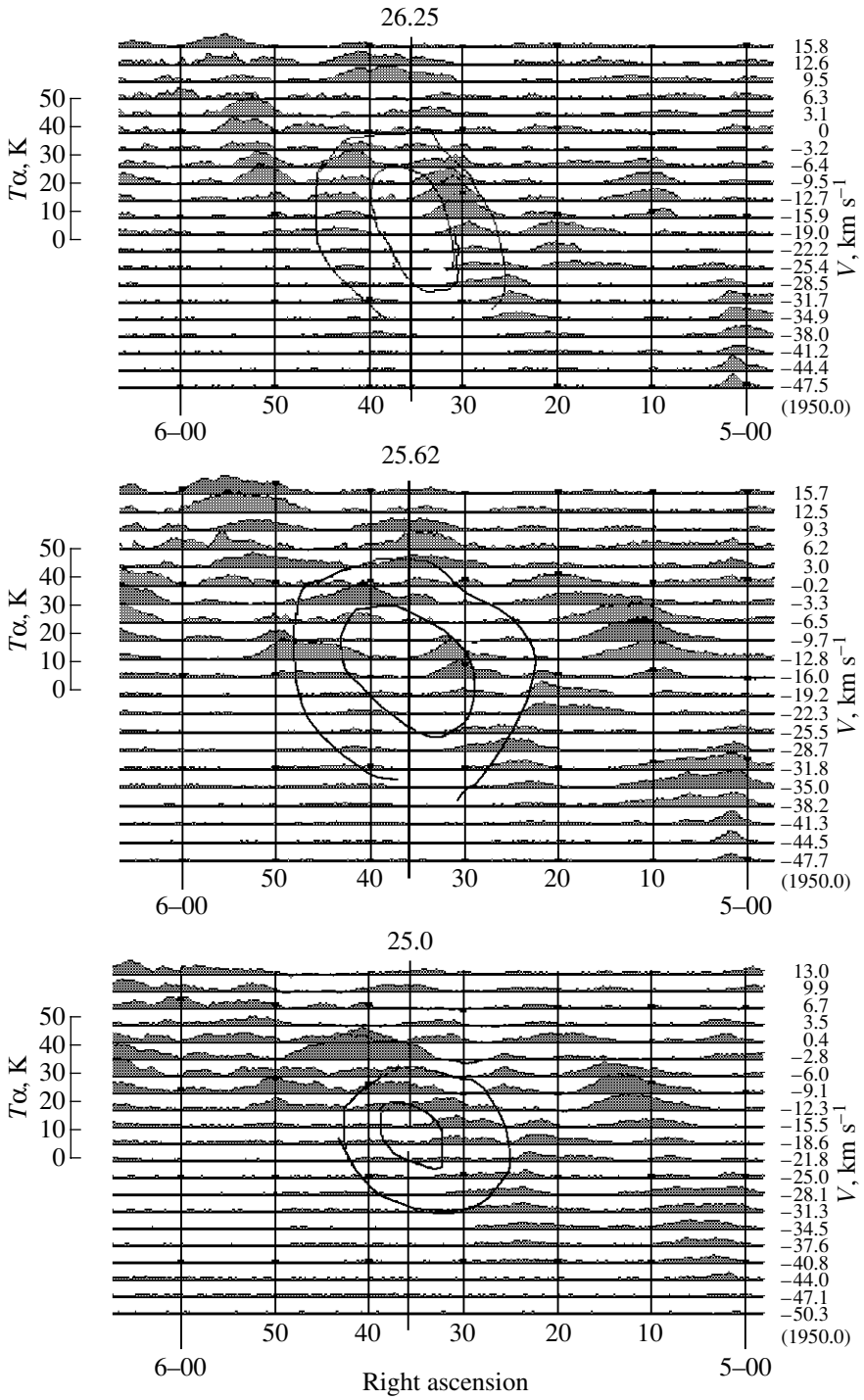

Fig. 1. (Contd.)

of the pulsar that is apparently associated with this SNR (Anderson *et al.* 1996), Case and Bhattacharya (1998) revised its distance to 1.5 kpc; they included S 147 in a small group of reference SNRs whose distances are considered to be known.

Given this distance, the physical parameters of the H I shell around the SNR S 147 are the following:

outer diameter 90 pc;
inner diameter 57 pc;
mean gas density 3.25 cm^{-3};
H I mass in the shell $2.2 \times 10^4 M_\odot$;
angular velocity -1.4×10^{-14} rad s^{-1}.

We determine the density of the ambient interstellar medium $n_0 \approx 2.35$ cm^{-3}, by assuming that

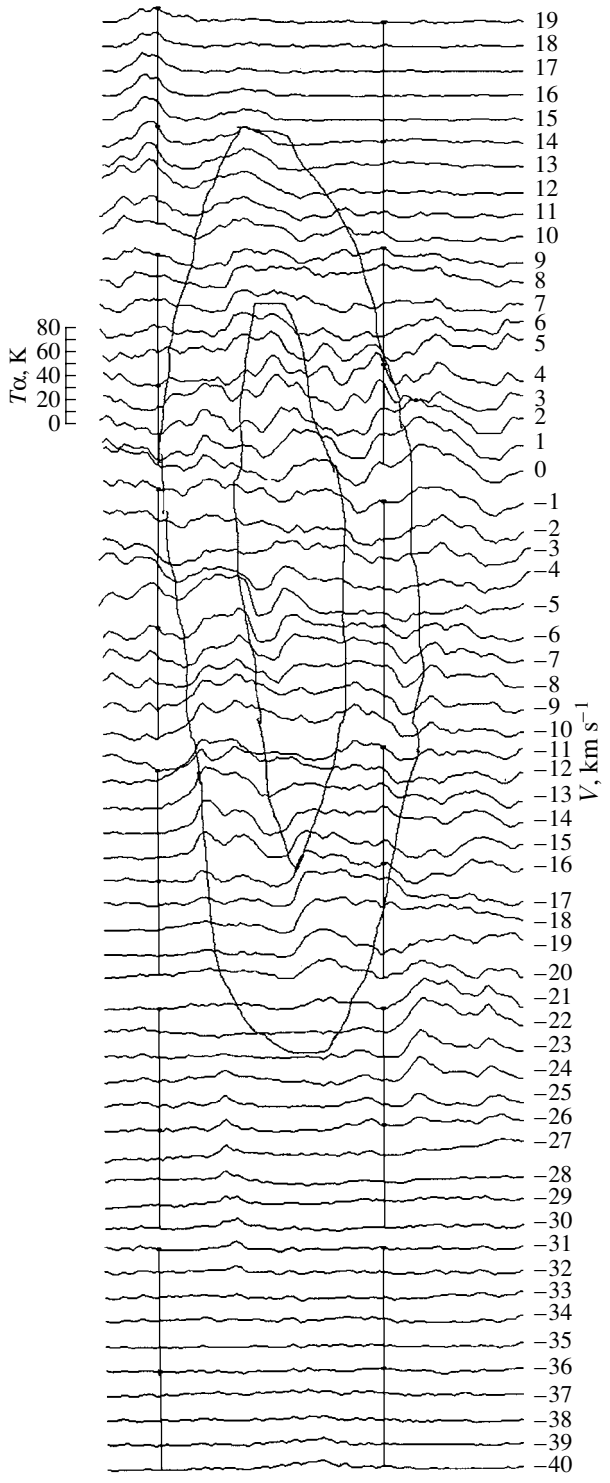

Fig. 2. The distribution of H I emission features, as constructed from the survey data by Westerhout and Wendlandt (1982). The drift curve in l–V coordinates at the Galactic latitude $b = -1.5°$ is shown. The extended background of the H I emission was subtracted; the thin lines trace the shell structure.

the gas of the H I shell was initially spread over its entire present volume. Then, using the formulas from Wheeler *et al.* (1980), we can estimate the initial explosion energy and the SNR age:

$$E_0 = 1.02 \times 10^{44} V_s^{1.27} n_0^{1.18} R_s^{3.16} \text{ erg},$$

$$t = t_{\rm rad} + 13 R_{\rm rad}^{5/2} (n_0/E_{51})^{1/2} [(R_s/R_{\rm rad})^{7/2} - 1] \text{ yr},$$

where $E_{51} = E_0/10^{51}$ erg; $R_{\rm rad}$ and $t_{\rm rad}$ are, respectively, the radius and initial time of the radiative SNR expansion phase:

$$R_{\rm rad} = 15.2 E_{51}^{0.29} n_0^{-0.43} \approx 13.0 \text{ pc},$$

$$t_{\rm rad} = 1.2 \times 10^4 E_{51}^{0.22} n_0^{-0.54} \approx 0.9 \times 10^4 \text{ yr}.$$

As a result, we obtain $E_0 = 2.2 \times 10^{51}$ erg and $t = 6.5 \times 10^5$ yr, which are typical of the old shell-type SNRs.

CONCLUSIONS

As was mentioned above, we cannot compare the parameters of the H I shell revealed by the RATAN-600 observations with the only mention of a similar shell around the SNR S 147 in Assousa *et al.* (1973, 1975), because, in effect, the results of the latter were not published. We can only confirm that there are no detectable H I features at negative radial velocities (< -50 km s^{-1}) in our data that could be related to the SNR S 147. Our data show that the shell is highly inhomogeneous in structure and is clearly seen only at low Galactic latitudes (the northern part of the SNR) and at positive velocities of its expansion. In general, such a structure comes as no surprise, because the size of the SNR itself is comparable to the thickness of the Galactic-gas layer ($\sim$100 pc) and the SNR is located almost 2° to the south from the maximum of the neutral-gas layer and, most likely, in front of it. It appears that the inhomogeneity of the ambient medium can also account for the variation in the radio spectral index across the SNR disk found by Fürst and Reich (1986). As for the shell rotation, it is probably the residual rotation of the gas cloud in which the supernova exploded. According to Phillips (1999) and Gosachinskij and Morozova (2000), rotation is typical of almost all molecular and atomic clouds of interstellar gas.

The total supernova explosion energy we obtained is close to the results by Lozinskaya (1976). However, the SNR age was found to be almost an order of magnitude larger than the one in this paper and it is much closer to the estimates based on the radio observations by Sofue *et al.* (1980) or Kundu *et al.* (1980).

By the parameters of the ambient gas, the SNR S 147 clearly belongs to the less than twenty SNRs

whose interaction with the ambient interstellar medium is beyond question; i.e., expanding shells of neutral hydrogen were detected around them [see, e.g., Gosachinskij and Khersonskij (1985)]. At present, we are searching for H I shells around more than 90 SNRs with angular diameters larger than 10′–15′ using RATAN-600. The results presented here are only a small part of this work.

ACKNOWLEDGMENTS

I am grateful to G.N. Il'in, I.F. Okunev, Z.A. Alferova, and T.V. Monastyreva from the Special Astrophysical Observatory for maintaining the equipment in an operational state and for help with the observations. This work was supported by the Russian Foundation for Basic Research (project no. 01-02-17154) and the Program "Astronomy" (project no. 2.1.2.6).

REFERENCES

1. Z. A. Alferova, I. V. Gosachinskij, S. R. Zhelenkov, and A. S. Morozov, Izv. SAO **23**, 89 (1986).
2. S. B. Anderson, B. J. Cadwell, B. A. Jacoby, *et al.*, Astrophys. J. Lett. **468**, L55 (1996).
3. G. E. Assousa, B. Balick, and J. W. Erkes, Bull. Am. Astron. Soc. **5**, 410 (1973).
4. G. E. Assousa, B. Balick, and J. W. Erkes, Bull. Am. Astron. Soc. **7**, 35 (1975).
5. G. L. Case and D. Bhattacharya, Astrophys. J. **504**, 761 (1998).
6. T. M. Dame, H. Ungerechts, R. S. Cohen, *et al.*, Astrophys. J. **322**, 706 (1987).
7. T. M. Dame, D. Hartmann, and P. Thaddeus, Astrophys. J. **547**, 792 (2001).
8. N. A. Esepkina, N. S. Bakhvalov, B. A. Vasil'ev, *et al.*, Izv. SAO **11**, 182 (1979).
9. E. Fürst and W. Reich, Astron. Astrophys. **163**, 185 (1986).
10. P. M. Gondhalekar and A. P. Phillips, Mon. Not. R. Astron. Soc. **191**, 13P (1980).
11. I. V. Gosachinskij and V. K. Khersonskij, Astrophys. Space Sci. **108**, 303 (1985).
12. I. V. Gosachinskij and V. V. Morozova, Astron. Zh. **76**, 883 (1999) [Astron. Rep. **43**, 777 (1999)].
13. D. A. Green, in *Proceedings of the IAU Colloquium No. 145 "Supernovae and Supermova Remmants", Xian, 1993,* Ed. by R. McCray and Z. Wang (Cambridge Univ. Press, Cambridge, 1996), p. 419.
14. G. N. Il'in, A. M. Pilipenko, and V. A. Prozorov, in *Proceedings of the XXVII Radio Astronomical Conference "Problems of Modern Radio Astronomy"* (IPA RAN, St. Petersburg, 1997), p. 128.
15. B.-C. Koo and C. Heiles, Astrophys. J. **382**, 204 (1991).
16. M. R. Kundu, P. E. Angerhofer, E. Fürst, and W. Hirth, Astron. Astrophys. **92**, 225 (1980).
17. T. A. Lozinskaya, Astron. Zh. **53**, 38 (1976) [Sov. Astron. **20**, 19 (1976)].
18. J. P. Phillips, Astron. Astrophys., Suppl. Ser. **134**, 241 (1999).
19. A. P. Phillips, P. M. Gondhalekar, and J. C. Blades, Mon. Not. R. Astron. Soc. **195**, 485 (1981).
20. J. Silk and G. Wallerstein, Astrophys. J. **181**, 799 (1973).
21. Y. Sofue, E. Fürst, and W. Hirth, Publ. Astron. Soc. Jpn. **31**, 1 (1980).
22. S. van den Berg, A. P. Marscher, and Y. Terzian, Astrophys. J., Suppl. Ser. **26**, 19 (1973).
23. A. P. Venger, I. V. Gosachinskij, V. G. Grachev, and N. F. Ryzhkov, Izv. SAO **14**, 118 (1981).
24. A. P. Venger, V. G. Grachev, T. M. Egorova, *et al.*, Soobshch. SAO, No. 35, 5 (1982).
25. G. Westerhout and H. U. Wendlandt, Astron. Astrophys., Suppl. Ser. **49**, 137 (1982).
26. J. C. Wheeler, T. J. Masurek, and A. Sivaramakrishnan, Astrophys. J. **237**, 781 (1980).

Translated by G. Rudnitskii

Astronomy Letters, Vol. 28, No. 5, 2002, pp. 310–315. Translated from Pis'ma v Astronomicheskiĭ Zhurnal, Vol. 28, No. 5, 2002, pp. 356–361.

Observational Effects in Supernova Remnants Associated with H II Regions and Dense Gaseous Clouds

S. O. Tagieva*

Institute of Physics, Academy of Sciences of Azerbaijan, pr. Dzhavida 33, Baku, 370143 Azerbaijan

Received September 14, 2001; in final form, December 6, 2001

Abstract—The dependences of various parameters for S- and C-type supernova remnants (SNRs) on their diameters are investigated. Only SNRs with $D \leq 40$ pc that expand initially within H II regions and, subsequently, in dense media are considered. The expansion velocities and thermal electron densities of these SNRs were found to decrease with increasing diameter, on average, as D^{-1} and $D^{-0.5}$, respectively. H II regions hamper the detection of SNRs; this effect is particularly pronounced in regions with $270° \leq 1 \leq 300°$ and $330° \leq 1 \leq 360°$. The X-ray luminosities of SNRs born in dense media increase by an order of magnitude when their diameters reach ~30 pc. After the SNR diameters reach ~40 pc, their radio and X-ray luminosities decrease sharply. © *2002 MAIK "Nauka/Interperiodica"*.

Key words: *supernovae and supernova remnants*

INTRODUCTION

The observational parameters of supernova remnants (SNRs) depend on the supernova explosion energy (on the expansion kinetic energy of the explosion matter), on the mean density of the ambient diffuse matter and the presence of various types of clouds (molecular, H I, and H II), and on the SNR age. These parameters vary over wide ranges: the characteristic matter expansion energies range from 5×10^{49} to 10^{51} erg, the matter densities range from 0.01 to 10^5 cm^{-3}, and the sizes range from 3–5 to 50 pc. Therefore, the SNR shapes, sizes, expansion velocities, surface radio brightnesses, X-ray luminosities, and lifetimes not only differ greatly from one another, but also change during the expansion to a much greater extent. SNR brightness is also affected by the genetically associated active neutron star.

Here, we investigate the variations in parameters of (shell-type and combined) SNRs in the course of their evolution and the influence of H II regions on the possibility of their detection.

DEPENDENCES OF THE SHOCK-FRONT EXPANSION VELOCITY V, THERMAL-ELECTRON DENSITY n_e, MAGNETIC INDUCTION B, AND SPECTRAL RADIATION DENSITY j_ν IN SNR SHELLS ON THEIR DIAMETERS

We know from the theory of synchrotron radiation that the volume radiation density at a given frequency (spectral radiation density) is given by the formula (Ginzburg 1979)

$$j_\nu = 1.35 \times 10^{-27} b(\alpha) \times (6.26 \times 10^4)^\alpha K_e B_{-5}^{\alpha+1} \nu_9^{-\alpha}, \quad \text{erg cm}^{-3}\,\text{s}^{-1}\,\text{sr}^{-1}\,\text{Hz}^{-1}. \tag{1}$$

Here, $b(\alpha)$ is a constant specified in tabular form; B_{-5} is the magnetic induction, 10^{-5} G; ν_9 is the radiation frequency, 10^9 Hz; and K_e is the constant in the energy spectrum of ultrarelativistic electrons

$$N_e dE = K_e E^{-\gamma} dE \text{ el. cm}^{-3}, \tag{2}$$

where $\gamma = 2\alpha + 1$.

At the SNR shock fronts, the electrons are accelerated with a high probability to ultrarelativistic energies by a regular acceleration mechanism, the Bell–Krymskii mechanism (Bell 1978a, 1978b; Krymskii 1977). This mechanism allows the electron number density and the energy spectrum to be estimated as a function of the velocity of a strong shock front and the postshock thermal-electron density. The numerical value of K_e in Eq. (2) depends on the density of the X-ray-emitting thermal electrons at the shock (n_e) and on the shock-front velocity (V) as follows:

$$K_e \sim n_e V^{2\alpha}. \tag{3}$$

Therefore, Eq. (1) for the spectral radiation density in the case of electron acceleration at the SNR shock fronts by the regular mechanism takes the form

$$j_\nu = 9.69 \times 10^{-30} (3.41 \times 10^{-9})^\alpha b(\alpha) \tag{4}$$

*E-mail: physic@lan.ab.az

Table 1. S- and C-type SNRs with $D \leq 40$ pc with the most reliable data on D, V, n_e, and B

l, deg	b, deg	Name	D, pc	V, 10^7 cm s^{-1}		n_e, cm^{-3}		B, 10^{-6} G	
111.7	−2.1	Cas A	4.1	∼50–100	[12, 36, 25]	8	[1]		
120.1	+1.4	Tycho	7.7	45	[35]	2–3	[41]		
332.4	−0.4	RCW 103	11	≈30	[17, 19]				
31.9	+0.0	3C 391	13	6.7	[37]	5–10	[37]		
39.2	−0.3	3C 396	15					200	[42]
34.7	−0.4	W 44	25	1.5	[23]	1–6	[23]	200	[42]
78.2	+2.1	DR 4	26	10	[30]	≥ 4	[28]		
260.4	−3.4	Puppis A	29	7–18	[9, 15]	0.5–3	[35, 8]		
6.4	−0.1	W 28	31	6	[37]	0.23–4	[37, 22]	200	[24]
315.4	−2.3	RCW 86	34	8	[35]	1	[35]		
119.5	+10.2	CTA 1	37	4	[39]	0.08	[42]	3	[42]
320.4	−1.2	RCW 89	41					8	[33]
326.3	−1.8		35	45	[18]	0.4	[20]		
263.9	−3.3	Vela	36	1.1	[10]			60	[16]

$$\times \Phi_e \alpha n_e V_8^{2\alpha} B_{-5}^{\alpha+1} \nu_9, \text{ erg cm}^{-3}\text{ s}^{-1}\text{ sr}^{-1}\text{ Hz}^{-1}.$$

Here, V_8 is the shock-front velocity in units of 10^8 cm s^{-1} and Φ_e is the constant of the Bell–Krymskii acceleration mechanism. As we see from Eq. (4), the spectral radiation density [for the constant spectral index $\alpha = 0.5$ typical of shell-type (S) and combined (C) SNRs] is related to n_e, V, and B by

$$j_\nu \sim n_e V B^{1.5}. \quad (5)$$

Using X-ray, optical, and radio data on SNRs, Allahverdiyev *et al.* (1986) showed that, in general, the following relations hold for S- and C-type SNRs:

$$n_e \sim D^{-1.2}, \quad V \sim D^{-0.9}, \quad B \sim D^{-1}. \quad (6)$$

Since the data on SNRs have been significantly enriched in recent years, we have attempted to refine the dependences of the shock-front velocity V and mean electron density n_e in the shell on the SNR diameter. We restricted our analysis to SNRs with diameters $D < 40$ pc, because in most cases, SNRs with larger diameters expand in tenuous media. On the other hand, SNRs with $D > 40$ pc are strongly affected by selection effects at distances >3–4 kpc. SNRs with large D are found nearby and mostly toward the Galactic anticenter. Below, we use the SNR distances from Ankay *et al.* (2002).

Table 1 gives observational data on the shock-front expansion velocities V, on the thermal-electron densities n_e in the shells, and on the mean magnetic-field strengths B in the shells in order of increasing diameters of S- and C-type SNRs. Using these data, we derived the following relations:

$$V \sim D^{-1.3\pm0.3}, \quad n_e \sim D^{-0.9\pm0.4}. \quad (7)$$

The derived relations have significant uncertainties, because these quantities are estimated with large errors. We failed to find any dependence of B on D using the data from the table, because these are few in number and unreliable (see Table 1). However, we can find it in a different form if the $\Sigma \sim D^{-2.38}$ relation (6) is used.

The radio emission is known to originate mainly from the SNR shell, which accounts for the Ath fraction of the entire SNR volume. Since the filling factor A can, in principle, change from SNR to SNR and for an individual SNR during its expansion,

$$F = \frac{A}{24}\frac{jD^3}{d^2}, \quad \Sigma = \frac{F}{\theta^2} \sim AjD. \quad (8)$$

Using the Σ–D relation and expressions (5) and (7), we obtain

$$B \sim D^{-0.8}. \quad (9)$$

Naturally, observational data must be accumulated to construct the B–D relation, Next, by comparing this relation with expression (9), we can judge whether the derived relations (7) and (9) are valid.

Table 2. The distribution of O stars in Galactic longitude and in distance from the Sun

d, kpc	l, deg											
	0–30	30–60	60–90	90–120	120–150	150–180	180–210	210–240	240–270	270–300	300–330	330–360
≤1	1	–	7	11	1	1	9	1	4	–	2	3
≤2	31	1	41	21	10	6	25	11	9	18	13	34
≤3	58	4	69	37	48	14	34	15	19	64	24	77
	37	3	41	17	27	8	19	7	13	39	18	57
≤4	66	5	73	44	60	17	36	20	29	89	25	80
	43	4	45	24	34	10	19	9	17	57	19	59
≤4	–	144	–	–	121	–	–	85	–	–	194	
		92			68			45			135	

Table 3. The distribution of S- and C-type SNRs with diameters $D \leq 40$ pc in Galactic longitude and in distance from the Sun

d, kpc	l, deg											
	0–30	30–60	60–90	90–120	120–150	150–180	180–210	210–240	240–270	270–300	300–330	330–360
≤1	–	–	1	–	–	–	–	–	1	–	–	–
≤2	–	–	3	2	–	–	1	–	2	1	2	–
≤3	4	1	4	3	1	–	1	–	2	1	6	1
≤4	7	2	4	4	2	–	1	–	2	1	6	1
≤4	–	12	–	–	6	–	–	3	–	–	8	–

COMPARISON OF THE SPATIAL DISTRIBUTIONS OF S- AND C-TYPE SNRs WITH $D \leq 40$ pc AND O STARS

SNRs projected onto bright H II regions or born inside them are known to be more difficult to detect than SNRs that are not associated with such regions. Below, we attempt to estimate the extent to which this selection effect influences SNR detection. To this end, we compare the Galactic distributions of O stars at distances up to 4 kpc with the distributions of S- and C-type SNRs with the same distances.

Table 2 presents the distributions of O stars in Galactic longitude and in distance from the Sun. The data were taken from the catalog of O stars by Cruz-Gonzalez *et al.* (1974). The upper rows give the distributions of all O stars in Galactic longitude and in distance from the Sun. The lower rows give the same distributions but only for stars of spectral type O7 or earlier and for O stars classified as giants and supergiants. We see from Table 2 that the fraction of such luminous O stars toward the Galactic center is much larger than that toward the Galactic anticenter. If the star-formation function in the massive part is, on average, the same in both directions, then this ratio reflects the selection effect. Clearly, strong absorption in the inner Galactic arms and, in general, toward the Galactic center hampers the detection of less luminous O stars and leads to the selection effect.

Table 3 gives the distributions of S- and C-type SNRs with diameters $D \leq 40$ pc ($\Sigma \geq 25 \times 10^{-22}$ W^2 Hz^{-1} sr^{-1}) in Galactic longitude and in distance from the Sun (Ankay *et al.* 2002).

Since the SNR progenitors are main-sequence stars with masses $M > 7$–$8\ M_\odot$ (Aydin *et al.* 1996), they must be born more frequently where O stars are concentrated. As we see from Table 2, 338 of the 544 O stars (62%) within $d \leq 4$ kpc of the Sun are located toward the Galactic center. Massive O stars are concentrated in this direction to an even greater extent: 227 of 340, i.e., 67%.

As we see from Table 3, 21 of the 30 SNRs (i.e., 70%) with $D \leq 40$ pc and distances $d \leq 4$ kpc are located toward the Galactic center. Thus, the fraction of SNRs with high surface radio brightnesses and distances up to 4 kpc toward the Galactic center is as large as the fraction of all O stars. However, the overwhelming majority of fainter SNRs lie toward the Galactic anticenter. In most cases, the diameters of SNRs with surface radio brightnesses $\Sigma <$

Table 4. The X-ray luminosities of S- and C-type SNRs and the observed energy ranges

l, deg	b, deg	Name	D, pc	L_x, 10^{-35} erg s^{-1} (ΔE, keV)		
11.2	−0.3		6.9	0.5	(1–10)	[45]
120.1	+1.4	Tycho	7.7	8.9	(1.5–4.5)	[34]
27.4	+0.0		10.5	2	(0.3–4)	[40]
332.4	−0.4	RCW 103	11	88	(0.1–2.4)	[11]
31.9	+0.0	3C 391	13	17	(0.1–2.4)	[38]
		N49 LMX	16	63	(0.5 – 5)	[46]
189.1	+3.0	IC 443	19.6	2.1	(0.2–4)	[4]
34.7	−0.4	W 44	25	80	(0.1–2.4)	[23]
260.4	−3.4	Puppis A	29	170	(0.1–2.4)	[11]
6.4	−0.1	W 28	31	400	(0.1–2.4)	[37]
119.5	+10.2	CTA 1	37	0.6	(0.1–2.4)	[41]
320.4	−1.2	RCW 89	41	0.2	(0.1–2.4)	[14]
109.1	−1.0	CTB 109	40.6	10	(0.1)	[31]

10^{-22} W^2 Hz^{-1} sr^{-1} are $D > 40$ pc. They expand in comparatively homogeneous media with a low density ($n \approx 0.1$–0.4 cm^{-3}). We see from our Σ–D relation (Ankay *et al.* 2002) that a surface brightness $\Sigma \geq 25 \times 10^{-22}$ W^2 Hz^{-1} sr^{-1} is reached for SNR diameters of ~38 pc. CTB 80 and HC 40 with ages of $\sim 2 \times 10^4$ yr are known to be among the well-studied SNRs with such diameters and similar surface radio brightnesses.

Let us determine how the selection effects influence the above ratios as the distance from the Sun increases (naturally, the selection effects for bright SNRs cannot be significant at the distances under consideration). The number of O stars with distances up to 3 kpc is given in the first line of the third row in Table 2. As we see from Table 2, 296 of the 442 O stars (i.e., 67%) lie toward the Galactic center. For the stars of spectral type O7 or earlier and for the giants and supergiants, these numbers are 276 and 185, respectively, which is also 67%. If these numbers are compared with those given above (for d up to 4 kpc), then the selection effects may also be said to be marginal for the O stars within 4 kpc of the Sun.

We pointed out above that the fraction of SNRs with $\Sigma \geq 25 \times 10^{-22}$ W^2 Hz^{-1} sr^{-1} located toward the Galactic center is almost the same as the fraction of all O stars. However, if we compare the number of SNRs with the number of O stars at distances up to 3 and 4 kpc in different Galactic-longitude intervals, then we will see virtually no SNRs in the intervals $l = 270°$–$300°$ and $l = 330°$–$360°$, where the number of O stars is largest (see Tables 2, 3). This deficit of SNRs in places where many O stars are located can be explained by the following selection effect. O stars are surrounded by H II regions with different diameters but, in most cases, with $D < 50$ pc and $\Sigma > 10^{-21}$ W^2 Hz^{-1} sr^{-1}. When the H II regions (produced by O stars) are projected onto SNRs and when SNRs develop inside large H II regions, the SNRs become virtually undetectable. On the other hand, the density of the medium generally increases toward the Galactic center. Therefore, the SNRs with $D \leq 40$ pc in this direction must be brighter on average. This effect results in a partial compensation for the selection effect discussed above.

AN INCREASE IN THE X-RAY LUMINOSITY OF SNRs WHEN THEIR DIAMETERS REACH THE SIZES OF H II REGIONS AND A FURTHER SHARP REDUCTION IN THE X-RAY AND RADIO LUMINOSITIES

Many years ago, Lozinskaya (1986) hypothesized that the expansion velocity of an SNR expanding inside an H II region must abruptly decrease after its collision with the boundary of the H II region. Naturally, the SNR will subsequently expand in an H I region where the matter density is an order of magnitude higher than that inside the H II region. The matter behind the shock front will be ionized, and its density will increase by a factor of ~4. This, in turn, will cause a sharp increase in the cross section for thermal radiation of the hot gas through Coulomb interactions. Thus, the thermal X-ray radiation must increase in intensity. To make sure that this reasoning is correct, we considered the variations in X-ray luminosity with SNR diameter.

Table 4 lists the X-ray luminosities of SNRs with the most reliable diameters (distances). The observed energy ranges are given near the luminosities; in several cases, the luminosities were changed, because more accurate distances were obtained (Ankay *et al.* 2002).

As we see from Table 4, when the SNR diameters reach approximately 40 pc, their X-ray luminosity decreases sharply. The Σ–D relation shows that when the SNR sizes reach 30–40 pc, the SNR synchrotron radio luminosity also decreases. This is because the shock-front velocity decreases sharply and because the rate of Coulomb losses and the ultrarelativistic electron energies greatly increase.

Since the SNR progenitors produce H II regions of different diameters, starting from several parsecs, the SNRs reach the boundaries of the H II regions with different velocities. As we see from Table 4, the X-ray luminosity of the SNR IC 433 is much lower than that of the other SNRs with similar diameters. This SNR, with the age $t \leq 7000$ yr, is expanding rapidly, as suggested by the high postshock temperature, $T = 1.2 \times 10^7$ K (Asoaka and Aschenbach 1994). That is why the electrons accelerated to energies $\sim$ TeV are observed (Keohane *et al.* 1997; Sturner *et al.* 1997; Asvarov *et al.* 1990).

The young SNR RCW 103, with an age of no more than 3×10^3 yr, has a high X-ray luminosity. However, it has a massive (dense) shell whose northern part interacts with molecular clouds (Dickel *et al.* 1996; Oliva *et al.* 1999; Braun *et al.* 1989).

CONCLUSIONS

(1) The ratio of the number of S- and C-type SNRs with diameters $D \leq 40$ pc to the number of O stars within 4 kpc of the Sun increases toward the Galactic center. However, this ratio is very small for SNRs in the intervals $270° \leq l \leq 300°$ and $330° \leq l \leq 360°$, where the number of luminous O stars (of early O types and supergiants) is particularly large. This is because the SNRs expanding inside the H II regions left from massive O stars are difficult to detect. The SNRs developing in a dense gaseous medium are easy to detect.

(2) Upon reaching a diameter of about 40 pc, the SNRs born in a dense medium at the final evolutionary stage of luminous O stars rapidly lose their radio luminosity and become undetectable. The reason is that the postshock matter density (the radiation through Coulomb interactions) greatly increases after the SNRs reach the sizes of the H II regions produced by their progenitors.

(3) The X-ray luminosity of the SNRs born in dense media increases by an order of magnitude when their diameters reach $\sim$30 pc. This is because the mass and density of their shells increase. After the SNRs reach a diameter of $\sim$40 pc, their X-ray luminosity decreases sharply.

(4) The expansion velocity of S- and C-type SNRs with diameters up to 40 pc in media with normal and high densities decreases, on average, as D^{-1}, while the postshock thermal-electron density decreases as $D^{-0.5}$.

REFERENCES

1. A. O. Allahverdiyev, A. I. Guseynov, and F. K. Kasumov, Astrophys. Space Sci. **123**, 237 (1986).
2. A. Ankay, O. H. Guseynov, A. Sezwr, and S. O. Tagyeva (2002) (in press).
3. I. Asoaka and B. Aschenbach, Astron. Astrophys. **284**, 573 (1994).
4. A. I. Asvarov, V. A. Dogiel, O. H. Guseinov, and F. K. Kasumov, Astron. Astrophys. **229**, 196 (1990).
5. C. Aydin, S. Ozdemir, O. H. Guseinov, *et al.*, Turk. J. Phys. **20** (1996).
6. A. R. Bell, Mon. Not. R. Astron. Soc. **182**, 147 (1978a).
7. A. R. Bell, Mon. Not. R. Astron. Soc. **182**, 443 (1978b).
8. G. D. Berthiaume, D. N. Burrows, G. P. Garmire, and J. A. Nousek, Astrophys. J. **425**, 132 (1994).
9. W. B. Blair, J. C. Raymond, and G. A. Kriss, Astrophys. J. Lett. **454**, L35 (1995).
10. F. Bocchino, A. Maggio, S. Sciortino, and J. Raymond, Astron. Astrophys. **359**, 316 (2000).
11. R. Braun, W. M. Goss, and A. G. Lyne, Astrophys. J. **340**, 355 (1989).
12. L. M. Carter, J. R. Dickel, and D. J. Bomans, Publ. Astron. Soc. Pac. **109**, 990 (1997).
13. R. A. Chevalier, R. P. Krishner, and J. C. Raymond, Astrophys. J. **235**, 186 (1980).
14. M. J. Claussen, W. M. Goss, D. A. Frail, and K. Desai, Astrophys. J. **522**, 349 (1999).
15. D. P. Cox, R. L. Shelton, W. Maciejewski, *et al.*, Astrophys. J. **524**, 179 (1999).
16. I. Cruz-Gonzalez, E. Reccilas-Cruz, R. Coestro, *et al.*, Rev. Mex. Astron. Astrofis. **1**, 211 (1974).
17. D. M. Dechristopher and B. F. Winkler, Astron. Astrophys., Suppl. Ser. **184**, 5608 (1994).
18. O. C. de Jager, A. K. Harding, and M. S. Strickman, Astrophys. J. **460**, 729 (1996).
19. J. R. Dickel, A. Green, T. Ye, and D. K. Milne, Astron. J. **111**, 340 (1996).
20. J. R. Dickel, D. K. Milne, and R. G. Strom, Astrophys. J. **543**, 840 (2000).
21. I. de Plessis, O. C. de Jager, S. Buchner, *et al.*, Astrophys. J. **453**, 746 (1995).
22. V. L. Ginzburg, *Theoretical Physics and Astrophysics* (Pergamon, Oxford, 1979; Nauka, Moscow, 1981).
23. C. Greiveldinger, S. Caucino, S. Massaglia, *et al.*, Astrophys. J. **454**, 855 (1995).
24. J. P. Hughes, I. Hayashi, and K. Koyama, Astrophys. J. **505**, 732 (1998).

25. N. E. Kassim, P. Hertz, and K. W. Weiler, Astrophys. J. **419**, 733 (1993).
26. J. Keohane, R. Petre, *et al.*, Astrophys. J. **484**, 350 (1997).
27. B. Koralesky, D. A. Frail, W. M. Goss, *et al.*, Astron. J. **116**, 1323 (1998a).
28. B. Koralesky, L. Rudnick, E. V. Gotthelf, and J. W. Keohane, Astrophys. J. Lett. **505**, L27 (1998b).
29. G. F. Krymskiĭ, Dokl. Akad. Nauk SSSR **234**, 1306 (1977) [Sov. Phys. Dokl. **22**, 327 (1977)].
30. T. L. Landecker, R. S. Roger, and L. A. Higgs, Astron. Astrophys., Suppl. Ser. **39**, 133 (1980).
31. T. A. Lozinskaya, *Supernovae and Stellar Wind in the Interstallar Medium* (Nauka, Moscow, 1986; American Inst. of Physics, New York, 1992).
32. T. A. Lozinskaya, V. V. Pravdikova, and A. V. Finoguenov, Pis'ma Astron. Zh. **26**, 77 (2000).
33. M. Morini, N. R. Robba, A. Smith, and M. van der Klis, Astrophys. J. **333**, 777 (1988).
34. E. Oliva, A. F. Moorwood, S. Drapatz, *et al.*, Astron. Astrophys. **343**, 943 (1999).
35. J. E. Reed, J. J. Hester, A. C. Fabian, and P. F. Winkler, Astrophys. J. **440**, 706 (1995).
36. P. B. Reid, PhD Thesis (1982).
37. E. M. Reynoso, M. G. Dubne, W. M. Goss, and E. M. Arnal, Astron. J. **110**, 318 (1995).
38. J.-H. Rho and R. Petre, Astrophys. J. **467**, 698 (1996).
39. J.-H. Rho, R. Petre, R. Pisarski, and L. R. Jones, MPE Rep. **263**, 273 (1996).
40. M. Rosado, P. Ambrocio-Cruz, E. Le Coarer, and M. Marcelin, Astron. Astrophys. **315**, 243 (1996).
41. K. Y. Sanbonmatsu and J. D. Helfand, Astron. J. **104**, 2189 (1992).
42. G. Seward, P. Gorenstein, and W. Tucker, Astrophys. J. **266**, 287 (1983).
43. G. Seward, T. M. Dame, R. A. Fesen, and B. Aschenbach, Astrophys. J. **449**, 681 (1995).
44. P. Slane, F. D. Seward, R. Bandiera, *et al.*, Astrophys. J. **485**, 221 (1997).
45. S. Sturner, J. Keohane, J. Skibo, *et al.*, Astron. Astrophys., Suppl. Ser. **191**, 4006 (1997).
46. K. Torii, H. Tsunemi, T. Dotani, and K. Mitsuda, Astrophys. J. Lett. **489**, L145 (1997).
47. J. Vink, M. C. Maccarone, J. S. Kaastra, *et al.*, Astron. Astrophys. **344**, 289 (1999).

Translated by V. Astakhov

Astronomy Letters, Vol. 28, No. 5, 2002, pp. 316–323. Translated from Pis'ma v Astronomicheskiĭ Zhurnal, Vol. 28, No. 5, 2002, pp. 362–369.

Statistics of High-Velocity Outflows in Regions of Massive Star Formation

I. I. Zinchenko*

Institute of Applied Physics, Russian Academy of Sciences, ul. Ul'yanova 46, Nizhni Novgorod, 603600 Russia

Received November 6, 2001

Abstract—Based on a SO and $C^{18}O$ survey of dense molecular-cloud cores in regions of massive star formation (selected by the presence of H_2O maser emission), we estimate the frequency of occurrence of high-velocity outflows in these regions and their parameters. The presence of extended SO-line wings (compared to $C^{18}O$) is considered to be indicative of outflows. We estimate the outflow parameters (mass, momentum, and kinetic energy) from optically thin $C^{18}O$ lines, which increases the reliability of these estimates. According to this approach, high-velocity outflows were detected in ~40% of the observed objects, which is a lower limit on the frequency of their occurrence. There is a clear correlation between the outflow mass, momentum, and kinetic energy, on the one hand, and the bolometric luminosity of the associated infrared sources, on the other hand. The slope of the correlations is close to unity. Their comparison with similar correlations of the mass-loss rate, force, and mechanical luminosity with the bolometric luminosity shows that the spread in outflow dynamical age is small and that this age has no systematic correlation with the infrared luminosity. The mean outflow dynamical age that can be obtained from this comparison is $\sim 7 \times 10^3$ yr. © *2002 MAIK "Nauka/Interperiodica".*

Key words: *interstellar medium, gaseous nebulae*

INTRODUCTION

High-velocity bipolar molecular outflows generally mark an important stage of low-mass star formation [see, e.g., Bachiller (1996) for a review]. These are currently believed to carry away excess angular momentum from a contracting cloud, thereby making it possible for mass to be accumulated by the central core via accretion (Shu *et al.* 1987).

As for massive ($M > 8M_\odot$) stars, the protostellar cores with masses $\gtrsim 10M_\odot$ were shown to produce a sufficient radiation pressure to stop the spherical contraction (Wolfire and Cassinelli 1987). This led Bonnell *et al.* (1998) to suggest that such stars could be formed through the coalescence of low- and intermediate-mass stars (Bonnell *et al.* 1998). However, since the contraction is probably anisotropic, it appears that massive stars can still be formed via accretion. Observational data do not yet allow a final choice to be made between these models. Observations of molecular outflows that are closely related to accretion can help in settling this question.

To date, several surveys of molecular outflows have been carried out toward intense infrared sources and ultracompact H II regions, which are indicative of massive star formation. These were all conducted in lines of the main CO isotope, and in most cases, the objects were not mapped (Snell *et al.* 1988, 1990; Wilking *et al.* 1989; McCutcheon *et al.* 1991; Shepherd and Churchwell 1996; Osterloh *et al.* 1997). Broad CO-line wings were detected in a large fraction (from 40 to 90%) of the objects studied. However, since CO emission is observed everywhere and since the lines are optically thick, non-Gaussian line profiles reminiscent of broad wings can arise from a superposition of emissions from the various sources within the antenna beam, particularly in the inner Galaxy. This problem can be overcome by mapping objects (Zhang *et al.* 2001) or by using tracers of high-velocity gas other than CO.

Another problem in the studies of bipolar outflows is related to estimating their physical parameters. In general, these parameters are also estimated from lines of the main CO isotope. However, because of the large and, moreover, uncertain optical depth in these lines, the reliability of these estimates is questionable.

Recently, we have carried out a survey of H_2O masers (which are also indicative of massive star formation) in HNCO, $C^{18}O$, SO, and other lines [our results were published in part in Zinchenko *et al.* (2000)]. We selected objects with a sufficiently strong CS emission, suggesting the presence of a large amount of dense gas. The abundance of some molecules, in particular, SO, greatly increases behind

*E-mail: zin@appl.sci-nnov.ru

1063-7737/02/2805-0316$22.00

the shock fronts produced by high-velocity outflows. As a result, these can be good tracers of outflows that are unaffected by confusion such as CO. The outflow parameters themselves can be determined from $C^{18}O$ lines, which are definitely optically thin. Henning *et al.* (2000) provided such estimates for one of the objects from the sample under consideration.

In this paper, we analyze data from this survey in order to reveal high-velocity outflows and estimate the outflow parameters from optically thin $C^{18}O$ lines.

OBSERVATIONS AND THEIR ANALYSIS

The above survey of H_2O masers covered the northern and southern hemispheres alike. Here, we restrict our analysis to the observations of southern sources alone, because only these were simultaneously carried out in $C^{18}O$ and SO lines, i.e., definitely at the same point. These observations were performed with the SEST radio telescope in Chile. The instrument and equipment parameters, along with the observing procedure, were described previously (Zinchenko *et al.* 2000). A list of sources and their positions are also given in the above paper. This list includes 56 sources. Here, however, we do not consider such distinguished objects as Orion KL and Sgr A.

A comparison of the $C^{18}O$- and SO-line profiles for the remaining sources shows that the SO lines have broad wings in 23 of them, which may serve as compelling evidence for the presence of high-velocity outflows. The spectra of these sources are shown in Fig. 1. We fitted the $C^{18}O$-line profiles for them with two-component Gaussian curves, as was done by Henning *et al.* (2000). In all cases, the component widths differed greatly. Next, a narrow Gaussian component was subtracted from the original $C^{18}O$ spectra. The remaining broad component can be identified with the high-velocity gas [see Henning *et al.* (2000) for a discussion]. We see from Fig. 1 that in most cases, it is satisfactorily fitted with a Gaussian.

Subsequently, these spectra were used to compute the basic high-velocity gas parameters: mass (M), momentum (P), and kinetic energy ($E_{\rm kin}$). This was done by analogy with Henning *et al.* (2000) but using the Gaussian fit rather than the spectrum itself. Given the good quality of this fit, this seems quite justifiable. Our estimates are listed in the table. We took the distances to the sources from spectrophotometric data and, where these were lacking, used the kinematic distances estimated from the measured radial velocities of $C^{18}O$. The energies are given in units of $L_\odot$ yr for a convenient comparison with the luminosities ($1 L_\odot$ yr $\approx 1.21 \times 10^{41}$ erg). No corrections were made for the projection effects.

Almost all of the observed masers lie near infrared IRAS sources. The last column in the table gives the luminosities of these sources.

DISCUSSION

As was pointed out above, the first question that we hoped to elucidate here was the following: How frequently do high-velocity outflows occur in the objects under study? It follows from a comparison of the $C^{18}O$- and SO-line profiles that these are present in 23 of the 54 sources observed, i.e., in $\sim$40% of them. This is a lower limit on the frequency of occurrence of high-velocity outflows, because outflows oriented at a large angle to the line of sight ($\sim\pi/2$) cannot be detected in this way. The above estimate lies within the range of other available estimates for the frequency of occurrence of such outflows in regions of massive star formation. It is worth noting that this estimate is appreciably lower than that obtained by Zhang *et al.* (2001) for a sample of intense infrared sources ($\sim$90%), which may be because the objects under study have a different evolutionary status.

When high-velocity outflows are investigated, such outflow parameters as the mass-loss rate ($\dot{M} = M/t$), force ($F = P/t$), and mechanical luminosity ($L = E_{\rm kin}/t$), where t is the so-called outflow dynamical age (see, e.g., Cabrit and Bertout 1990), are discussed most commonly. This age can be determined from the source maps. Since we mapped no sources, we cannot determine this parameter. Therefore, we will consider the quantities given in the table.

On the one hand, our estimates give lower limits for the corresponding quantities primarily because the objects were not mapped. In addition, we also disregarded the probable inclination of the outflow axis to the line of sight, which affects the momentum and kinetic-energy estimates. On the other hand, our technique for determining the parameters includes the part of the outflow emission that overlaps the cloud emission in radial velocity (i.e., the low-velocity part of the outflow emission). Most authors discard this emission, which, of course, yields smaller estimates of the parameters, primarily of the mass. Thus, Henning *et al.* (2000) obtained mass estimate for these two approaches that differed by a factor of 4. However, given the other uncertainties typical of this kind of estimates, this difference may be considered to be not all that significant. A common approach to estimating the parameters appears to be more important, which is held to here.

Our estimates of the outflow masses lie within the range $\sim$20 to $\sim$1000 $M_\odot$, in satisfactory agreement with published mass estimates for outflows from massive stars (Churchwell 1997). The other parameters also correspond to the available data.

Parameters of the broad Gaussian $C^{18}O$-line components and estimates of the high-velocity gas parameters in the sources. The rms errors of the line parameters (in units of the last decimal digit) are given in parentheses

l^*, deg	$\int T_{\rm mb}^{**} dv$, K km s^{-1}	ΔV, km s^{-1}	d, kpc	M, $M_\odot$	P, $M_\odot$ km s^{-1}	$E_{\rm kin}$, $L_\odot$ yr	$L_{\rm IR}$, $L_\odot$
261.64	4.34(28)	8.74(42)	2.40	39	1.18×10^2	4.56×10^4	5.82×10^3
267.94	7.94(45)	6.46(18)	1.70	36	7.99×10^1	2.28×10^4	–
270.26	1.24(11)	15.56(110)	3.40	22	1.21×10^2	8.30×10^4	2.68×10^4
285.26	2.76(22)	10.85(62)	4.70	96	3.56×10^2	1.71×10^5	4.30×10^5
294.97	3.92(20)	8.44(46)	2.40	35	1.03×10^2	3.83×10^4	2.03×10^4
300.97	9.58(50)	7.72(22)	2.00	60	1.59×10^2	5.44×10^4	4.18×10^4
301.12	11.64(23)	11.78(21)	4.40	358	1.43×10^3	7.46×10^5	2.45×10^5
308.80	6.16(39)	9.90(43)	2.90	82	2.77×10^2	1.21×10^5	2.50×10^4
318.05	7.76(46)	8.79(38)	3.70	168	5.03×10^2	1.96×10^5	3.37×10^4
324.20	8.42(35)	11.56(40)	6.90	637	2.50×10^3	1.28×10^6	4.70×10^5
326.47	3.18(44)	9.57(80)	3.10	48	1.58×10^2	6.68×10^4	1.52×10^4
328.81	33.30(87)	8.03(16)	3.10	508	1.38×10^3	4.92×10^5	1.92×10^5
329.03	3.21(19)	19.68(159)	3.10	49	3.27×10^2	2.85×10^5	1.16×10^4
330.88	12.36(69)	17.76(97)	4.20	346	2.09×10^3	1.64×10^6	2.56×10^5
337.40	6.87(58)	11.49(62)	3.40	126	4.92×10^2	2.50×10^5	9.31×10^4
340.06	20.87(66)	9.70(19)	4.20	585	1.93×10^3	8.27×10^5	1.73×10^5
345.00	3.62(236)	21.73(990)	3.20	58	4.34×10^2	4.18×10^5	7.84×10^4
345.01	13.67(97)	9.53(29)	2.10	95	3.10×10^2	1.31×10^5	6.54×10^4
345.51	12.71(35)	12.22(34)	2.50	126	5.23×10^2	2.83×10^5	8.97×10^4
348.73	15.33(47)	13.05(32)	2.40	140	6.21×10^2	3.59×10^5	2.04×10^5
351.41	16.03(60)	12.79(38)	1.70	73	3.19×10^2	1.81×10^5	7.77×10^4
351.58	16.65(29)	8.42(9)	6.80	1224	3.49×10^3	1.30×10^6	2.07×10^5
351.78	19.58(92)	11.91(36)	1.60	79	3.22×10^2	1.70×10^5	6.43×10^4

*l—Galactic longitude of the source; **$T_{\rm mb}$ is the brightness temperature in the main antenna lobe.

One of the questions discussed in the literature concerns the correlation between outflow parameters and luminosities of the central sources (stellar luminosity L_* or infrared bolometric luminosity $L_{\rm IR}$). Having analyzed the available data using their theoretical models, Cabrit and Bertout (1992) found close correlations between the force and mechanical luminosity, on the one hand, and the bolometric luminosity, on the other hand. However, they noted that these correlations could, in principle, result from the selection effect attributable to the Malmquist bias, i.e., missing faint sources at large distances (Ridge and Moore 2001). Consequently, before analyzing our data for such correlations, it would be reasonable to determine how strongly these are affected by the selection.

In Figs. 2 and 3, our estimates of the outflow masses and the infrared luminosities of IRAS sources are plotted against distance d. We see that the above selection clearly shows up at $d > 4$ kpc. Therefore, below, we separately consider a subsample of sources at distances $d > 4$ kpc.

In Figs. 4–6, the mass, momentum, and kinetic-energy estimates are plotted against the luminosity of the associated infrared sources; the data for objects with $d < 4$ and $d > 4$ kpc are marked differently. In all cases, there is a clear correlation, irrespective of whether the results for distant sources are taken into account. Our analysis shows that the slope of all three

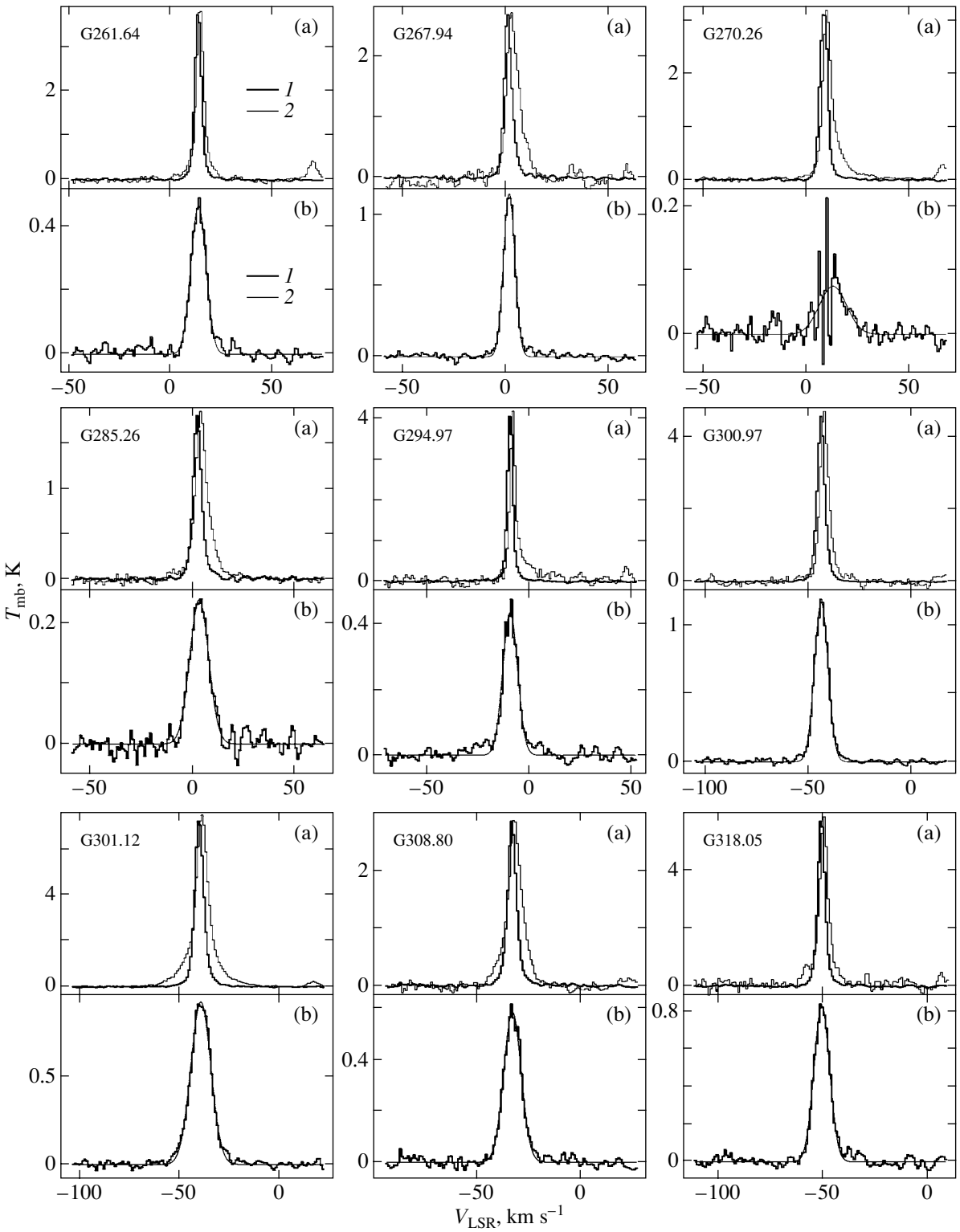

Fig. 1. (a) The measured $C^{18}O$ (*1*) and SO (*2*) spectra toward objects with signatures of high-velocity outflows. The peak SO-line intensities were scaled to the $C^{18}O$-line intensities. (b) The same $C^{18}O$ spectra after subtracting a narrow Gaussian component (*1*); (*2*) a Gaussian fit.

correlations is close to unity ($M \propto L_{IR}^{1.1 \pm 0.3}$, $P \propto L_{IR}^{0.9 \pm 0.2}$, $E_{kin} \propto L_{IR}^{1.2 \pm 0.3}$).

The correlations of the mass-loss rate, force, and mechanical luminosity with the infrared luminosity

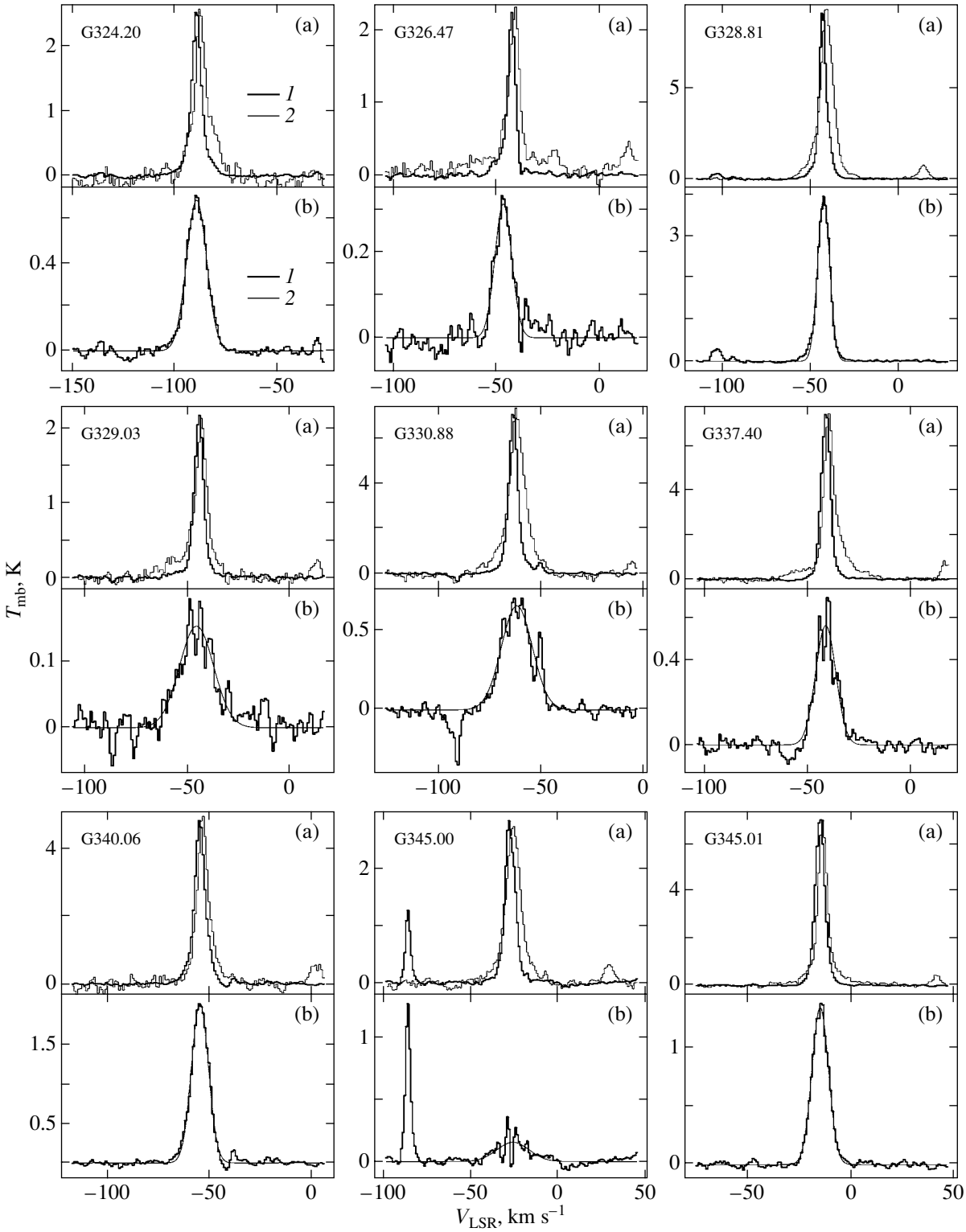

Fig. 1. (Contd.)

have approximately the same slope and a comparable dispersion. Thus it follows, in particular, that the spread in outflow dynamical age is small and that this age has no systematic correlation with the infrared luminosity. By comparing the derived $E_{kin}(L_{IR})$ correlation with the correlation between the mechanical and infrared luminosities, as inferred by Cabrit and Bertout (1992), we found the mean outflow dynamical

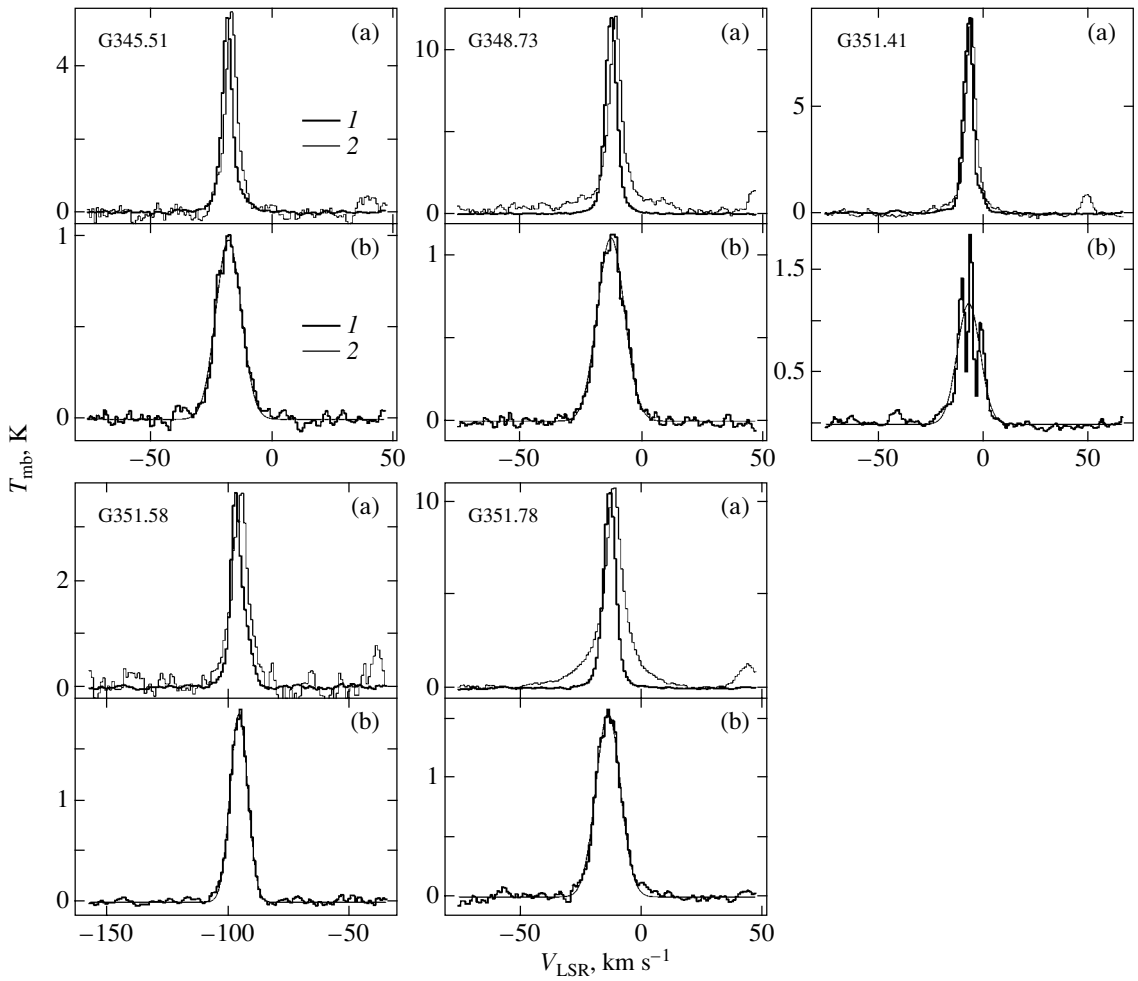

Fig. 1. (Contd.)

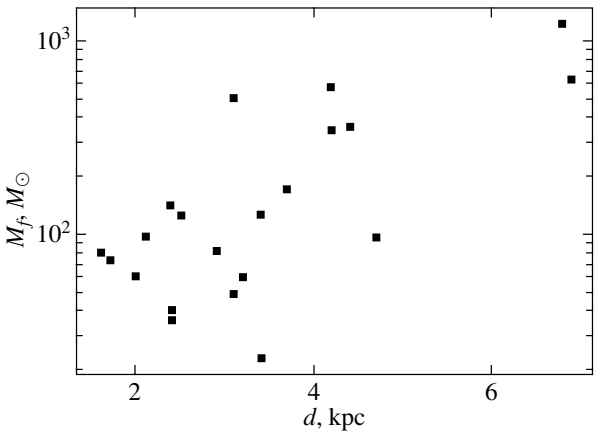

Fig. 2. Outflow-mass estimates versus distance.

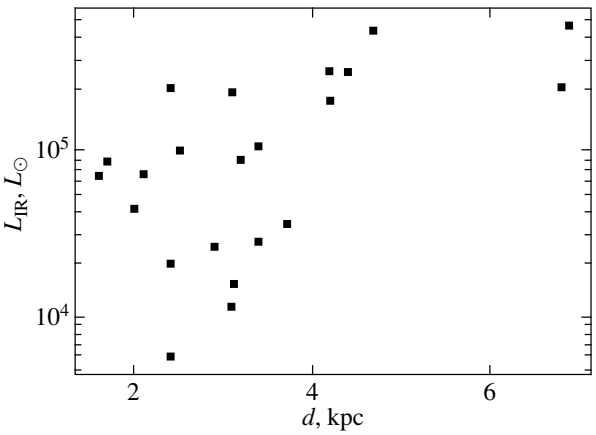

Fig. 3. Infrared-luminosity estimates for the IRAS sources in our sample versus distance.

age to be $\sim 2 \times 10^3$ yr. However, we disregarded the projection effects in our estimates. Taking the mean inclination of the outflow axis to the line of sight to be 57°.3 (Bontemps *et al.* 1996), we obtain a correction factor of $\sim$3.4; i.e., the dynamical-age estimate increases to $\sim 7 \times 10^3$ yr, which is close to its typical values (Padman *et al.* 1997; Ridge and Moore 2001).

The small spread in outflow dynamical age can be seen, for example, in Ridge and Moore (2001),

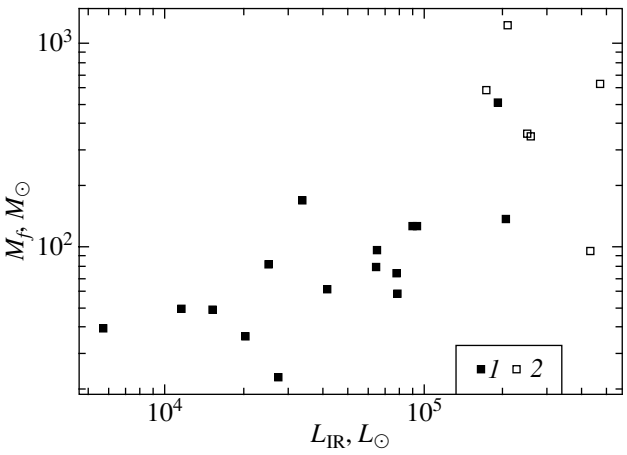

Fig. 4. Outflow-mass estimates versus luminosity of the associated infrared IRAS sources: *1* objects with $d < 4$ kpc, *2* objects with $d > 4$ kpc.

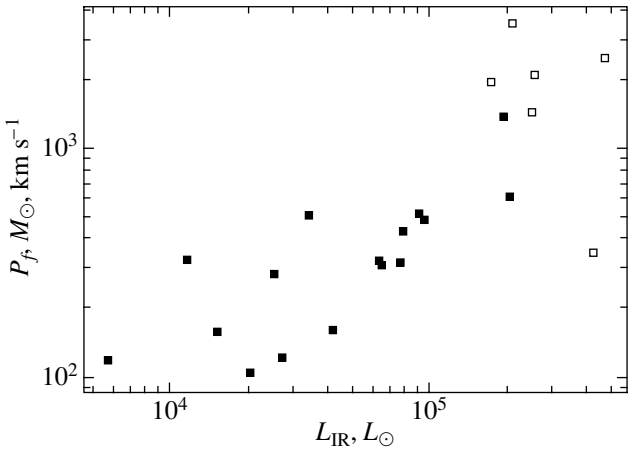

Fig. 5. Outflow-momentum estimates versus luminosity of the associated infrared IRAS sources. The notation is the same as in Fig. 4.

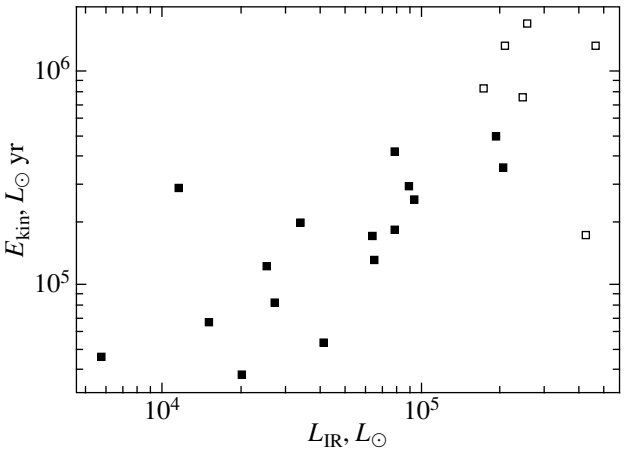

Fig. 6. Estimates of the outflow kinetic energy versus luminosity of the associated infrared IRAS sources. The notation is the same as in Fig. 4.

suggesting that younger and older outflows either were not included in the samples under study or are undetectable for some reason. Our selection criterion was the presence of H_2O masers and a sufficiently strong CS emission, while the selection criterion in Ridge and Moore (2001) was a sufficiently intense infrared emission. In general, however, almost all objects from our sample are also associated with intense infrared sources. Since outflows are observed toward most of the intense infrared sources and H_2O masers, we may conclude that the peak of infrared emission and maser activity probably corresponds to this evolutionary stage.

CONCLUSIONS

Having analyzed the results of our $C^{18}O$ and SO survey of H_2O masers, we identified objects with signatures of high-velocity molecular outflows (by the presence of appreciable SO-line wings compared to $C^{18}O$) and estimated the outflow parameters (mass, momentum, and kinetic energy). These estimates were obtained from optically thin $C^{18}O$ lines, which increases their reliability. Our main results are as follows:

(1) High-velocity molecular outflows are encountered in no less than 40% of the massive cores toward H_2O masers.

(2) There is a close correlation between the outflow mass, momentum, and kinetic energy, on the one hand, and the bolometric luminosity of the associated infrared source, on the other hand. The correlation coefficient is close to unity. A comparison of these correlations with similar correlations of the mass-loss rate, force, and mechanical luminosity with the bolometric luminosity shows that the spread in outflow dynamical age is small and that this age has no systematic correlation with the infrared luminosity. The mean outflow dynamical age derived from this comparison is $\sim 7 \times 10^3$ yr.

ACKNOWLEDGMENTS

This study was supported by the Russian Foundation for Basic Research (project no. 99-02-16556), INTAS (grant no. 99-1667), and NASA (the JURRISS Program, via CRDF RPO-841).

REFERENCES

1. R. Bachiller, Annu. Rev. Astron. Astrophys. **34**, 111 (1996).
2. I. Bonnell, M. R. Bate, and H. Zinnecker, Mon. Not. R. Astron. Soc. **298**, 93 (1998)
3. S. Bontemps, P. André, S. Terebey, and S. Cabrit, Astron. Astrophys. **311**, 858 (1996).

4. S. Cabrit and C. Bertout, Astrophys. J. **348**, 530 (1990).
5. S. Cabrit and C. Bertout, Astron. Astrophys. **261**, 274 (1992).
6. E. Churchwell, Astrophys. J. Lett. **479**, L59 (1997).
7. Th. Henning, A. Lapinov, K. Schreyer, *et al.*, Astron. Astrophys. **364**, 613 (2000).
8. W. H. McCutcheon, P. E. Dewdney, R. Purton, and T. Sato, Astron. J. **101**, 1435 (1991).
9. M. Osterloh, Th. Henning, and R. Launhardt, Astrophys. J., Suppl. Ser. **110**, 71 (1997).
10. R. Padman, S. Bence, and J. Richer, in *Proceedings of the IAU Symposium No. 182 "Herbig-Haro Flows and the Birth of Low Mass Stars,"* Ed. by B. Reipurth and C. Bertout (Kluwer, Dordrecht, 1997), p. 123.
11. N. A. Ridge and T. J. T. Moore, Astron. Astrophys. **378**, 495 (2001).
12. D. S. Shepherd and E. Churchwell, Astrophys. J. **472**, 225 (1996).
13. F. H. Shu, F. C. Adams, and S. Lizano, Annu. Rev. Astron. Astrophys. **25**, 23 (1987).
14. R. L. Snell, Y.-L. Huang, R. L. Dickman, and M. J. Clausser, Astrophys. J. **325**, 853 (1988).
15. R. L. Snell, R. L. Dickman, and Y.-L. Huang, Astrophys. J. **352**, 139 (1990).
16. B. A. Wilking, L. G. Mundy, J. H. Blackwell, and J. E. Howe, Astrophys. J. **345**, 257 (1989).
17. M. G. Wolfire and J. P. Cassinelli, Astrophys. J. **319**, 850 (1987).
18. Q. Zhang, T. R. Hunter, J. Brand, *et al.*, Astrophys. J. Lett. **552**, L167 (2001).
19. I. Zinchenko, C. Henkel, and R. Q. Mao, Astron. Astrophys. **361**, 1079 (2000).

Translated by V. Astakhov

Astronomy Letters, Vol. 28, No. 5, 2002, pp. 324–334. Translated from Pis'ma v Astronomicheskiĭ Zhurnal, Vol. 28, No. 5, 2002, pp. 370–381.

A Study of the Radial Velocity of the Star Θ^1 Ori C

É. A. Vitrichenko*

Space Research Institute, Russian Academy of Sciences, ul. Profsoyuznaya 84/32, Moscow, 117810 Russia

Received December 17, 2001

Abstract—The radial velocities of the star Θ^1 Ori C were measured from IUE spectra and are compared with published data. Two companions (C1 and C2) are assumed to be present. The probable periods for companion C1 can be estimated from the formula $P = 729.6/L$ days, where $L < 13$ is an integer. Radial-velocity curves were constructed for $L = 11$ and 12. The orbit turned out to be elliptical. At $L = 11$, the orbital elements are $P = 66.3(1)$ days, $\gamma = 10.9(2)$ km s^{-1}, $K = 6.1(4)$ km s^{-1}, $\omega = -2.88(5)$ rad, $e = 0.43(6)$, and Ep = JD 2449044.7(4). The errors in the last decimal digit are given in parentheses. Companion C2 was detected by temporal variations in the γ velocity of companion C1. Its orbit is assumed to be circular with the following elements: $P = 120(6)$ yr, $\gamma = 22(1)$ km s^{-1}, $K = 13(2)$ km s^{-1}, and Ep = 1911(3) yr. © *2002 MAIK "Nauka/Interperiodica".*

Key words: *stars, peculiarity, radial-velocity determination*

INTRODUCTION

Two of the four brightest Orion Trapezium stars are eclipsing systems: BM Ori = Θ^1 Ori B and V1016 Ori = Θ^1 Ori A. The brightest star, Θ^1 Ori C, exhibits photometric variability with the amplitude $\Delta V = 0^m.06$ (Kukarkin *et al.* 1982).

Frost *et al.* (1926) were the first to measure its radial velocity and discover its variability. Struve and Titus (1944) obtained a dense series of radial-velocity measurements but did not analyze it for variability. Conti (1972) obtained scarce, but highly accurate observations. The author concluded that the radial velocity was constant.

Stahl *et al.* (1993) obtained the largest series of dense, highly accurate measurements of the radial velocity determined from the photospheric C IV 5801 line. They found the radial velocity to be variable but made no attempt to construct the radial-velocity curve. It follows from their results that the period of the radial-velocity variations (if it exists) must be more than 40 days. Thus, it was shown that the radial velocity could not vary with the same period as the equivalent width of the Hα line for which a period of 15.43(3) days was found.

As yet none of the researchers has managed to detect a periodicity in the light or radial-velocity variations of the star.

A list of all radial-velocity studies is given in Table 1.

Since the observations by Frost *et al.* (1926) are two data sets widely spaced in time, each set was considered separately.

The observations in Table 1 should be broken down into two types. The first type includes dense series of highly accurate measurements with a sampling interval of ~1 days and an accuracy of ~1 km s^{-1}. The observations by Conti (1972), Stahl *et al.* (1993), and about half of our observations described below belong to these data. The second type includes less accurate measurements with an error of ~10 km s^{-1}.

Our study of the stellar continuum revealed three radiation sources. Apart from the primary star, the

Table 1. The radial velocity of Θ^1 Ori C

Reference	t, yr	N	γ, km s^{-1}	σ, km s^{-1}
Frost *et al.* (1926)	1905.8	11	22.3	4.9
Frost *et al.* (1926)	1925.1	12	24.8	3.6
Struve and Titus (1944)	1944.2	14	37.4	2.9
Conti (1972)	1972.1	13	24.9	1.1
Abt *et al.* (1991)	1978.1	20	17.0	2.5
Morrell and Levato (1991)	1982.7	6	9.2	4.4
Stahl *et al.* (1993)	1993.1	46	10.0	0.6
This paper, IUE	1995.6	14	10.4	0.8

Note. t is the mean epoch of observation, N is the number of radial-velocity measurements, γ is the mean radial velocity, and σ is its error.

*E-mail: vitrich@nserv.iki.rssi.ru

Table 2. A list of spectra

Spectrum number**	JD 2440000+*	N	V_r, km s^{-1}	σ_1, km s^{-1}	σ, km s^{-1}	g, Å	σ_1, Å	σ, Å
02768	3777.957	73	42.5	17	2.0	0.32	0.12	0.01
02769	3778.021	74	40.6	18	2.1	0.34	0.12	0.01
07481	4231.050	71	−2.5	14	1.6	0.29	0.10	0.01
09991	4485.201	69	16.8	15	1.8	0.32	0.14	0.02
13737	4711.564	77	5.4	14	1.6	0.30	0.11	0.01
13798	4719.310	78	1.7	14	1.6	0.36	0.17	0.02
14597	4816.501	63	27.7	15	1.9	0.31	0.14	0.02
14665	4822.300	58	7.4	12	1.7	0.30	0.08	0.01
15799	4957.556	58	2.9	12	1.7	0.34	0.11	0.01
16232	5001.914	56	6.1	13	1.7	0.29	0.12	0.02
19606	5426.547	61	10.0	12	1.6	0.31	0.11	0.01
48991	9283.921	58	15.5	12	1.5	0.32	0.10	0.01
48992	9283.995	60	15.3	15	2.0	0.34	0.11	0.01
54001	9777.660	77	8.9	15	1.7	0.32	0.11	0.01
54014	9778.666	70	9.8	12	1.4	0.28	0.07	0.01
54019	9779.730	59	5.7	13	1.7	0.33	0.13	0.02
54029	9780.651	61	8.2	15	2.0	0.32	0.11	0.01
54040	9781.651	59	5.0	13	1.7	0.30	0.08	0.01
54057	9783.656	58	11.1	13	1.7	0.33	0.09	0.01
54058	9783.676	56	9.5	12	1.7	0.32	0.11	0.01
54075	9785.761	55	7.9	12	1.6	0.33	0.09	0.01
54094	9787.645	60	12.2	11	1.5	0.30	0.11	0.01
54112	9789.671	81	13.6	14	1.5	0.28	0.09	0.01
54138	9791.655	84	11.8	14	1.5	0.31	0.11	0.01
54139	9791.676	84	11.6	16	1.7	0.29	0.10	0.01
54150	9792.650	79	15.1	14	1.5	0.29	0.10	0.01
54151	9792.671	81	15.5	11	1.2	0.29	0.09	0.01

Note. N is the number of measured lines; V_r is the radial velocity of the star; σ_1 and σ are the measurement errors of a single line and the mean radial velocity, respectively; g is the parameter of the Guassian fit to the line profile; and σ_1(Å) and σ(Å) are the errors of a single measurement and the mean result, respectively.

* According to the nomenclature of the IUE archive.

** Julian date for the mid-exposure.

sources with temperatures of 4000 and 190 K emit radiation (Vitrichenko 2000). The latter source can be a dust cloud or radiation from interstellar silicate particles, but the former source is definitely a star. On the Hertzsprung–Russell diagram, this source lies at the very beginning of the track (near the birth line) for a star of mass $15M_\odot$.

The star exhibits periodic variations in several physical parameters.

Variations in its spectrum were first detected by Conti (1972). The He II 4686 profile varied on a time scale of several days. The variations consisted in the appearance and disappearance of a violet-shifted emission component in the line. The spectral type of

Table 3. The radial velocity measured from interstellar lines

JD 2440000+	N	V_r, km s^{-1}	σ_1, km s^{-1}	σ, km s^{-1}	g, Å	σ_1, Å
3777.957	26	10.2	8.5	1.7	0.17	0.05
3778.021	28	10.2	9.1	1.7	0.18	0.05
4231.050	32	−1.7	8.5	1.5	0.19	0.06
4485.201	29	17.6	9.3	1.7	0.18	0.06
4711.564	27	0.0	8.1	1.6	0.18	0.04
4719.310	31	−5.4	9.0	1.6	0.18	0.05
4816.501	32	14.4	8.6	1.5	0.19	0.05
4822.300	31	1.1	7.3	1.3	0.18	0.05
4957.556	31	−4.7	9.1	1.6	0.20	0.06
5001.914	30	−1.6	8.1	1.5	0.21	0.06
5426.547	31	−0.7	8.7	1.6	0.19	0.05
9283.921	27	7.3	5.1	1.0	0.19	0.05
9283.995	33	7.1	10.6	1.8	0.22	0.08
9777.660	30	3.4	8.8	1.6	0.19	0.04
9778.666	27	2.3	8.5	1.6	0.18	0.05
9779.730	33	1.8	8.4	1.5	0.19	0.05
9780.651	30	2.8	9.6	1.8	0.20	0.05
9781.651	29	−0.1	8.9	1.7	0.19	0.05
9783.656	32	5.0	8.6	1.5	0.19	0.06
9783.676	30	2.8	9.4	1.7	0.19	0.05
9785.761	33	0.6	11.4	2.0	0.20	0.07
9787.645	30	1.8	10.0	1.8	0.20	0.05
9789.671	32	3.5	7.9	1.4	0.20	0.06
9791.655	29	2.1	9.0	1.7	0.19	0.05
9791.676	33	−0.1	9.3	1.6	0.18	0.04
9792.650	29	4.0	8.1	1.5	0.20	0.06
9792.671	30	2.5	7.9	1.4	0.19	0.05

the star was found to systematically change from O6 to O4 in seven days (Walborn 1981). Stahl *et al.* (1993) investigated the Hα emission component and found it to vary with a period of 15.4 days. Walborn and Nichols (1994) detected variations in the C IV 1548 and 1550 line profiles with a period of 15.41(2) days, which closely agrees with the variability period of the Hα emission. An interesting result was obtained by Gagne *et al.* (1997). They found the X-ray flux from the star to vary with a period of 16(4) days, which is consistent with the above period. To explain this phenomenon, Babel and Montmerle (1997) proposed a model of an oblique rotator with the magnetic induction $B = 300$ G at the stellar surface for Θ^1 Ori C.

Stahl *et al.* (1996) obtained the most accurate period of the spectral variations. The authors confirmed the results by Walborn and Nichols (1994): they investigated the behavior of the Hα and C IV 1548 and 1550 line equivalent widths and estimated their variability period to be $P = 15.422(2)$ days but attributed this periodicity to axial rotation of the star rather than to its binary nature.

The speckle interferometry by Weigelt *et al.* (1999) revealed companion C_2 at a distance of

0.03 arcsec from the primary star. They measured the magnitude $K = 5^m.95(11)$ and color index $H - K = 0^m.24(9)$ of the companion and obtained an upper limit on its mass, $M < 6M_\odot$, from its position on the Hertzsprung–Russell diagram.

In this paper, our objective is to analyze all the available and new measurements of the radial velocity in an effort to find the period of its variations.

RADIAL-VELOCITY MEASUREMENTS

All our measured spectra were taken with the SWP camera on the IUE satellite in the wavelength range 1150–1975 Å. To reduce the photometric noise, the spectra were filtered with a rectangular window whose width was calculated using the formula

$$\Delta\lambda = 0.00013\lambda. \quad (1)$$

The factor 0.00013 was chosen in such a way that the interstellar-line width increased by no more than ~5%, while the stellar-line width was virtually unaffected. The filtering reduced the photometric noise by a factor of 2–2.5.

A list of the studied spectra is given in Table 2.

An examination of Table 2 leads us to conclude that all radial-velocity measurements are homogeneous in accuracy and that the accuracy itself lies within the range 1.2 to 2.1 km s^{-1}.

We managed to identify a total of ~200 lines in the spectrum of Θ^1 Ori C. Only Fe IV lines were used to measure the radial velocity. These lines were chosen because they are certain to be photospheric (not interstellar ones and not subjected to chromospheric effects) and numerous. Almost half of all the identified lines belong to Fe IV. We performed the identification using the list of lines kindly provided by the Vienna Atomic Line Data (VALD) Center.

A list of the wavelengths of Fe IV lines (Å):

1253.81	1257.76	1270.76	1398.02	1430.52	1458.52	1464.70	1483.16
1489.54	1493.72	1495.18	1504.50	1517.78	1523.92	1526.07	1526.60
1530.26	1536.58	1538.29	1553.30	1557.46	1559.19	1560.27	1561.35
1563.58	1566.57	1568.28	1569.22	1570.28	1571.24	1574.74	1577.21
1577.78	1578.74	1585.84	1590.62	1592.05	1600.50	1601.82	1603.18
1604.88	1605.97	1609.10	1611.20	1612.60	1617.69	1623.53	1626.47
1628.54	1631.07	1632.41	1638.42	1641.86	1642.88	1647.09	1651.58
1652.90	1660.10	1662.52	1663.54	1668.07	1670.79	1673.68	1675.66
1681.29	1687.68	1698.88	1704.93	1707.35	1709.81	1711.41	1712.76
1722.71	1724.26	1725.63	1732.94	1763.05	1764.92	1783.07	1792.11
1805.32	1860.42	1884.24					

These lines were carefully chosen by using two criteria. The most important criterion was that the difference between the radial velocity and the mean radial velocity for each line should not exceed 2.5σ in magnitude, where σ is the standard deviation of the radial velocity from its mean for a given spectrum. Using this criterion, we rejected lines with a possible identification error and blended lines. The second criterion involved the line width, which is meant to be the parameter of the Gaussian fit to the line profile; this allows blended lines to be rejected. Since the lines were selected by using stringent criteria, the above list can be used as a reference in investigating the spectra of OB stars from the IUE archive.

The following sources of errors in the radial-velocity measurements should be noted: line blending, inaccurate wavelengths, and photometric errors. The first two errors are systematic in nature and can be eliminated by analyzing the radial-velocity residuals for all spectra. The third type of error is random in nature. Here, allowance for the residuals is meaningless, because in this case, the radial velocity does not change and only the formal error decreases, which is small anyway.

Table 4. A list of interstellar lines

Species	λ, Å	Species	λ, Å	Species	λ, Å	Species	λ, Å
N I	1163.88	S II	1250.58	Si II	1311.26	Si II	1808.00
N I	1164.32	S II	1253.81	Si II	1350.52	Si II	1816.93
Al II	1189.19	S II	1259.52	Si II	1526.71	Al III	1854.72
Si II	1190.42	Si II	1260.42	Si II	1533.45	Al III	1862.79
Si II	1193.29	Si II	1264.74	C I	1560.31		
Si II	1194.50	O I	1302.17	C I	1667.01		
Si II	1197.39	Si II	1304.37	Si II	1608.46		
N I	1199.55	O I	1304.86	Al II	1670.79		
N I	1200.22	O I	1306.03	N I	1745.25		
N I	1200.71	Si II	1309.28	Al II	1765.82		

To make sure that the radial velocity of the star was determined accurately, we measured the radial velocities from interstellar lines. These measurements are presented in Table 3, and the list of lines is given in Table 4. The notation in Table 3 is the same as that in Table 2. The error of the mean g for all spectra is 0.01 Å.

We used the lists from Ferrero (1984) and Holberg *et al.* (1998) to identify interstellar lines. However, the VALD list of lines for a star with $T_{\rm eff} = 20\,000$ K proved to be most useful. This list contains almost all interstellar lines. The absence of lines in the line list for a star with $T_{\rm eff} = 37\,500$ K (Θ^1 Ori C), a low degree of ionization, and a small line width may be considered to be evidence of such lines. For the first two spectra, the radial velocity also served as additional evidence of interstellar lines, because it differs significantly for stellar and interstellar lines. In the remaining cases, the radial-velocity difference is not large enough for this criterion to be used.

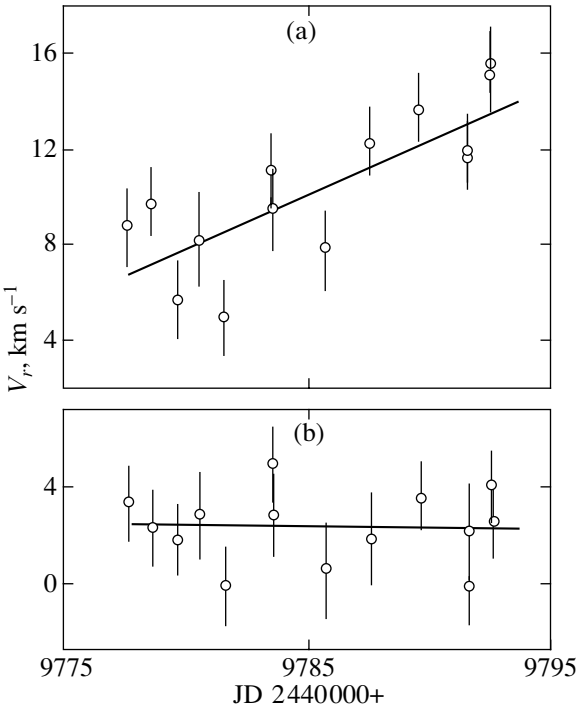

Fig. 1. The time dependence of the radial velocity constructed from (a) stellar and (b) interstellar lines. The errors are indicated by vertical bars; the straight lines were drawn by least squares.

We detected no circumstellar lines.

An examination of Table 2 leads us to the firm conclusion that the radial velocity is variable. Let us compare two measurements from spectra nos. 02768 and 07481. The radial velocities differ by $\Delta V_r = 42.5 - (-2.5) = 45$ km s^{-1}. The errors of the first and second measurements are 2 and 1.6 km s^{-1}, respectively. If we take the larger error as noise, then the signal-to-noise (S/N) ratio will be S/N$= 45/2 = 22.5$. For such an S/N ratio, the variability is beyond question.

Let us perform a simple analysis of the data in Tables 2 and 3. The goal of this analysis is to check whether the radial velocity of the star is constant or variable for the dense series of measurements given in the last 14 rows of Table 2.

The results of our analysis are presented in Fig. 1. Figure 1a shows the measurements with stellar lines. The straight line was drawn by least squares; its equation is

$$V_r = 6.5(\pm5) + 0.46(\pm4)(t - 2\,449\,777). \qquad (2)$$

In Eq. (2), t is the epoch of observation in Julian days. The errors in the coefficients (in the last decimal digit) are given near them. The error of a

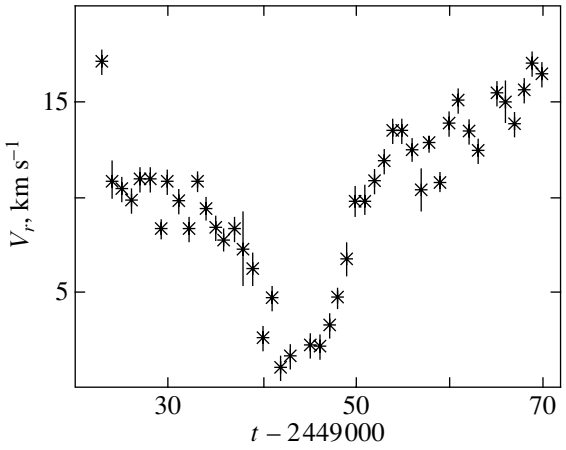

Fig. 2. The radial-velocity measurements by Stahl *et al.* (1993).

single equation is 2.0 km s^{-1}, in agreement with the measurement errors in Table 2.

The second coefficient is the slope of the straight line. It was found to be a factor of 11.5 larger than the error of its determination. This proves that the radial velocity is variable.

In three cases, the measurements were carried out twice during 1 day. We see from Fig. 1a that these pairs of measurements are in close agreement, within the error limits. This suggests that the star exhibits no rapid radial-velocity variations on a time scale of $\sim$1 day.

Figure 1b shows the measurements with interstellar lines. These measurements were fitted by a straight line with the equation

$$V_r = 2.4(\pm5) - 0.01(\pm4)(t - 2\,449\,777). \qquad (3)$$

In this case, the second coefficient is a factor of 4 smaller in magnitude than the error of its determination, suggesting that the radial velocity of interstellar lines is constant. The error of a single equation is 1.5 m s^{-1}, in close agreement with the intrinsic errors in Table 3.

ANALYSIS OF THE OBSERVATIONS BY STAHL *et al.* (1993)

In Fig. 2, the radial-velocity measurements from Stahl *et al.* (1993) are indicated by asterisks. These measurements were taken from the plot, because they were not tabulated. The authors pursued the goal to detect radial-velocity variations with the same period with which the Hα equivalent width varied, i.e., $\sim$ 15 days.

An examination of Fig. 2 and simple estimates lead us to several important conclusions.

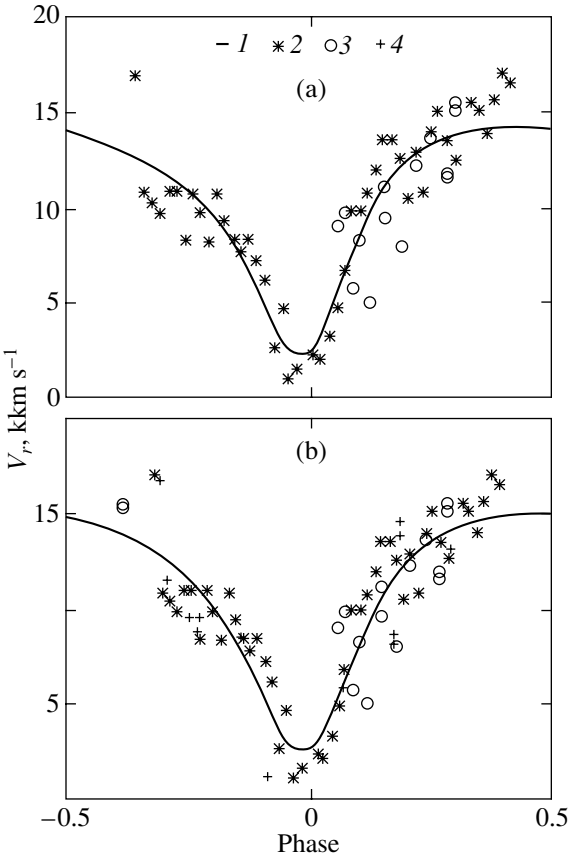

Fig. 3. The radial-velocity observations folded with the periods calculated for $L = 12$ (a) and for $L = 11$ (b): (*1*) theoretical radial-velocity curve; (*2*) the observations by Stahl *et al.* (1993); (*3*) the dense series of observations from the lower part of Table 2; (*4*) observations by Conti.

The period of the radial-velocity variations is considerably larger than the observing interval of 45 days. This obvious conclusion was also reached by Stahl *et al.* (1993). Thus, the radial velocity does not vary with a 15-day period.

The radial-velocity minimum is sharp and comparatively narrow, suggesting that the orbit has a significant eccentricity.

Let us compare the observed radial-velocity curve shown in Fig. 2 with the observations by Struve and Titus (1944), who also provided a dense 44-day-long series of radial-velocity measurements. The mean velocity inferred from these measurements is $\langle V_r \rangle = 37(2)$ km s^{-1}. The observations by Stahl *et al.* (1993) yield $\langle V_r \rangle = 9.8(6)$ km s^{-1}. Clearly, the discrepancy between these values is far beyond the error limits, which once again confirms the radial-velocity variability. If the observations by Struve and Titus (1994) are assumed to refer to the region of the broad radial-velocity maximum, then the radial-velocity amplitude can be roughly estimated: $K = (37 - 10)/2 =$

8 km s^{-1}. This estimate shows that the radial-velocity curve cannot be constructed by the classical technique of radial-velocity measurements, because the measurement errors for this technique lie within the range 16–34 km s^{-1} (Vitrichenko *et al.* 1996). Only observations with an error of $\sim$1 km s^{-1} achieved by Stahl *et al.* (1993) allow a reliable radial-velocity curve to be constructed.

Let us estimate the connectedness of the radial-velocity measurements by Stahl *et al.* (1993). We define this quantity σ_c as

$$\sigma_c = \left[\sum\{(V_i - V_{i+1})/2\}^2/(N-1)\right]^{1/2} \quad (4)$$
$$= 1.0 \text{ km s}^{-1}.$$

Here, V_i and V_{i+1} are two adjacent (in time) radial velocities and N is the number of measurements. The summation is performed from $i = 1$ to $i = N - 1$. The quantity σ_c is useful in determining the convergence of the iteration process. An iteration may be considered complete when $\sigma_m \sim \sigma_c$, where σ_m is the normal rms deviation of the measured radial velocities from the theoretical radial-velocity curve. The quantity σ_c is also useful to know when planning new observations. Its value shows that for an accuracy of radial-velocity measurements equal to $\sim$1 km s^{-1}, the sampling interval of the measurements must be $\sim$1 day.

The above estimates allowed us to specify approximate initial parameters of the radial-velocity curve and to determine the significance of the derived orbital elements.

The theoretical curve was constructed by using the following technique.

Our dense series of 14 measurements (the lower part of Table 2) was displaced along the axis of dates to closely coincide with the observations by Stahl *et al.* (1993). This displacement was 729.6(10) days, which allows the probable periods to be calculated from the formula

$$P = 729.6/L \text{ days}, \quad (5)$$

where L is an integer.

Figure 3a shows the radial-velocity curve for $L = 12$.

The spectroscopic orbital elements calculated by least squares are given in Table 5. Also given here for comparison are the elements for $L = 11$ and for the star V1016 Ori (Vitrichenko *et al.* 1998). The epoch refers to the time when the stars pass through the periastron.

It follows from an examination of Table 5 that the orbital elements for $L = 12$ and $L = 11$ are equal, within the error limits. The errors of a single equation given in the last row are also equal. For these reasons, we cannot favor a particular assumption. Our experience in reducing observations with $L < 12$ shows the agreement between individual series of measurements and the theoretical curve to be appreciably poorer.

A comparison with the elements for V1016 Ori leads us to conclude that the periods, eccentricities, and longitudes of the ascending node are similar for the two stars. This argues for the assumption that the orbital axes are close in direction. In that case, however, an eclipse is possible in Θ^1 Ori C, which we can attempt to detect at the time of conjunction. This time can be easily calculated from the spectroscopic orbital elements if the correct period is found. Conversely, if several probable periods are known, then the detection of an eclipse using the ephemeris will allow the true period to be chosen from several probable periods.

Recall that for our analysis, we chose only the dense series of our measurements from the lower part of Table 2. As we see from Fig. 3a, these measurements are in close agreement with the observations by Stahl *et al.* (1993). The error of a single equation virtually matches the mean error of our measurements (see Table 2). However, a large fraction of the measurements (1/3 of their total number) in the upper part of Table 2 disagree with the theoretical radial-velocity curve. The possible causes of this disagreement are considered below.

Yet another complicated question concerns the systematic errors of the radial velocity. We carried out our measurements by using IUE spectra. These spectra were processed with the old IUESIPS program. According to Holberg *et al.* (1998), the systematic correction between ground-based and IUE radial-velocity measurements is +1.3(1.2) km s^{-1}. This correction was disregarded, because it is small and matches the error of its determination.

ANALYSIS OF THE OBSERVATIONS BY CONTI (1972)

The third (and last) series of dense, highly accurate observations was obtained by Conti (1972). Let us consider the question of whether these observations are consistent with the radial-velocity curve shown in Fig. 3a.

We managed to achieve good agreement of Conti's observations with other observations and with the theoretical radial-velocity curve by applying a systematic correction of -15 km s^{-1} to Conti's observations and by slightly changing the period for $L = 11$. The new period is $P = 729.6/11 - 0.08 = 66.319(4)$ days. The significant increase in accuracy stems from the fact that Conti's observations are separated from the initial epoch by $\sim$800 cycles. Since

Table 5. Spectroscopic orbital elements

Parameter	$L = 12$	$L = 11$	Conti	V1016 Ori
P, days	60.8(1)	66.3(1)	66.319(4)	65.4
γ, km s^{-1}	10.6(2)	10.9(2)	26(1)	28.3(10)
K, km s^{-1}	6.0(4)	6.1(4)	6.2(4)	32.7(15)
ω, rad	−2.87(5)	−2.88(5)	−2.92(5)	3.12(5)
e	0.39(6)	0.43(6)	0.39(6)	0.66(3)
T, JD	2449044.6(4)	2449044.7(4)		2441970.4(2)
$a_1 \sin i$, AU	0.031	0.033	0.035	0.15
f_1, $M_\odot$	0.11×10^{-2}	0.12×10^{-2}	0.13×10^{-2}	0.10(1)
σ, km s^{-1}	1.8	1.8	1.9	10

period miscalculation is highly probable in this case, the accuracy of the period is most likely fictitious.

A new theoretical radial-velocity curve was constructed with the elements given in the next-to-last column of Table 5. As we see from the last row of this table, the error of a single measurement is virtually the same; all the remaining elements are also equal, within the error limits.

Figure 3b shows all three series of accurate observations, along with the two measurements from Table 2 that closely agree with other observations. These two measurements are in conflict with the period for $L = 12$ but agree with all measurements for $L = 11$. A total of 75 radial-velocity measurements are plotted in Fig. 3b.

We may conclude that Conti's dense, highly accurate series of measurements agrees with the probable period for $L = 11$. In this case, Conti's observations almost completely cover the entire period and his suggestion of a constant radial velocity is inconsistent with his own measurements.

The nature of the −15 km s^{-1} correction is not yet clear; it will be discussed below.

ANALYSIS OF THE OBSERVATIONS BY STRUVE AND TITUS (1944)

This series of observations is fairly dense, but it cannot be considered to be highly accurate. The authors provided no observational errors of the radial velocity. We deduced the error of a single measurement, 8 km s^{-1}, from the error of the mean radial velocity. This error is given in the paper, but it characterizes the scatter of this series of observations about the mean.

The error of a single measurement by these authors was previously studied in two papers. Having analyzed the radial-velocity measurements for the star BM Ori, Vitrichenko *et al.* (1996) determined the error of a single measurement (24 km s^{-1}). Vitrichenko *et al.* (1998) used the observations by Struve and Titus (1944) to construct the radial-velocity curve for the star V1016 Ori and found the error of a single measurement to be 11 km s^{-1}. The difference in the measurement accuracy results from the difference between $V \sin i$ for the two stars. For BM Ori and V1016 Ori, $V \sin i = 170$ and 90 km s^{-1}, respectively.

Whereas the above three highly accurate series of measurements have an error of 2 km s^{-1}, the error of the observations by Struve and Titus is severalfold larger. Therefore, it would be unreasonable to expect a high accuracy when constructing and analyzing the radial velocity using these observations.

Figure 4 shows (*1*) a plot of the observations by Struve and Titus (1944) against Julian date and (*2*) a theoretical radial-velocity curve. The theoretical curve was constructed with the following elements: $P = 55(5)$ days, Ep = JD 2430785(2), $g =$

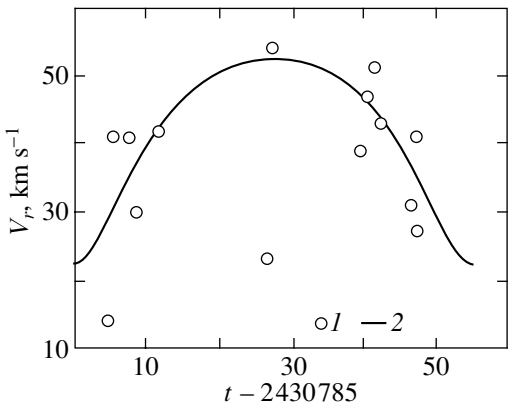

Fig. 4. (*1*) The radial-velocity measurements by Struve and Titus (1944); (*2*) a theoretical radial-velocity curve. The elements of the theoretical curve are given in the text. The Julian dates measured from an arbitrary initial epoch are along the horizontal axis.

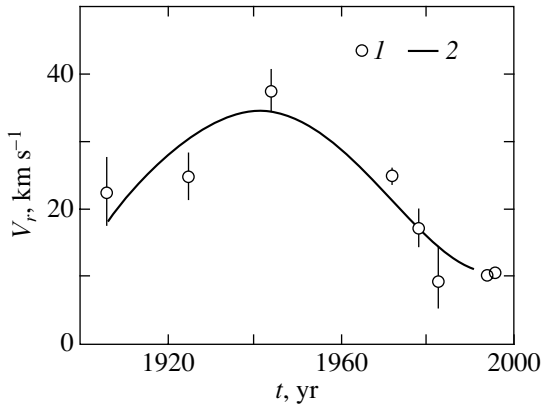

Fig. 5. γ velocity versus time: (*1*) observations, with the errors represented by vertical bars; (*2*) a sine-wave fit to the observations.

42(2) km s^{-1}, $K = 15(2)$ km s^{-1}, $\omega = -3.14$ rad, and $e = 0.3$. The errors are rough estimates.

An examination of Fig. 4 leads us to the following conclusions. Given the above errors, the observations are in satisfactory agreement with the theoretical radial-velocity curve. Even the greatly deviating point $t - 2\,430\,785 = 28$ days is not an outlier for an error of a single measurement equal to 8 km s^{-1} if the 3σ criterion is used.

The epoch was chosen arbitrarily, because the observations are so far away from the previously adopted epoch that period miscalculation is highly probable.

All the remaining elements are in satisfactory agreement with those obtained from the highly accurate observations.

The γ velocity constitutes an exception. It exceeds the previously obtained values so much that this circumstance forces us to cease the study of individual series of measurements and to consider the pattern of variations in the γ velocity with time, especially since a preliminary analysis showed that the remaining series of measurements have an insufficient accuracy for this type of analysis, which was performed by using highly accurate observations. In addition, their sampling interval is unsatisfactorily large.

THE HYPOTHESIS OF A THIRD STAR

To analyze the behavior of the γ velocity with time, we use the mean radial velocities of all series of measurements, which we take as the γ velocity. In this case, we admit an error but it cannot be large, because K is relatively small for companion C1.

In Table 1, the mean radial velocity and its error are given for each series of observations in the last two columns. Figure 5 shows a plot of the γ velocity against time. Dates (in years) are along the horizontal axes. The errors are indicated by bars. The observed dependence was fitted with a sine wave. We obtained the following orbital elements by least squares:

$$\gamma = 22(1) \text{ km s}^{-1}, \quad K = 13(2) \text{ km s}^{-1}, \quad (6)$$
$$\text{Ep} = 1911(3) \text{ yr}, \quad P = 120(6) \text{ yr},$$
$$e = 0 \text{ (fixed)}.$$

The time of conjunction on the ascending branch of the radial-velocity curve was taken as the initial epoch.

An examination of Fig. 5 leads us to conclude that the observations are in satisfactory agreement with the theoretical curve. Consequently, there is a second companion in the system and the system itself is at least a triple one.

In this case, $\gamma = 22(1)$ km s^{-1} is the center-of-mass radial velocity for the triple system.

The hypothesis that the radial-velocity variations we detected could result from the motion of the stellar atmosphere must be rejected. Simple calculations show that if the star pulsates, then its brightness must vary significantly, which is not observed.

DISCUSSION

Below, we discuss the following questions: (1) why only $\sim 2/3$ of the new observations satisfy the radial-velocity curve; (2) how to organize further observations of the star to confirm or reject our hypothesis of two companions; (3) whether star C_2 discovered by Weigelt *et al.* (1999) can be companion C2; and (4) whether the primary star can be eclipsed by companion C1.

We managed to reconcile only $\sim 2/3$ of the new observations (the lower part of Table 2) with the radial-velocity observations by Stahl *et al.* (1993). These observations form a dense series. The remaining observations (the upper part of Table 2) are comparatively far away from the initial epoch and form small groups widely spaced in time. Since both periods of the radial-velocity variations are known with insufficient accuracy, all observations are difficult to reconcile. The problem can be solved if the two periods are refined.

The question of accuracy is a key question where the new observations are concerned. Whereas classical radial-velocity measurements for O stars give an order-of-magnitude error of ~ 10 km s^{-1}, an accuracy of ~ 1 km s^{-1} is required to analyze the star under consideration. The next important question concerns the sampling interval of the measurements and their duration. To reliably construct the radial-velocity curve for a period of 60–66 days, we must measure the radial velocity at least once in two days

and continue the observations for no fewer than 70–80 nights. Note that none of the authors has obtained a complete radial-velocity curve for the short period.

To confirm the long period (~120 yr), we must construct the radial-velocity curve for the short period every five or six years and use the γ velocity to construct the radial-velocity curve for the long period. We managed to construct the radial-velocity curve only for a time interval spanning ~3/4 of the period. Further observations will allow us to estimate the orbital eccentricity and to improve the orbital elements.

Let us consider the question of whether star C_2 discovered by Weigelt *et al.* (1999) can be the same star C2 that we discovered. According to these authors, the separation between the primary star and companion C_2 is 16 AU in a plane perpendicular to the line of sight. Because of the projection effect, the true separation between the stars at the epoch of observation can only be larger than this value. We derive the following inequality for the radius of the relative orbit:

$$a > 16 \text{ AU}. \quad (7)$$

By solving the radial-velocity curve, we can derive yet another inequality for a:

$$a > KP(1 + 1/q)/2\pi = 200 \text{ AU}. \quad (8)$$

In this formula, $K = 13$ km s^{-1} is the velocity at which the primary star moves around the center of mass due to the presence of a second companion, $P = 120$ yr is the period of this motion, and $q = M_2/M_1 = 6/20 = 0.3$ is the mass ratio of the companion and the primary star. The masses were taken from Weigelt *et al.* (1999) and Vitrichenko (2000). The inequality sign appears here, because we assumed that $\sin i = 1$.

To estimate a, we can also make use of the Kepler law

$$a = [P^2(M_1 + M_2)]^{1/3} = 100 \text{ AU}. \quad (9)$$

Inequality (7) is consistent with inequality (8) and equality (9), but formally, inequality (8) is in conflict with equality (9). However, given that the masses were inferred from evolutionary tracks and hence are inaccurate and that there are no data on $\sin i$, the above estimates for the radius of the relative orbit may be considered to be in satisfactory agreement. It should then be concluded that star C_2 discovered by Weigelt *et al.* (1999) and star C2 we discovered could be the same star.

If this is the case, then a unique opportunity to determine the distance to the system and the components' masses opens up. This requires investigating the orbit of companion C2 as a visual double star. An extended period is needed for the problem to be solved, but it is solvable.

The data obtained are insufficient to conclude whether an eclipse is possible in the system. Below, we provide evidence for this possibility. Two of the four Orion Trapezium stars are eclipsing systems. If all stars were formed from a common protostellar aggregate whose rotation plane was close to the line of sight, then it would be natural to expect a similar orientation of the orbital plane for the star under study.

Let us roughly estimate the separation between the primary star and companion C1 using the Kepler law

$$a = (M_1 P^2)^{1/3} = 0.9 \text{ AU}. \quad (10)$$

Equality (10) gives the semimajor axis of a relative elliptical orbit, but for the subsequent estimates, we may assume a to be the radius of a circular orbit. Here, $M_1 = 20M_\odot$ is the mass of the primary star (Vitrichenko 2000), the mass of companion C1 is ignored, and P is the orbital period of the companion (in years).

We write the condition for the existence of an eclipse as

$$57.3(R + R_1)/a > 90^\circ - i, \quad (11)$$

$$4\overset{\circ}{.}8 > 3\overset{\circ}{.}9. \quad (11a)$$

In inequality (11), $R = 7.4R_\odot$ is the radius of the primary star taken from the tables of Straizis and Kuriliene (1981) for a zero-age main-sequence O6 star, $R_1 = 8.4R_\odot$ is the radius of the companion of BM Ori (Vitrichenko *et al.* 1996), $a = 190R_\odot$ is the orbital semimajor axis given by expression (10), and $i = 86\overset{\circ}{.}1$ is the mean orbital inclination for BM Ori and V1016 Ori (Bondar' and Vitrichenko 1995; Bondar' *et al.* 2000). The first factor serves to convert radians to degrees.

Formula (11a) gives the left- and right-hand parts of the inequality. A comparison of these values leads us to conclude that an eclipse is quite possible, but it should be borne in mind that we consider an optimistic case.

A close examination of Fig. 3b reveals an interesting feature: near phase 0.7 (phase −0.3 in Fig. 3b), four observations show an increase in the radial velocity relative to the theoretical curve, following which the group of observations lies below the theoretical radial-velocity curve. Such a phenomenon is well known. It is attributed to an eclipse of the star and can be explained by the fact that part of the rotating star is eclipsed by the companion, which distorts the measured radial velocity. This fact is strong evidence for an eclipse.

However, there is a peculiarity that is still difficult to explain. Because of the orbital ellipticity, the conjunction of the stars occurs at phase 0.84 and an abrupt change in the radial velocity must be observed

precisely at this phase, whereas it is observed near phase 0.7. The plausible explanations are that either the period is inaccurate, the orbit is inaccurate, or an eclipse is produced not by companion C1 but by a different body revolving with a multiple period. The choice between these alternatives cannot yet be made.

Table 5 gives the epochs of periastron passage by the stars. The conjunction (primary minimum) for the two periods ($L = 11, 12$) occurs at phase 0.842. For $L = 11$, the ephemeris for the observed primary minimum can be calculated from the elements

$$\min \mathrm{I} = \mathrm{JD}\ 2449034.2(4) + 66.3(1)E. \qquad (12)$$

It is easy to calculate the elements for $L = 12$ as well, because the minimum occurs at the same phase. Since, as we see from formula (12), the error in the precomputed epoch of minimum is large, observations must be carried out for several days near the computed epoch.

CONCLUSIONS

Our analysis of all the available radial-velocity measurements for Θ^1 Ori C suggests the existence of two companions, which we propose to designate as Θ^1 Ori C1 and Θ^1 Ori C2.

The probable orbital period of companion C1 can be calculated using the formula $P = 729.6/L$ days, where $L < 13$ is an integer. At $L = 11$, the measurements by Stahl *et al.* (1993) and Conti (1972) and more than half of the new radial-velocity measurements can be reconciled with its theoretical radial-velocity curve. The remaining new measurements are far away from the initial epoch in time. As a result, the following errors are introduced: due to the inaccurate period, because of the systematic variation in γ velocity, and due to period miscalculation. The evolution of orbital elements, for example, apsidal rotation, is also possible in a triple system.

Our analysis of the temporal behavior of the γ velocity for companion C1 suggests the existence of yet another companion C2. We provide evidence that companion C2 is star C_2 discovered by Weigelt *et al.* (1999) through speckle interferometry.

ACKNOWLEDGMENTS

I am grateful to the Vienna Atomic Line Data Center (Kupka *et al.* 1999) for providing a list of spectral lines and to the IUE archive (Folker 1984) for organizing friendly access to the archive. The discussions with V.E. Vitrichenko, O.B. Kostina, L.I. Matveyenko, and V.P. Fedotov were very helpful.

REFERENCES

1. H. A. Abt, R. Wang, and O. Cardona, Astrophys. J. **367**, 155 (1991).
2. J. Babel and Th. Montmerle, Astrophys. J. Lett. **485**, L29 (1997).
3. N. I. Bondar' and E. A. Vitrichenko, Pis'ma Astron. Zh. **21**, 708 (1995) [Astron. Lett. **21**, 627 (1995)].
4. N. I. Bondar', E. A. Vitrichenko, and M. M. Zakirov, Pis'ma Astron. Zh. **26**, 525 (2000) [Astron. Lett. **26**, 452 (2000)].
5. P. S. Conti, Astrophys. J. Lett. **174**, L79 (1972).
6. R. F. Ferrero, in *Proceedings of the Fourth International Ultraviolet Explorer Conference, Rome, 1984* (ESA, Paris, 1984), ESA SP-218, p. 133.
7. J. Folker, in *Proceedings of the Fourth International Ultraviolet Explorer Conference, Rome, 1984* (ESA, Paris, 1984), ESA SP-218, p. 465.
8. E. B. Frost, S. B. Barrett, and O. Struve, Astrophys. J. **64**, 1 (1926).
9. M. Gagne, J.-P. Cailault, J. R. Stauffer, and J. J. Linski, Astrophys. J. Lett. **478**, L87 (1997).
10. J. B. Holberg, M. A. Barstow, and E. M. Sion, Astrophys. J., Suppl. Ser. **119**, 207 (1998).
11. B. V. Kukarkin, P. N. Kholopov, N. M. Artyukhina, *et al.*, *New Catalogue of Stars Suspected to Brightness Variability* (Nauka, Moscow, 1982).
12. F. Kupka, N. E. Piskunov, T. A. Ryabchikova, *et al.*, Astron. Astrophys., Suppl. Ser. **138**, 119 (1999).
13. N. Morrell and H. Levato, Astrophys. J., Suppl. Ser. **75**, 965 (1991).
14. O. Stahl, Th. Gang, C. A. Gummersbach, *et al.*, Astron. Astrophys. **274**, L29 (1993).
15. O. Stahl, A. Kaufer, Th. Rivinius, *et al.*, Astron. Astrophys. **312**, 530 (1996).
16. V. Straizis and G. Kuriliene, Astrophys. Space Sci. **89**, 353 (1981).
17. O. Struve and J. Titus, Astrophys. J. **99**, 84 (1944).
18. É. A. Vitrichenko, Pis'ma Astron. Zh. **26**, 294 (2000) [Astron. Lett. **26**, 244 (2000)].
19. É. A. Vitrichenko, V. S. Shevchenko, and V. A. Shcherbakov, Pis'ma Astron. Zh. **22**, 185 (1996) [Astron. Lett. **22**, 163 (1996)].
20. É. A. Vitrichenko, V. G. Klochkova, and S. I. Plachinda, Pis'ma Astron. Zh. **24**, 352 (1998) [Astron. Lett. **24**, 295 (1998)].
21. N. R. Walborn, Astrophys. J. Lett. **243**, L37 (1981).
22. N. R. Walborn and J. S. Nichols, Astrophys. J. Lett. **425**, L29 (1994).
23. G. Weigelt, Y. Balega, T. Preibisch, *et al.*, Astron. Astrophys. **347**, 15 (1999).

Translated by V. Astakhov

Astronomy Letters, Vol. 28, No. 5, 2002, pp. 335–344. Translated from Pis'ma v Astronomicheskiĭ Zhurnal, Vol. 28, No. 5, 2002, pp. 382–392.

Parametric Generation of Acoustic-Gravity Waves by Alfvén Waves in the Solar Atmosphere

M. Yu. Petukhov* and Yu. V. Petukhov

Institute of Applied Physics, Russian Academy of Sciences, ul. Ul'yanova 46, Nizhni Novgorod, 603600 Russia

Received October 3, 2001

Abstract—Based on a plane-parallel isothermal model solar atmosphere permeated by a uniform magnetic field directed against the action of gravity, we investigate the parametric generation of acoustic-gravity disturbances by Alfvén waves propagating along the corresponding field lines. We established that for a weak linear coupling of Alfvén waves, the nonlinear interaction of Alfvén waves propagating in opposite directions (rather than in the same direction) is the predominant generation mechanism of acoustic-gravity disturbances at the difference frequency. In this case, no acoustic flow (wind) was found to emerge at a zero difference frequency in the acoustic-gravity field. © *2002 MAIK "Nauka/Interperiodica".*

Key words: *Sun, atmosphere, waves*

INTRODUCTION

When studying the oscillation and wave processes in the solar atmosphere, several fundamental problems have been formulated to date (Dubov 1978; Vorontsov and Zharkov 1988; Severnyi 1988; Priest 1982; *Advances in Solar System Magnetohydrodynamics* 1991; Kaplan *et al.* 1977). The following two interrelated questions feature prominently among these problems: whether vertically propagating acoustic-gravity waves (AGWs) at frequencies below the Lamb cutoff frequency ω_L can exist up to coronal heights (Dubov 1978; Vorontsov and Zharkov 1988; Severnyi 1988; Petukhov and Petukhov 2001) and how efficient the nonlinear absorption of Alfvén waves is, which can thus contribute to coronal heating and solar-wind acceleration (Priest 1982; *Advances in Solar System Magnetohydrodynamics* 1991; Kaplan *et al.* 1977). The corresponding problems are interrelated for the following reasons. First, the propagating AGWs at frequencies $\Omega_- = \omega_2 - \omega_1 < \omega_L$ can be generated through the nonlinear interaction of not only waves of similar types with different frequencies ω_1 and ω_2 (Petukhov and Petukhov 2001), but also of Alfvén waves. Second, the nonlinear absorption of Alfvén waves can show up through their transformation into AGWs not only at relatively low Ω_-, but also at high $\Omega_+ = \omega_1 + \omega_2$ frequencies, to which the relatively large and small dissipation heights of the latter correspond.

That is why our goal here is to investigate the parametric generation of AGWs by vertically propagating Alfvén waves in terms of a simple plane-parallel isothermal model solar atmosphere with a uniform magnetic field directed against the action of gravity.

It should be noted that the linear propagation of Alfvén waves and AGWs was considered in detail in terms of this model solar atmosphere by Ferraro and Plumpton (1958), Nakagawa *et al.* (1973), Brengauz (1969, 1974), Hollweg (1979, 1981), Christensen-Dalsgaard and Hasan (1992), and Banarjee *et al.* (1995). In addition, the nonlinear transformation of such waves was investigated analytically (Uchida and Kabuaki 1974; Wentzel 1974; Chiu 1971; Cohen and Kulsrud 1974; Low 1982) and numerically (Frank *et al.* 1995; Galloway *et al.* 1982; Hollweg 1982; Kudoh and Shibata 1999; Herbold *et al.* 1985; Hollweg and Sterling 1988). However, no consistent analysis of the problems formulated above has been performed in terms of the hydrodynamic approach, which to a greater extent refers to approximate analytical studies (Uchida and Kabuaki 1974; Wentzel 1974). Bridging this gap in the studies of the nonlinear transformation of Alfvén waves is also a distinctive feature of our work.

FORMULATION OF THE PROBLEM. THE DERIVATION OF APPROXIMATE NONLINEAR EQUATIONS

Let us consider the vertical propagation of plane magnetohydrodynamic (MHD) waves in a plane-parallel isothermal atmosphere $z \geq 0$ permeated by

*E-mail: petukhov@hydro.appl.sci-nnov.ru

a uniform magnetic field directed along the z axis. Such an atmosphere is characterized by certain dependences of the equilibrium pressure $p_0(z)$ and density $\rho_0(z)$ of a perfect gas on height z:

$$p_0(z) = \frac{\rho_{00}c_0^2}{\gamma}\exp(-z/H), \quad (1)$$
$$\rho_0(z) = \rho_{00}\exp(-z/H),$$

and by constant values of the vertical component B_0 of the magnetic induction vector $\mathbf{B}_0 = (0, 0, B_0)$, adiabatic speed of sound c_0, adiabatic index γ, Lamb frequency ω_L, and scale height H (Dubov 1978; Vorontsov and Zharkov 1988; Severnyi 1988; Priest 1982; *Advances in Solar System Magnetohydrodynamics* 1991):

$$c_0^2 = \gamma p_0/\rho_0, \quad \omega_L = \gamma g/2c_0, \quad H = c_0/2\omega_L. \quad (2)$$

Here, the z axis is assumed to be directed vertically upward, against the action of gravity, whose free-fall acceleration is constant and equal to g; $\rho_{00} = \rho_0(z = 0)$ is the gas density at the lower atmospheric boundary.

We also assume that the atmosphere borders an absolutely rigid half-space with periodic magnetic-field disturbances observed over its entire depth, $z \le 0$. These disturbances produce steady-state (in time t) perturbations of the horizontal (along the x axis) oscillation velocity in the atmosphere at $z = 0$ at frequencies ω_1 and ω_2 with the corresponding amplitudes A_1 and A_2:

$$v_x|_{z=0} = A_1\cos(\omega_1 t) + A_2\cos(\omega_2 t), \quad (3)$$
$$(-\infty < t < +\infty),$$
$$v_z|_{z=0} = 0.$$

As was pointed out in the Introduction, below, we focus on an approximate analytic description of the nonlinear parametric generation of AGWs by Alfvén waves at the difference Ω_- $\begin{cases} < \omega_L \\ > \omega_L, \end{cases}$ and sum Ω_+ $\begin{cases} < \omega_L \\ > \omega_L, \end{cases}$ frequencies.

To solve the formulated problem, we use the system of MHD equations that describes the motion of a perfectly conducting, compressible gas in a gravitational field (Priest 1982; *Advances in Solar System Magnetohydrodynamics* 1991):

$$\begin{cases} \rho\left\{\dfrac{\partial \mathbf{v}}{\partial t} + (\mathbf{v}\boldsymbol{\nabla})\mathbf{v}\right\} & (4) \\ \quad = -\boldsymbol{\nabla}\left(p + \dfrac{\mathbf{B}^2}{2\mu_0}\right) + \dfrac{(\mathbf{B}\boldsymbol{\nabla})\mathbf{B}}{\mu_0} + \rho\mathbf{g}, \\ \dfrac{\partial \rho}{\partial t} + \boldsymbol{\nabla}(\rho\mathbf{v}) = 0, & (5) \\ \dfrac{\partial p}{\partial t} + (\mathbf{v}\boldsymbol{\nabla})p = \dfrac{\gamma p}{\rho}\left\{\dfrac{\partial \rho}{\partial t} + (\mathbf{v}\boldsymbol{\nabla})\rho\right\}, & (6) \\ \dfrac{\partial \mathbf{B}}{\partial t} = [\boldsymbol{\nabla} \times [\mathbf{v} \times \mathbf{B}]], & (7) \\ (\boldsymbol{\nabla}\mathbf{B}) = 0. & (8) \end{cases}$$

Here, $p = p_0 + p'$ is the total pressure, $\rho = \rho_0 + \rho'$ is the total density, and $\mathbf{B} = \mathbf{B}_0 + \mathbf{B}'$ is the total magnetic induction vector; p', ρ', and $\mathbf{B}'$ are the pressure, density, and magnetic induction vector perturbations, respectively; $\mathbf{v} = (v_x, 0, v_z)$ is the oscillation velocity vector with horizontal and vertical components; μ_0 is the magnetic constant, which in our case is assumed to be equal to that for the solar atmospheric plasma. For the subsequent analysis, it should be noted that the perpendicularity of vector $\mathbf{B}'$ to the direction of wave propagation, i.e., $\mathbf{B}' \perp \mathbf{B}_0$, follows from Eq. (8) for a solenoidal magnetic field. This perpendicularity implies that the magnetic induction vector perturbation has only one nonzero horizontal $\mathbf{B}' = (B', 0, 0)$ component.

Thus, we derive the following nonlinear equations for the vertical and horizontal oscillation velocities from Eqs. (4)–(7), to within terms of the second order of smallness in the perturbations of the corresponding quantities $p'/p_0 \ll 1$, $\rho'/\rho_0 \ll 1$, $B'/B_0 \ll 1$, $v_x/c_0 \ll 1$, and $v_z/c_0 \ll 1$:

$$\frac{\partial^2 v_z}{\partial t^2} - c_0^2\frac{\partial^2 v_z}{\partial z^2} + \frac{c_0^2}{H}\frac{\partial v_z}{\partial z} = \frac{\gamma}{\rho_0}\frac{\partial}{\partial z}\left(p'\frac{\partial v_z}{\partial z}\right) \quad (9)$$
$$- \frac{\rho'}{\rho_0}\frac{\partial^2 v_z}{\partial t^2} - 2v_z\frac{\partial^2 v_z}{\partial z\partial t} - \frac{\partial v_z}{\partial t}\frac{\partial v_z}{\partial z} - \frac{1}{2}\frac{c_A^2}{B_0^2}\frac{\partial^2 (B')^2}{\partial z\partial t},$$

$$\frac{\partial^2 v_x}{\partial t^2} - c_A^2\frac{\partial^2 v_x}{\partial z^2} = -\frac{c_A^2}{B_0^2}\frac{\partial^2}{\partial z^2}(B'v_z) \quad (10)$$
$$- \frac{1}{\rho_0}\frac{\partial \rho'}{\partial t}\frac{\partial v_x}{\partial t} - \frac{\rho'}{\rho_0}\frac{\partial^2 v_x}{\partial t^2} - \frac{\partial v_z}{\partial t}\frac{\partial v_x}{\partial z} - v_z\frac{\partial^2 v_x}{\partial z\partial t}.$$

On the right-hand sides of Eqs. (9) and (10), the pressure, density, and magnetic-field perturbations are related, respectively, to the vertical and horizontal oscillation velocities by linear differential equations:

$$\frac{\partial p'}{\partial t} = \rho_0 c_0^2\left(\frac{v_z}{\gamma H} - \frac{\partial v_z}{\partial z}\right), \quad (11)$$

$$\frac{\partial \rho'}{\partial t} = \rho_0\left(\frac{v_z}{H} - \frac{\partial v_z}{\partial z}\right), \quad (12)$$

$$\frac{\partial B'}{\partial t} = B_0 \frac{\partial v_x}{\partial z}. \quad (13)$$

In addition, the following quantity was introduced in Eqs. (9) and (10):

$$c_A = B_0/\sqrt{\mu_0 \rho_0}, \quad (14)$$

which corresponds to the Alfvén wave velocity; in contrast to c_0, it depends on the vertical coordinate.

THE NONLINEAR GENERATION OF AGWs AT THE DIFFERENCE FREQUENCY

To analyze Eqs. (9) and (10) with boundary condition (3), we use the method of successive approximations to within quantities of the second order of smallness for these equations (Petukhov and Petukhov 2001; Rudenko and Soluyan 1975):

$$\mathbf{v} = \mathbf{v}^{(1)} + \mathbf{v}^{(2)}, \quad p' = p^{(1)} + p^{(2)}, \quad (15)$$
$$\rho' = \rho^{(1)} + \rho^{(2)}, \quad B' = B^{(1)} + B^{(2)}.$$

Here, $\mathbf{v}^{(1)}, p^{(1)}, \rho^{(1)}, B^{(1)}$ and $\mathbf{v}^{(2)}, p^{(2)}, \rho^{(2)}, B^{(2)}$ are quantities of the first and second orders of smallness, respectively.

To a first approximation, we derive the following linear equations from Eqs. (9) and (10) using (15):

$$\hat{L} v_z^{(1)} = 0, \quad (16)$$

$$\frac{\partial^2 v_x^{(1)}}{\partial t^2} - c_A^2 \frac{\partial^2 v_x^{(1)}}{\partial z^2} = 0, \quad (17)$$

where we introduce the following operator to make the ensuing equations more compact:

$$\hat{L} = \frac{\partial^2}{\partial t^2} - c_0^2 \frac{\partial^2}{\partial z^2} + \frac{c_0^2}{H}\frac{\partial}{\partial z}. \quad (18)$$

Since $c_0 = \text{const}$, only one term that describes only the AGWs propagating vertically upward at each frequency exceeding the cutoff frequency ω_L should be retained in the general solution of Eq. (16), which is the sum of two particular solutions. Therefore, when there are no corresponding excitation sources of these waves [see (3)], apart from the boundary condition $v_z^{(1)}\big|_{z=0} = 0$, we must require the satisfaction of the equality $p^{(1)}\big|_{z=0} = 0$, from which the second boundary condition $\left.\frac{\partial v_z^{(1)}}{\partial z}\right|_{z=0} = 0$ follows automatically. The latter implies that, to a first approximation, magnetic-field oscillations do not excite AGWs in an isothermal atmosphere:

$$v_z^{(1)} = 0, \quad p^{(1)} = 0, \quad \rho^{(1)} = 0 \quad (z \geq 0). \quad (19)$$

It is quite natural that, to a first approximation, boundary condition (3) implies the linear generation of only Alfvén waves. The corresponding solution of Eq. (17) can be written using the results of many studies (Ferraro and Plumpton 1958; Nakagawa 1973; Brengauz 1969, 1974; Hollweg 1979, 1981; Christensen-Dalsgaard and Hasan 1992; Banarjee 1995; Uchida and Kabuaki 1974; Wentzel 1974; Chiu 1971) as

$$v_x^{(1)} = \mathrm{Re}\left\{\sum_{j=1}^{2} A_j e^{i\omega_j t} \frac{J_0\left(b_j e^{-\frac{z}{2H}}\right)}{J_0(b_j)}\right\}, \quad (20)$$

in which

$$b_j = \beta\frac{\omega_j}{\omega_L}, \quad \beta = \frac{c_0}{c_{A0}}, \quad (21)$$

and $c_{A0} = c_A(z=0)$ corresponds to the Alfvén wave velocity at the $z = 0$ boundary.

With the aim of subsequently using solution (20), let us analyze its behavior at $z > 0$. As we see from (20), the presence of a zero-order Bessel function in the denominators of the corresponding terms enables the resonant excitation of Alfvén waves at certain frequencies

$$\omega_j = \bar{\omega}_n = \omega_L \frac{\bar{b}_n}{\beta}, \quad (j = [1,2], n = 1,2,\ldots), \quad (22)$$

to which the zeros of these functions correspond at $b_j = \bar{b}_n$:

$$J_0(\bar{b}_n) = 0. \quad (23)$$

As can be easily verified (see Abramowitz and Stegun 1964), to the first decimal place, the roots of Eq. (23) are given by the relation

$$\bar{b}_n \approx \beta_n, \quad (24)$$

in which

$$\beta_n = \frac{3}{4}\pi + \pi(n-1). \quad (25)$$

Expressions (22), (24), and (25) allow an accurate determination of the resonance frequencies (particularly for $n \gg 1$). Their appearance, like the emergence of characteristic critical frequencies for modes in waveguides with perfectly reflecting boundaries, is apparently attributable to the formation of the corresponding standing waves at $\omega_j = \bar{\omega}_n$ through the interference of upward- and downward-propagating waves under the specified boundary conditions (3).

The fact that solution (20) for $b_j \gg 1$ ($b_j \geq \bar{b}_1$) describes the superposition of upward- and downward-propagating Alfvén waves can be clearly proven for the atmospheric heights that satisfy the condition

$$b_j e^{-\frac{z}{2H}} \gg 1. \quad (26)$$

Indeed, using the asymptotics of the Bessel function for large values of its argument, we represent solution (20) in the approximate form

$$v_x^{(1)} \approx \mathrm{Re}\left\{\sum_{j=1}^{2}\frac{A_j e^{\frac{z}{4H}}}{\cos(b_j-\pi/4)}e^{i\omega_j t}\cos\left(b_j e^{-\frac{z}{2H}}-\frac{\pi}{4}\right)\right\}. \quad (27)$$

If we also restrict our analysis to sufficiently small heights $z/H \ll 1$ and use the expansion in terms of this small parameter in the argument of the cosine function [see (27)], then by representing the latter as the sum of two corresponding exponents, we can reduce expression (27) to

$$v_x^{(1)} \approx \sum_{j=1}^{2}\frac{A_j e^{\frac{z}{4H}}}{2\cos(b_j-\pi/4)} \times\left\{\cos\left(\omega_j t-\frac{b_j}{2H}z+b_j-\frac{\pi}{4}\right)+\cos\left(\omega_j t+\frac{b_j}{2H}z-b_j+\frac{\pi}{4}\right)\right\}. \quad (28)$$

Clearly, the first and second terms in the curly braces of expression (28) correspond to upward- and downward-traveling Alfvén waves, respectively.

It should be noted that solution (20) can be represented as the sum of two terms corresponding to upward- and downward-propagating Alfvén waves for $b_j \gg 1$ only in a certain range of heights $0 \le z \le z_\mathrm{H}$ in which their interference leads to the natural oscillation of the total field (20) in z. Since the oscillations of the zero-order Bessel function cease with decreasing argument after the passage through the first zero, the upper limit z_H of the corresponding region can be determined from the simple relation

$$b_j e^{-\frac{z_H}{2H}} = \bar{b}_1, \quad (29)$$

which yields

$$z_H = 2H\ln\frac{b_j}{\bar{b}_1}. \quad (30)$$

As we see from (30), the height range $0 \le z \le z_\mathrm{H}$ under consideration appreciably narrows with decreasing radiation frequency, which is attributable to an increase in the importance of Alfvén-wave reflection effects and thus to an enhancement of their linear interaction (coupling) in an isothermal solar atmosphere. The effects of such a strong linear interaction between upward- and downward-traveling Alfvén waves manifest themselves in the fact that the corresponding terms in solution (20) cannot be explicitly separated out when the following condition opposite to (26) is satisfied:

$$b_j e^{-\frac{z}{2H}} \ll 1. \quad (31)$$

Therefore, a kind of oscillation process is established at heights $z \gg z_\mathrm{H}$, which is described by an approximate dependence of a different form following from expressions (20) and (31):

$$v_x^{(1)} \approx \sum_{j=1}^{2}\frac{A_j}{J_0(b_j)}\left(1-\frac{1}{4}b_j^2 e^{-\frac{z}{H}}\right)\cos\omega_j t. \quad (32)$$

Taking into account what we said above regarding the behavior of $v_z^{(1)}$ and $v_x^{(1)}$, let us now turn directly to an analysis of the parametric generation of AGWs. To this end, we derive the following linear inhomogeneous equation for $v_z^{(2)}$ from Eq. (9) using (15) and (19):

$$\hat{L}v_z^{(2)} = -\frac{c_\mathrm{A}^2}{2B_0^2}\frac{\partial^2\left(B^{(1)}\right)^2}{\partial z\partial t}. \quad (33)$$

If we use relation (13) and solution (20), then Eq. (33), after separating out the term on its right-hand side responsible for AGW generation at the difference frequency, reduces to the approximate form

$$\hat{L}v_z^{(2)} \simeq -A_{12}\sin(\Omega_- t)e^{-\frac{z}{2H}} \times\left\{b_1 J_0\left(b_1 e^{-\frac{z}{2H}}\right)J_1\left(b_2 e^{-\frac{z}{2H}}\right)+b_2 J_0\left(b_2 e^{-\frac{z}{2H}}\right)J_1\left(b_1 e^{-\frac{z}{2H}}\right)\right\}, \quad (34)$$

in which

$$A_{12} = \frac{A_1 A_2 B_0^2 b_1 b_2 \Omega_-}{16\omega_1\omega_2\mu_0\rho_{00}H^3 J_0(b_1)J_0(b_2)}. \quad (35)$$

To obtain approximate analytic solutions of Eq. (34), let us consider two limiting situations. Let us first study the parametric generation of waves at the radiation frequencies and heights that satisfy condition (26). The situation corresponding to (26) is of greatest interest, because $v_x^{(1)}$ changes most dramatically with height precisely in the characteristic height range $0 \le z \le z_\mathrm{H}$ (30) where the upward- and downward-traveling Alfvén waves $v_x^{(1)}$ are separated explicitly [see (28)]. Since the magnetic-field perturbation $B^{(1)}$ depends on the rate of change in $v_x^{(1)}$ [see (13)], one might expect the right-hand side of Eq. (34) to be at a maximum when condition (26) is satisfied. Taking into account the smallness of the ratio $z/H \ll 1$, we reduce Eq. (34) to a much simpler form:

$$\hat{L}v_z^{(2)} = \bar{A}_{12}\sin(\Omega_- t) \quad (36)$$

$$\times \{\Omega_+ \cos(\varphi_1 - k_1 z) + \Omega_- \sin(\varphi_2 - k_2 z)\},$$

where

$$\bar{A}_{12} = \frac{A_1 A_2 \beta}{8H} \frac{\Omega_-}{\omega_L \cos\left(b_1 - \frac{\pi}{4}\right) \cos\left(b_2 - \frac{\pi}{4}\right)}, \quad (37)$$

$$k_1 = (b_1 + b_2)/2H = \frac{\beta}{2H}\frac{\Omega_+}{\omega_L}, \quad (38)$$

$$k_2 = (b_2 - b_1)/2H = \frac{\beta}{2H}\frac{\Omega_-}{\omega_L},$$

$$\varphi_1 = b_1 + b_2 = \beta\frac{\Omega_+}{\omega_L}, \quad (39)$$

$$\varphi_2 = b_2 - b_1 = \beta\frac{\Omega_-}{\omega_L}.$$

The general solution of Eq. (36) is the sum

$$v_z^{(2)} = v_{z,H}^{(-)} + v_{z,0}^{(-)} \quad (40)$$

of the particular solution $v_{z,H}^{(-)}$ to the inhomogeneous equation (36) and the solution $v_{z,0}^{(-)}$ to the corresponding homogeneous equation, which are

$$v_{z,H}^{(-)} = \mathrm{Im}\left\{B_1 e^{i(\Omega_- t - k_1 z)} + B_1^* e^{i(\Omega_- t + k_1 z)} + B_2 e^{i(\Omega_- t - k_2 z)} + B_2^* e^{i(\Omega_- t + k_2 z)}\right\}, \quad (41)$$

$$v_{z,0}^{(-)} = \begin{cases} \mathrm{Im}\left\{C_1 \exp\left[\frac{z}{2H} + i\left(\Omega_- t - \sqrt{\frac{\Omega_-^2}{\omega_L^2} - 1}\frac{z}{2H}\right)\right] + C_2 \exp\left[\frac{z}{2H} + i\left(\Omega_- t + \sqrt{\frac{\Omega_-^2}{\omega_L^2} - 1}\frac{z}{2H}\right)\right]\right\}, \\ \Omega_- > \omega_L \\ \mathrm{Im}\left\{C_1 \exp\left[i\Omega_- t + \left(1 - \sqrt{1 - \frac{\Omega_-^2}{\omega_L^2}}\right)\frac{z}{2H}\right] + C_2 \exp\left[i\Omega_- t + \left(1 + \sqrt{1 - \frac{\Omega_-^2}{\omega_L^2}}\right)\frac{z}{2H}\right]\right\}, \\ \Omega_- < \omega_L. \end{cases} \quad (42)$$

Here,

$$B_1 = \frac{\bar{A}_{12}\Omega_+ e^{i\varphi_1}}{2\left(c_0^2 k_1^2 - \Omega_-^2 - ic_0 k_1/H\right)}, \quad (43)$$

$$B_2 = \frac{\bar{A}_{12}\Omega_- e^{i\varphi_2}}{2i\left(c_0^2 k_2^2 - \Omega_-^2 - ic_0 k_2/H\right)};$$

B_1^* and B_2^* are the corresponding complex conjugate quantities, and C_1 and C_2 are arbitrary constants; the satisfaction of certain conditions must be required for their determination.

One of these conditions follows from relations (3) and corresponds to the absence of a vertical oscillation velocity on an absolutely rigid surface $v_z^{(2)}\big|_{z=0} = 0$. To find another condition, let us analyze the solution $v_{z,H}^{(-)}$ of Eq. (41), whose coefficients B_1 and B_2 are entirely determined by the AGW generation efficiency. As we see from (41), the propagation of Alfvén waves in opposite directions [see (28)] results in the fact that the AGWs at the difference frequency also propagate both upward, with amplitudes B_1 and B_2, and downward, with amplitudes B_1^* and B_2^*. In this case, they are generated by the Alfvén waves propagating in the same direction [the terms with B_1 and B_1^* in (41)] and in opposite directions [the terms with B_2 and B_2^* in (41)]. This implies that, in contrast to the equality $p^{(1)}\big|_{z=0} = 0$ [see (19)], which holds for the linear propagation of AGWs and the corresponding boundary conditions (3), a similar equality for $p^{(2)}$ at the difference frequency does not hold.

In this situation, the equality of the individual terms in expression (40) corresponding to the upward- and downward-propagating AGWs to zero may be considered as a reasonable boundary condition. This boundary condition is not an additional one and has a simple physical meaning: the vertical oscillation velocity becomes zero on an absolutely rigid boundary separately for the upward- and downward propagating AGWs.

The choice of this condition may be considered to be quite justifiable for the following reasons.

First, there is no linear coupling for the the upward- and downward-propagating AGWs in an isothermal atmosphere in the approximation under consideration. That is why we may set the two corresponding conditions, one for each of the waves, which are equivalent to one condition $v_z^{(2)}\big|_{z=0} = 0$.

Second, a qualitative analysis of the causal processes of nonlinear interaction between Alfvén waves indicates that these boundary conditions are valid. Indeed, let us assume that the interaction takes place between time-limited Alfvén waves with frequencies ω_1 and ω_2 and duration $T \ll z_{\rm H}/c_{\rm A}$ propagating in a homogeneous, up to $z = z_{\rm H}$, atmosphere, where a partially reflecting transition layer is located at $z = z_H$. It is then quite natural that only upward-propagating AGWs will be generated in a time $0 \le t \le z_{\rm H}/c_{\rm A}$, for which $v_z^{(2)} = 0$ at the lower boundary. Mostly downward-propagating AGWs will be generated in a time $\frac{z_{\rm H}}{c_{\rm A}} \le t \le 2\frac{z_{\rm H}}{c_{\rm A}}$, for which $v_z^{(2)} = 0$ at $z = 0$ as well. Upward-propagating AGWs, which also become downward-propagating ones after the prior reflection from the $z = z_H$ boundary, will also be simultaneously generated only in the time interval $\frac{z_{\rm H}}{c_{\rm A}} \le t \le \frac{z_{\rm H}}{c_{\rm A}} + T$ that characterizes the reflection. The latter, however, result from the linear reflection at the $z = z_{\rm H}$ boundary of the nonlinearly generated AGWs at $z < z_{\rm H}$. Therefore, they are absent in our case of an isothermal atmosphere [see (1)]. In addition, it should be noted that the boundary condition under discussion does not significantly affect the description of the processes under consideration, because, as was pointed out above, the efficiency of the nonlinear generation of upward- and downward-propagating AGWs is entirely determined by the corresponding forced solution (41), more specifically, by the coefficients B_1, B_2 and B_1^*, B_2^*, respectively.

Thus, the arbitrary constants in system (42) can be defined as

$$C_1 = -(B_1 + B_2), \quad C_2 = -(B_1^* + B_2^*). \qquad (44)$$

The derived expressions (40)–(44) allow us to investigate the efficiency of various mechanisms for the parametric generation of AGWs at the difference frequency by Alfvén waves propagating at $0 \le z \le z_{\rm H}$. To this end, it will suffice to analyze the Ω_- dependence of the corresponding ratio $U = |B_1/B_2|$, which we write using (43) as

$$U = \left\{ \frac{\left(\beta^2 - 1\right)^2 W^2 + \beta^2}{(2W_1 + W)^2 \left[\beta^2 - W^2/(2W_1 + W)^2\right]^2 + \beta^2} \right\}^{1/2}, \qquad (45)$$

where

$$W = \frac{\Omega_-}{\omega_{\rm L}}, \quad W_1 = \frac{\omega_1}{\omega_{\rm L}}. \qquad (46)$$

At the frequencies $W \ll 1$ of major interest well below the cutoff frequency of linear AGWs and for $W_1 \gg 1$, we can derive more clear approximate relations from (45):

$$U \approx \frac{1}{2\beta W_1} \left\{ 1 + \frac{1}{2} \left[\frac{\left(\beta^2 - 1\right)^2}{\beta^2} W^2 - \frac{W}{W_1} \right] \right\}, \qquad (47)$$

$$\left(\beta^2 - 1\right)^2 \ll 1,$$

$$U \approx \frac{1}{2\beta W_1} \qquad (48)$$

$$\times \begin{cases} \left\{ 1 + \frac{1}{2} \left(\frac{1}{\beta} W^2 - \frac{W}{W_1} \right) \right\}, & W \ll \beta \\ \frac{W}{\beta} \left\{ 1 + \frac{1}{2} \left[\frac{\beta^2}{W^2} - \frac{W}{W_1} \right] \right\}, & W \gg \beta, \end{cases}$$

$$(\beta \ll 1),$$

$$U \approx \frac{1}{2W_1\beta} \qquad (49)$$

$$\times \begin{cases} \left\{ 1 + \frac{1}{2} \left[\beta^2 W^2 - \frac{W}{W_1} \right] \right\}, & W \ll \frac{1}{\beta} \\ \beta W \left\{ 1 + \frac{1}{2} \left[\frac{1}{W^2\beta^2} - \frac{W}{W_1} \right] \right\}, & W \gg \frac{1}{\beta}, \end{cases}$$

$$(\beta \gg 1).$$

We see from (47)–(49) that U, according to formula (45), is always smaller than unity; the corresponding dependence on W can have a minimum. Using (47)–(49), we obtain the minimum values of $\bar{U}_j$ corresponding to these approximate relations for $W = \bar{W}_j$ $(j = [1, 3])$:

$$\bar{U}_j = \frac{1}{2\beta W_1} \left(1 - \frac{1}{4} \bar{W}_j / W_1 \right); \qquad (50)$$

$$\bar{W}_1 = \frac{\beta^2}{2\left(\beta^2 - 1\right)^2 W_1}, \qquad (51)$$

$$\bar{W}_2 = \frac{\beta}{2W_1}, \quad \bar{W}_3 = \frac{1}{2\beta^2 W_1}.$$

Since relations (47)–(49) are valid at frequencies $W \ll 1$, we must also require that the conditions

$\bar{W}_j \ll 1$ be satisfied. However, one of them,

$$\frac{\beta^2}{2(\beta^2-1)^2 W_1} \ll 1, \qquad (52)$$

may not be satisfied at $\beta \to 1$. This implies the absence of a minimum in the corresponding relation (47) and, consequently, in $U(W)$ (45) for β close to unity.

The above characteristic patterns in the behavior of $U(W)$, which were clearly demonstrated by our calculations using expression (45) (see Fig. 1), suggest that the nonlinear interaction of oppositely directed Alfvén waves is the predominant parametric generation mechanism of AGWs at the difference frequency. The relative contribution of this AGW generation mechanism increases with fundamental radiation frequency ω_1 and decreases with increasing difference frequency Ω_- for $\beta < 1$ and $\beta > 1$; at $\beta = 1$, it increases only slightly with Ω_-. In addition, as β, which characterizes the ratio of the acoustic and Alfvén wave velocities at the $z = 0$ boundary, increases, the relative contribution of this generation mechanism for $\beta \le 1$ increases over the entire Ω_- range, while for $\beta > 1$, a similar increase in this contribution takes place only at relatively low frequencies, $0 \le \Omega_- \le \Omega_\beta$, because its decrease is observed at $\Omega_- > \Omega_\beta$ (see Fig. 1). At the same time, the frequency Ω_β decreases appreciably with increasing β and increases only slightly with ω_1.

The following important remark should be made regarding the parametric generation of AGWs in the spatial region $0 \le z \le z_H$: we see from (41), (42), and (44) that at the relatively low frequencies of major interest, $0 \le \Omega_- \le \omega_L$, the contribution of nonpropagating waves (oscillations) (42) to the total field (40) begins to dominate with increasing height z over the contribution of propagating waves (41), which generate the corresponding oscillations (42). This effect is particularly pronounced at very low frequencies $\Omega_-/\omega_L \ll 1$, where the amplitude of oscillations (42) excited by downward-propagating waves [see (41)] increases roughly in inverse proportion to the decreasing ambient density. Clearly, this situation is directly opposite to the situation characteristic of the parametric generation of AGWs at $\Omega_- < \omega_L$ by waves of a similar type with frequencies $\omega_1 > \omega_L$ and $\omega_2 > \omega_L$ considered by Petukhov and Petukhov (2001). There is also another fundamental difference from the process described by Petukhov and Petukhov (2001). It shows up in the fact that the nonlinear interaction of Alfvén waves produces no acoustic flow (wind) for $\Omega_- \to 0$, because in contrast to the above paper, we obtain $v_z^{(2)} \to 0$ for $\Omega_- \to 0$ from expressions (40)–(42) and (44).

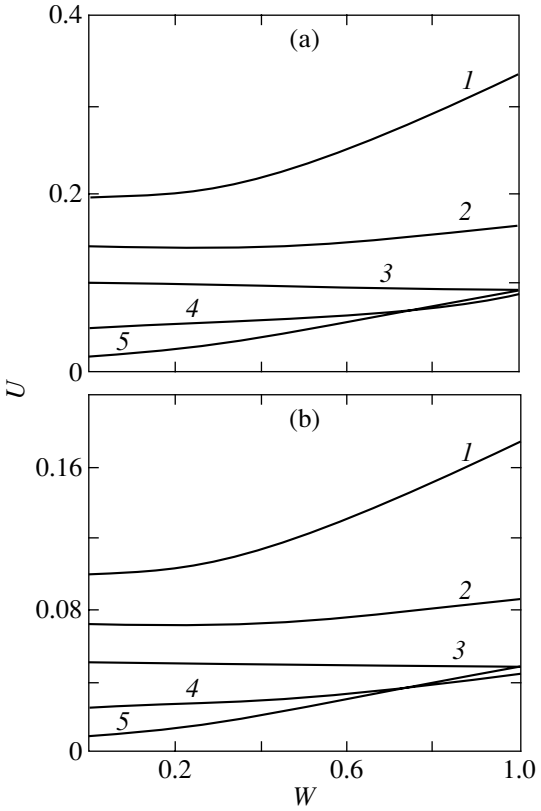

Fig. 1. U [see (45)] versus dimensionless frequency $W = \Omega_-/\omega_L$ at (a) $W_1 = 5$ and (b) $W_1 = 10$. Curves *1–5* correspond to $\beta = 0.5$, 0.7, 1, 2, and 6, respectively.

Let us now study the parametric generation of AGWs for a strong linear coupling of oppositely propagating Alfvén waves (31), which produce weakly varying (with height) oscillations in $v_x^{(1)}$ (32). In this situation, Eq. (34) reduces to

$$\hat{L} v_z^{(2)} = -B_{12} e^{-\frac{z}{H}} \sin(\Omega_- t), \qquad (53)$$

where

$$B_{12} = \frac{A_1 A_2}{2c_0} \beta^2 \frac{\omega_1 \omega_2 \Omega_-}{J_0(b_1) J_0(b_2) \omega_L}. \qquad (54)$$

The general solution of Eq. (53) is the sum of the two corresponding solutions (40), among which only the particular solution of this equation differs from (41) in form:

$$v_{z,H}^{(-)} = \bar{B}_{12} e^{-\frac{z}{H}} \sin(\Omega_- t), \qquad (55)$$

where

$$\bar{B}_{12} = B_{12}/(8\omega_L^2 + \Omega_-^2). \qquad (56)$$

The solution of the homogeneous equation corresponding to (53) is of the same form (42), in which, however, the constants C_1 and C_2 take on values

different from (43), although a relation between them similar to (43) is preserved:

$$C_1 = C_2^*. \quad (57)$$

To successively determine these constants, let us consider a situation in which the initial radiation frequencies ω_1 and ω_2 are low enough, $b_j \ll 1$. The latter allows us to properly use the boundary condition $v_z^{(2)}\Big|_{z=0} = 0$ following from (3). Using (40), (42), and (57), we obtain from this condition

$$C_1 = C_2 = -\frac{1}{2}\bar{B}_{12}. \quad (58)$$

It follows from relations (55) and (56) that in the region of strong linear interaction between Alfvén waves, $z > z_{\rm H}$, the efficiency of the parametric generation of propagating AGWs at the difference frequency decreases with height proportionally to the decreasing ambient density. Consequently, as we see from (41), (42), (44) and (55), (57), the nonpropagating acoustic-gravity disturbances will dominate in the corresponding frequency range $0 < \Omega_- < \omega_{\rm L}$ over the entire height of the atmosphere.

THE NONLINEAR GENERATION OF AGWs AT THE SUM FREQUENCY

During the nonlinear interaction of Alfvén waves, AGWs are generated not only at difference (Ω_-) but also at sum (Ω_+), frequencies. Since the latter process is more efficient than the former for the nonlinear damping of Alfvén waves, we also study this process below. To significantly simplify the algebraic transformations and to derive clear relations for the corresponding quantities, let us consider the generation of the second harmonic to which the following relations between the parameters in boundary condition (3) correspond:

$$\omega_1 = \omega_2 = \omega, \quad A_1 = A_2 = A/2. \quad (59)$$

In this special case [see (59)], three processes, the generation of second harmonics $2\omega_1 = 2\omega, 2\omega_2 = 2\omega$ and the sum frequency $\Omega_+ = \omega_1 + \omega_2 = 2\omega$, are combined into a whole.

Taking into account what was said above [see (3), (59)] and using solutions (20) from (33), we derive the equation

$$\hat{L}v_z^{(2)} = De^{-\frac{z}{2H}} J_1\left(be^{-\frac{z}{2H}}\right) J_0\left(be^{-\frac{z}{2H}}\right) \sin(\Omega_+ t), \quad (60)$$

in which

$$D = \frac{A^2\omega^2}{c_{\rm A0}J_0^2(b)}, \quad b = \frac{\omega}{\omega_{\rm L}}\beta. \quad (61)$$

As before, when obtaining an approximate analytic solution of Eq. (60), we first consider the height range $0 \le z \le z_{\rm H}$ (30), in which there is a weak linear interaction of oppositely directed Alfvén waves. When the corresponding condition (26) is satisfied and when $z/H \le 1$, the right-hand side of Eq. (60) can be simplified using the asymptotics of the Bessel functions to

$$\hat{L}v_z^{(2)} \simeq D_1 \cos\left(2b - \frac{bz}{H}\right) \sin(\Omega_+ t), \quad (62)$$

where

$$D_1 = -\frac{c_{\rm A0}}{\omega 2\pi H} D. \quad (63)$$

By analogy with (40), the general solution of Eq. (62) is the sum

$$v_z^{(2)} = v_{z,H}^{(+)} + v_{z,0}^{(+)}, \quad (64)$$

in which

$$v_{z,H}^{(+)} = {\rm Im}\left\{D_2 e^{i(\Omega_+ t - kz)} + D_2^* e^{i(\Omega_+ t + kz)}\right\} \quad (65)$$

is its particular solution and $v_{z,0}^{(+)}$ is the solution of the corresponding homogeneous equation. Naturally, $v_{z,0}^{(+)}$ is similar in form to $v_{z,0}^{(-)}$ [see (42)], in which the arbitrary constants C_1, C_2 and the frequency Ω_- must be replaced with C_3, C_4 and Ω_+, respectively. Here [see (65)],

$$D_2 = \frac{1}{2}e^{i\varphi}\frac{D_1}{c_0^2k^2 - \Omega_+^2 - i\dfrac{c_0^2}{H}k}, \quad (66)$$

$$k = \frac{b}{H} = \beta\frac{\Omega_+}{2H\omega_{\rm L}}, \quad \varphi = 2b = \beta\Omega_+,$$

and C_3 and C_4 can be determined from similar equalities for C_1 and C_2 [see (44)]:

$$C_3 = -D_2, \quad C_4 = -D_2^*. \quad (67)$$

In the case of an initially strong linear interaction between oppositely directed Alfvén waves, $b \ll 1$, Eq. (60) reduces to an approximate form similar to (53),

$$\hat{L}v_z^{(2)} \simeq Fe^{-z/H}\sin(\Omega_+ t), \quad (68)$$

where

$$F = \frac{A^2 H\omega^3}{c_{\rm A0}^2 J_0^2(b)}. \quad (69)$$

The general solution of Eq. (68) can also be represented as sum (64), in which now

$$v_{z,H}^{(+)} = F_1 e^{-z/H}\sin(\Omega_+ t), \quad (70)$$

where

$$F_1 = -F/\left(\Omega_+^2 + 8\omega_{\rm L}^2\right). \quad (71)$$

In the solution $v_{z,0}^{(+)}$, the corresponding constants are given by

$$C_3 = C_4 = -\frac{1}{2}F_1. \quad (72)$$

The derived solutions (65)–(67) and (70)–(72) lead us to definitive conclusions regarding the behavior of the process under consideration. More specifically, in the frequency range $\Omega_+ > \omega_L$ of major interest, the amplitude of the propagating AGWs increases with height in inverse proportion to the square root of the decreasing ambient density. In contrast, at relatively low frequencies, $\Omega_+ < \omega_L$, as in the case of Ω_- generation, the contribution of the nonpropagating acoustic-gravity disturbances to the total field dominates; at very low frequencies, $\Omega_+ \ll \omega_L$, their amplitude increases with height in inverse proportion to the decreasing ambient density.

In the corresponding ranges of radiation frequencies, the frequency dependences of the AGW amplitudes $v_m = \max\left\{v_z^{(+)}\right\}$ also differ significantly:

$$v_m \sim \begin{cases} \omega^3, \quad \omega \ll \omega_L/\beta, & \begin{cases} \beta > 1 \\ \beta < 1 \end{cases} \\ \dfrac{\omega}{\cos^2\left(\beta\dfrac{\omega}{\omega_L} - \dfrac{\pi}{4}\right)}, & \omega \gg \omega_L/\beta, \quad \beta \to 1 \\ \dfrac{1}{\cos^2\left(\beta\dfrac{\omega}{\omega_L} - \dfrac{\pi}{4}\right)}, & \omega \gg \omega_L/\beta, \begin{cases} \beta \ll 1 \\ \beta \gg 1. \end{cases} \end{cases} \quad (73)$$

As in the description of the generation of difference frequencies Ω_-, our conclusions concerning the generation of second harmonics are valid for radiation frequencies that differ markedly from the resonance frequencies $\bar{\omega}_n$ (22).

CONCLUSIONS

Let us formulate our main results and the conclusions that follow from them.

We investigated the parametric generation of acoustic-gravity disturbances of Alfvén waves propagating along the corresponding field lines in terms of a simple plane-parallel isothermal model solar atmosphere permeated by a uniform magnetic field directed against the action of gravity.

We established that the nonlinear interaction of oppositely propagating Alfvén waves is the predominant parametric generation mechanism of AGWs at the difference frequency in the radiation frequency range and at atmospheric heights where a weak linear coupling of Alfvenén waves takes place.

We showed that the contribution of this generation mechanism of acoustic-gravity disturbances relative to the corresponding contribution from the nonlinear interaction of Alfvén waves propagating in the same direction increases with increasing initial radiation frequency of the latter and decreases with increasing difference frequency.

We found that at the difference frequencies of major interest below the Lamb cutoff frequency, the contribution of nonpropagating acoustic-gravity disturbances to the total field begins to dominate with increasing height over the corresponding contribution of propagating AGWs. It should be noted that this situation is opposite to the situation characteristic of the nonlinear interaction of propagating AGWs in the absence of a magnetic field in the solar atmosphere (see Petukhov and Petukhov 2001).

We also proved that, in contrast to the nonlinear interaction of propagating AGWs (see Petukhov and Petukhov 2001), the nonlinear interaction of Alfvén waves does not give rise to an acoustic flow (wind) in their generated field of AGWs at a zero difference frequency.

We pointed out that at sum frequencies above the Lamb cutoff frequency, the amplitude of the propagating AGWs increases with height in inverse proportion to the square root of the decreasing ambient density, i.e., much more slowly than for the processes considered in Petukhov and Petukhov (2001) where this quantity would change in inverse proportion to the density in the corresponding case of initially propagating primary waves. Only at frequencies much lower than the Lamb cutoff frequency does the amplitude of the nonpropagating AGWs increase with height in inverse proportion to the decreasing ambient density. This is in contrast to our previous results (see Petukhov and Petukhov 2001), where this quantity changes much more slowly, more specifically, in inverse proportion to the density to the power equal to the square of the small (compared to unity) radiation-to-Lamb frequency ratio.

Thus, our studies suggest that weakly nonlinear Alfvén waves can be effectively involved in heating the solar upper chromosphere and corona through their generation of propagating AGWs over the entire range of their frequencies. However, the latter can also take place only when Alfvén waves are excited at relatively high frequencies, for which the spatial regions of weak linear interaction between these waves [see (26)] extend to the corresponding atmospheric heights, which was previously disregarded (Priest 1982; Uchida and Kabuaki 1974; Wentzel 1974). In this case, in contrast to the fairly intense Alfvén waves, which can transform into fast shock waves under certain conditions (Galloway *et al.* 1982; Kudoh and Shibata 1999) while propagating in

open magnetic flux tubes, the weakly nonlinear Alfvén waves considered here cannot produce upward-directed flows.

ACKNOWLEDGMENTS

This study was supported by the Russian Foundation for Basic Research (project nos. 00-15-96619 and 00-15-96591).

REFERENCES

1. M. Abramowitz and I. A. Stegun, *Handbook of Mathematical Functions* (National Bureau of Standards, Washington, 1964; Nauka, Moscow, 1979).
2. *Advances in Solar System Magnetohydrodynamics,* Ed. by E. R. Priest and A. W. Wood (Cambridge Univ. Press, Cambridge, 1991; Mir, Moscow, 1995).
3. D. Banarjee, J. Christensen-Dalsgaard, and S. S. Hasan, Astrophys. J. **451**, 825 (1995).
4. V. D. Brengauz, Izv. Vyssh. Uchebn. Zaved., Radiofiz. **12**, 145 (1969).
5. V. D. Brengauz, Izv. Vyssh. Uchebn. Zaved., Radiofiz. **17**, 192 (1974).
6. Y. T. Chiu, Phys. Fluids **14**, 1717 (1971).
7. J. Christensen-Dalsgaard and S. S. Hasan, Astrophys. J. **396**, 311 (1992).
8. R. H. Cohen and R. M. Kulsrud, Phys. Fluids **17**, 2215 (1974).
9. É. E. Dubov, Itogi Nauki Tekh., Astron. **14**, 148 (1978).
10. V. C. A. Ferraro and C. Plumpton, Astrophys. J. **127**, 459 (1958).
11. A. Frank, T. W. Jones, and D. Ryu, Astrophys. J. **452**, 785 (1995).
12. D. Galloway, J. V. Hollweg, and S. Jackson, Sol. Phys. **75**, 35 (1982).
13. G. Herbold, R. Rosner, and P. Ulmschneider, Astron. Astrophys. **145**, 157 (1985).
14. J. V. Hollweg, Sol. Phys. **62**, 227 (1979).
15. J. V. Hollweg, Sol. Phys. **70**, 25 (1981).
16. J. V. Hollweg, Astrophys. J. **254**, 806 (1982).
17. J. V. Hollweg and A. C. Sterling, Astrophys. J. **327**, 950 (1988).
18. V. N. Kaplan, S. B. Pikel'ner, and V. N. Tsytovich, *Physics of Solar Atmospheric Plasma* (Nauka, Moscow, 1977).
19. T. Kudoh and K. Shibata, Astrophys. J. **514**, 493 (1999).
20. B. C. Low, Astrophys. J. **254**, 796 (1982).
21. Y. Nakagawa, E. R. Priest, and R. E. Wellck, Astrophys. J. **184**, 931 (1973).
22. M. Yu. Petukhov and Yu. V. Petukhov, Pis'ma Astron. Zh. **27**, 220 (2001) [Astron. Lett. **27**, 186 (2001)].
23. E. R. Priest, *Solar Magnetohydrodynamics* (Reidel, Dordrecht, 1982; Mir, Moscow, 1985).
24. O. V. Rudenko and S. I. Soluyan, *Theoretical Foundations of Nonlinear Acoustics* (Nauka, Moscow, 1975; Consultants Bureau, New York, 1977).
25. A. B. Severnyi, *Some Problems of Solar Physics* (Nauka, Moscow, 1988).
26. Y. Uchida and O. Kabuaki, Sol. Phys. **35**, 451 (1974).
27. S. V. Vorontsov and V. N. Zharkov, Itogi Nauki Tekh., Astron. **38**, 253 (1988).
28. D. G. Wentzel, Sol. Phys. **39**, 129 (1974).

Translated by V. Astakhov

Astronomy Letters, Vol. 28, No. 5, 2002, pp. 345–352. Translated from Pis'ma v Astronomicheskiĭ Zhurnal, Vol. 28, No. 5, 2002, pp. 393–400.

Calculating the Potential Magnetic Field of a Local Region on the Sun Using the Measured Oblique Component

O. G. Den*

Institute of Terrestrial Magnetism, Ionosphere and Radiowave Propagation, Russian Academy of Sciences, Troitsk, 141090 Russia

Received November 8, 2001

Abstract—We propose a method for solving the Neumann boundary-value problem using the known magnetic-field component at the boundary in a specified direction (the oblique-derivative problem). The method allows the normal field component at the boundary to be directly determined from the measured line-of-sight component. This makes it possible to calculate the potential magnetic field in the corona above a region far removed from the solar-disk center. A model potential magnetic field is used as an example to test our method. © *2002 MAIK "Nauka/Interperiodica"*.

Key words: *Sun, solar magnetic fields, corona*

INTRODUCTION

When the solar magnetic field is measured, its line-of-sight component at the photospheric level is customarily determined from the Zeeman effect. Using these data as the boundary condition allows the coronal magnetic field to be calculated.

To a first approximation, the solar magnetic field may be assumed to be potential. Strong large-scale electric currents are required to appreciably change the potential magnetic-field configuration (Levine and Altschuler 1974). The potential field determines the overall topology of active regions and the locations of flares, prominences, and other active structures. The role of the potential field and the relationship between the potential and nonpotential (current) magnetic-field components of active regions were discussed in detail by Somov (2000) in his monograph. In this paper, we consider one important aspect of the problem of calculating the field using measurements.

The classical statement of the problem of calculating the potential field is the external Neumann boundary-value problem—solving the Laplace equation for a potential with the normal-field distribution specified at the boundary. There are two methods for solving this problem. The first method consists in representing the potential in integral form by the Green function; it allows the field above the boundary to be directly calculated (Schmidt 1964). The second method involves expanding the potential in terms of the eigenfunctions that satisfy the Laplace equation. The expansion in terms of associated Legendre polynomials (spherical functions) for the Sun as a whole (Altschuler and Newkirk 1969) and the Fourier expansion, as a rule, for a selected region (Nakagawa and Raadu 1972; Nakagawa 1973; Levine and Altschuler 1974; Adams and Pneuman 1976) are used. Once the required number of terms has been specified, the expansion coefficients can be determined from the fitting of the solution to the boundary condition by least squares. In other words, the accuracy of the solution is limited by the accuracy of the least-squares method from the outset (Sakurai 1982). In addition, using the Fourier expansion for a specific region presupposes a periodic extension of the solution to the entire solar surface (Levine 1975). Therefore, the solution by the Green-function method seems preferable.

Unfortunately, the region of interest is not always located near the solar-disk center, where the line of sight coincides with the normal to the surface. For example, when calculating the critical prominence height (Fillipov and Den 2000), we have to restrict ourselves to low-latitude prominences. Determining the coronal magnetic field for solar regions far removed from the disk center is related to the so-called oblique-derivative problem (Mikhlin 1968). In this paper, we present our method for solving the oblique-derivative problem, which may be called the method of integral iterations. It allows the magnetic-field component normal to the region boundary to be directly determined from the measured line-of-sight component.

*E-mail: Den@izmiran.troitsk.ru

1063-7737/02/2805-0345$22.00

SOLVING THE OBLIQUE-DERIVATIVE PROBLEM BY THE METHOD OF INTEGRAL ITERATIONS

Semel (1967) attempted to solve the oblique-derivative problem. To this end, he considered the Dirichlet boundary-value problem for the magnetic-field component along the line of sight and took the line-of-sight component at the boundary as the boundary condition. Subsequently, the potential was calculated by integrating the derived solution along the line coincident with the line of sight. Sakurai (1982) showed that Semel's solution for the potential could be represented as

$$\varphi(\mathbf{r}) = \frac{1}{2\pi}\int\limits_{s'} B_l(\mathbf{r}')\,G(\mathbf{r},\mathbf{r}')\,ds', \qquad (1)$$

$$G(\mathbf{r},\mathbf{r}') = \frac{1}{2\pi}\left[\frac{\mathbf{n}\cdot\mathbf{l}}{R} + \frac{\boldsymbol{\mu}\cdot\mathbf{R}}{R(R+\mathbf{l}\cdot\mathbf{R})}\right], \qquad (2)$$

where $\mathbf{R} = \mathbf{r} - \mathbf{r}'$; $\mathbf{n}$ and $\mathbf{l}$ are the unit vectors along the normal and the line of sight, respectively; and $\boldsymbol{\mu} = \mathbf{l}\times(\mathbf{n}\times\mathbf{l})$. The first term on the right-hand side of Eq. (2) represents the contribution of the monopole with magnetic flux $2\mathbf{n}\cdot\mathbf{l}$, and the second term gives the contribution of the dipoles with moment $\boldsymbol{\mu}/2\pi$ per unit length distributed along the direction opposite to the line of sight ($-\mathbf{l}$) from $\mathbf{r}'$ to $-\infty$.

The following can be said regarding Semel's solution. In general, the solution of the homogeneous Laplace equation for the potential by using the Green-function method is (Koshlyakov *et al.* 1970; Korn and Korn 1968)

$$\varphi(r) = \int\limits_{s'} \left.\frac{\partial\varphi}{\partial n}\right|_{s'} G(r,r')\,ds' - \int\limits_{s'}\varphi(r')\frac{\partial G(r,r')}{\partial n}ds'. \qquad (3)$$

If the Green function $G(r,r')$ is zero at the boundary, then we have the Dirichlet problem [the second term in Eq. (3)]; if the normal derivative of $G(r,r')$ is zero at the boundary, then we have the Neumann problem [the first term in Eq. (3)]. Since Semel used the typical Green function $\dfrac{1}{2\pi|\mathbf{r}-\mathbf{r}'|}$, which is nonzero at the boundary, to solve the Dirichlet problem for the field component B_l, the condition $\dfrac{\partial B_l}{\partial n} = 0$ must be satisfied at the boundary. This requires an artificial construction of the magnetic-field sources.

Below, by comparison with a model field, we show that Semel's solution is approximate.

The solution of the Neumann problem by using the Green-function method for an infinite plane is given by (Schmidt 1964)

$$\mathbf{B}(x,y,z) = \frac{1}{2\pi}\int\limits_{s'}\frac{B_n(x',y',0)\,\mathbf{r}}{r^3}\,dx'dy', \qquad (4)$$

where $B_n(x',y',0)$ is the normal surface magnetic-field component and $r = ((x-x')^2 + (y-y')^2 + z^2)^{1/2}$ is the distance from the point under consideration to the point on the surface. Solution (4) can also be obtained from the solution of the external Neumann problem for a sphere when the sphere radius tends to infinity (Koshlyakov *et al.* 1970).

The idea of solving the oblique-derivative problem by the method of integral iterations was put forward by Den *et al.* (1979). Let us choose a coordinate system whose Z axis coincides with the normal to the surface. Let the magnetic vector $\mathbf{B}$ in this coordinate system have the B_x, B_y, and B_z components. For the field component along a direction $\mathbf{l}$ coincident with the line of sight, we can then write

$$B_l = B_x\cos\alpha + B_y\cos\beta + B_z\cos\gamma, \qquad (5)$$

where α, β, and γ are the angles between the specified direction $\mathbf{l}$ and the coordinate axes. Let us now consider Eq. (5) for the boundary surface on which the line-of-sight component is specified. For the normal component, we have

$$B_n(x,y,0) = \frac{B_l(x,y,0)}{\cos\gamma} - \frac{\cos\alpha}{\cos\gamma}B_x(x,y,0) - \frac{\cos\beta}{\cos\gamma}B_y(x,y,0), \qquad (6)$$

where $B_x(x,y,0)$ and $B_y(x,y,0)$ are the field components determined from Eq. (4). These field components determined from the solution of the Neumann problem cannot be numerically calculated at the boundary, because the boundary is singular. However, Den *et al.* (1979) proposed the following procedure for calculating integrals (4): within the magnetograph resolution cell, the measured magnetic-field strength may be assumed to be constant; within this cell, the integration in (4) was performed analytically and the surface integration was replaced with the summation over such cells. After this procedure, any singularities at the boundary in the expressions for $B_x(x,y,0)$ and $B_y(x,y,0)$ disappear.

Without loss of generality, we assume for simplicity that one of the coordinate axes, for example, the Y axis, is perpendicular to the line of sight, $\cos\beta = 0$; in that case, $\cos\alpha = \sin\gamma$. Substituting the expression for B_x from Eq. (4) in Eq. (6) yields

$$B_n(x,y,0) = \frac{B_l(x,y,0)}{\cos\gamma} \qquad (7)$$

$$-\tan\gamma\frac{1}{2\pi}\int\limits_{s'}\frac{B_n(x',y',0)\,(x-x')}{r^3}\,dx'dy'.$$

Equation (7) is an integral equation for B_n. We solve it through iterations by sequentially substituting the right-hand side of Eq. (7) for B_n under the integral sign. Denoting

$$|x|\phi|x'| = \frac{1}{2\pi}\int\limits_{s'}\frac{\phi(x',y',0)(x-x')}{r^3}dx'dy', \quad (8)$$

we can then write

$$\begin{aligned} &B_n(x,y,0)\cos\gamma - B_l(x,y,0) \quad (9)\\ &= -\tan\gamma|x|B_l|x'| + \tan^2\gamma|x|x'|B_l|x''|x'|\\ &-\tan^3\gamma|x|x'|x''|B_l|x'''|x''|x'| + \ldots\\ &+(-1)^n\tan^n\gamma|x|x'\ldots|x^{(n-1)}|B_l|x^{(n)}|\ldots x''|x'|\\ &+(-1)^{n+1}\tan^n\gamma\\ &\times\sin\gamma|x|x'\ldots|x^{(n)}|B_n|x^{(n+1)}|\ldots x''|x'|, \end{aligned}$$

or in the form of an infinite series,

$$\begin{aligned} B_n(x,y,0) &= \frac{B_l}{\cos\gamma} - \frac{\tan\gamma}{\cos\gamma}\left\{\left|x\,|B_l|\,x'\right| \quad (10)\right.\\ &-\tan\gamma\left|x\left|x'\,|B_l|\,x''\right|x'\right|\\ &+\tan^2\gamma\left|x\left|x'\left|x''\,|B_l|\,x'''\right|x''\right|x'\right| - \ldots\\ &+(-1)^{n-1}\tan^{n-1}\gamma\\ &\times\left.\left|x\left|x'\ldots\left|x^{(n-1)}\,|B_l|\,x^{(n)}\right|\ldots x''\right|x'\right| + \ldots\right\}. \end{aligned}$$

Here, $x', x''\ldots x^{(n+1)}$ are the dummy variables of integration over one of the coordinates X. Thus, the normal magnetic-field component can be expressed as an infinite alternating series. The factor $\tan\gamma$ is the parameter that ensures the convergence of the series; i.e., the condition $\tan\gamma < 1$ or $\gamma < 45^\circ$ must be satisfied. This factor determines the number of terms in the series that provide the desired accuracy of the calculation.

We can derive a general formula for the normal field component for an arbitrary angle γ. To this end, consider $\bar{\mathbf{i}}$, $\mathbf{j}$, and $\bar{\mathbf{k}}$ as the unit basis vectors; the new unit vectors $\bar{\mathbf{i}}$ and $\bar{\mathbf{k}}$ can be obtained from the old $\mathbf{i}$ and $\mathbf{k}$ by rotation about the Y axis through angle θ (the positive angle is measured counterclockwise). In that case,

$$\mathbf{B} = \mathbf{i}B_x + \mathbf{j}B_y + \mathbf{k}B_z$$

in the old basis vector system and

$$\mathbf{B} = \bar{\mathbf{i}}B_{\bar{x}} + \mathbf{j}B_y + \bar{\mathbf{k}}B_{\bar{z}}$$

in the new basis vector system.

The vector components in the old and new basis systems are related by the same relations as those for the coordinates when rotating the coordinate system, in our case, through angle θ about the Y axis. For B_z, we can therefore write

$$B_z = -B_{\bar{x}}\sin\theta + B_{\bar{z}}\cos\theta. \quad (11)$$

For the line-of-sight component (given that the Y axis is perpendicular to the line of sight), we have

$$B_l = B_{\bar{x}}\sin(\gamma-\theta) + B_{\bar{z}}\cos(\gamma-\theta)$$

or

$$B_{\bar{z}} = \frac{B_l}{\cos(\gamma-\theta)} - B_{\bar{x}}\tan(\gamma-\theta). \quad (12)$$

Substituting (12) in (11) yields

$$\begin{aligned} B_n(x,y,0) &= B_z(x,y,0) \quad (13)\\ &= \frac{B_l\cos\theta}{\cos(\gamma-\theta)} - \frac{B_{\bar{x}}\sin\gamma}{\cos(\gamma-\theta)}. \end{aligned}$$

Taking the projection of (4) onto the direction $\bar{\mathbf{i}} = \mathbf{i}\cos\theta - \mathbf{k}\sin\theta$, we obtain

$$\begin{aligned} B_{\bar{x}}(x,y,0) &= \lim_{z\to 0}\frac{1}{2\pi} \quad (14)\\ &\times\int\limits_{s'}\frac{B_n(x',y',0)\,[(x-x')\cos\theta - z\sin\theta]}{r^3}\,dx'dy'\\ &= \lim_{z\to 0}\frac{1}{2\pi}\int\limits_{s'}\frac{B_n(x',y',0)(x-x')\cos\theta}{r^3}dx'dy'\\ &-\lim_{z\to 0}\frac{1}{2\pi}\int\limits_{s'}\frac{B_n(x',y',0)z\sin\theta}{r^3}\,dx'dy'. \end{aligned}$$

It seems obvious that the second term in Eq. (14), by analogy with the Dirac delta function, is equal to $B_n(x,y,0)\sin\theta$. This is shown in the Appendix by using the formula for B_z from Den *et al.* (1979).

Thus, substituting expression (13) for B_n, we can transform Eq. (14) to the form

$$B_{\bar{x}}(x,y,0) = \lim_{z\to 0}\frac{1}{2\pi}\int\limits_{s'}\frac{\left[\dfrac{B_l\cos\theta}{\cos(\gamma-\theta)} - B_{\bar{x}'}\dfrac{\sin\gamma}{\cos(\gamma-\theta)}\right][(x-x')\cos\theta - z\sin\theta]}{r^3}dx'dy' \quad (15)$$

$$= \frac{\cos\theta}{\cos(\gamma-\theta)}\left[\lim_{z\to 0}\frac{1}{2\pi}\int\limits_{s'}\frac{B_l(x-x')\cos\theta dx'dy'}{r^3} - B_l(x,y,0)\sin\theta\right]$$
$$-\frac{\sin\gamma}{\cos(\gamma-\theta)}\lim_{z\to 0}\frac{1}{2\pi}\int\limits_{s'}\frac{B_{\bar{x}'}\left[(x-x')\cos\theta - z\sin\theta\right]dx'dy'}{r^3}.$$

Equation (15) is an integral equation for $B_{\bar{x}}$. We solve it by analogy with the solution of Eq. (7) using the iteration method by sequentially substituting the right-hand side of Eq. (15) for $B_{\bar{x}}$ under the integral sign. Knowing $B_{\bar{x}}$, we can derive the normal component from Eq. (13).

Denoting

$$\left[x\left[\psi\right]x'\right] = \lim_{z\to 0}\frac{1}{2\pi} \times \int\limits_{s'}\frac{\psi(x',y',0)\left[(x-x')\cos\theta - z\sin\theta\right]dx'dy'}{r^3}, \quad (16)$$

$$k_1 = \frac{\cos\theta\sin\gamma}{\cos^2(\gamma-\theta)}, \quad k = \frac{\sin\gamma}{\cos(\gamma-\theta)}, \quad (17)$$

we derive the following expression for the normal component:

$$B_n(x,y,0) = \frac{B_l\cos\theta}{\cos(\gamma-\theta)} - k_1\Big\{\left[x\left[B_l\right]x'\right] - k\left[x\left[x'\left[B_l\right]x''\right]x'\right] + k^2\left[x\left[x'\left[x''\left[B_l\right]x'''\right]x''\right]x'\right] - \ldots + (-1)^{n-1}k^{n-1} \times \left[x\left[x'\left[\ldots\left[x^{(n-1)}\left[B_l\right]x^{(n)}\right]\ldots\right]x''\right]x'\right] + (-1)^n\frac{\cos(\gamma-\theta)}{\cos\theta}k^n \times \left[x\left[x'\left[\ldots\left[x^{(n-1)}\left[B_{\bar{x}^{(n)}}\right]x^{(n)}\right]\ldots\right]x''\right]x'\right]\Big\}, \quad (18)$$

or in the form of an infinite series,

$$B_n(x,y,0) = \frac{B_l\cos\theta}{\cos(\gamma-\theta)} - k_1\Big\{\left[x\left[B_l\right]x'\right] - k\left[x\left[x'\left[B_l\right]x''\right]x'\right] + k^2\left[x\left[x'\left[x''\left[B_l\right]x'''\right]x''\right]x'\right] - \ldots + (-1)^n k^n \times \left[x\left[x'\left[\ldots\left[x^{(n)}\left[B_l\right]x^{(n+1)}\right]\ldots\right]x''\right]x'\right] + \ldots\Big\}. \quad (19)$$

Clearly, Eq. (19) transforms to Eq. (10) at $\theta = 0$. The convergence of series (19) requires that the condition $k < 1$ be satisfied. Let us determine the angles θ for which this condition is satisfied:

$$k = \frac{\sin\gamma}{\cos(\gamma-\theta)} < 1$$

or

$$\sin\gamma < \cos(\gamma-\theta),$$

i.e.,

$$\theta > 2\gamma - \frac{\pi}{2}.$$

For $\theta = \gamma$, k takes on the smallest value of $\sin\gamma$ and series (19) converges most rapidly. For this case, we can derive the following expression from Eq. (19):

$$B_n(x,y,0) = B_l\cos\gamma - \cos\gamma\sin\gamma\Big\{\left[x\left[B_l\right]x'\right] - \sin\gamma\left[x\left[x'\left[B_l\right]x''\right]x'\right] + \sin^2\gamma\left[x\left[x'\left[x''\left[B_l\right]x'''\right]x''\right]x'\right] - \ldots + (-1)^n\sin^n\gamma \times \left[x\left[x'\left[\ldots\left[x^{(n)}\left[B_l\right]x^{(n+1)}\right]\ldots\right]x''\right]x'\right] + \ldots\Big\}, \quad (20)$$

which we use in the subsequent calculations.

TESTING THE METHOD ON A MODEL FIELD

To test our method, we performed a comparative analysis with accurate model magnetic field strengths. Figure 1 shows the October 13, 1999, magnetogram of a solar region in the northern hemisphere near the central meridian.

In the upper part of the region, a filament was observed on the inverse polarity line. The magnetic field of this region was roughly modeled by four charges located at different depths beneath the photosphere. The positions and magnitudes of the charges and their depths were determined from the condition that the location of the neutral line with the filament and the field strengths on this line corresponded to the actual parameters of the region. After fitting the model parameters, we could calculate the accurate model field at any point in the selected region.

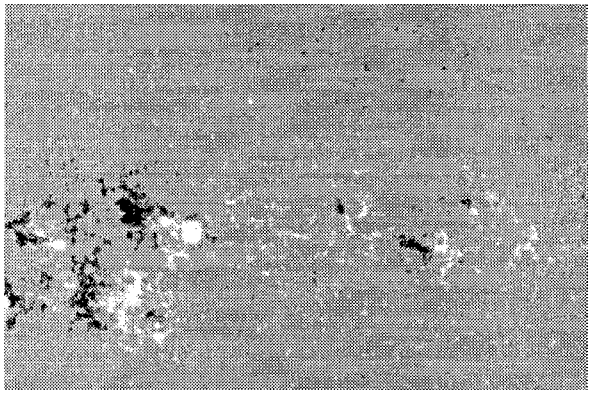

Fig. 1. The October 13, 1999, magnetogram of a solar region in the northern hemisphere near the central meridian. Data from the MDI instrument on the SOHO spaceborne observatory (with permission of the SOHO MDI Consortium; SOHO is a joint ESA–NASA program.).

Figure 2 shows isolines of the October 13, 1999, magnetogram, and Fig. 3 shows isolines of the line-of-sight field component modeled by four charges. Below, the unit of scale along the axes corresponds to two magnetogram pixels, where one pixel ≈2.9 Mm. As we see from a comparison of the two figures, the salient features of the magnetogram field are reflected in the model field.

At Z = 0 corresponding to the photospheric level, we determined the distribution of the oblique (line-of-sight) model magnetic-field component within the selected region and calculated the normal component from formula (20).

For our calculation, we took an 80×120 matrix with 1.25×1.25 cells. Below, we provide plots of a horizontal (along the Y axis) cut across the region center. Figure 4 shows plots of the model oblique component for $\gamma = 40°$ and 70°. The problem was to determine the normal component, which is also shown in this figure, from these components.

Figure 5 shows the computed normal component for these angles. We see good agreement with the accurate (analytically calculated) model field. In our calculation, we took such a number of terms in the series of formula (20) that the accuracy of our calculation was no less than 10^{-3}–10^{-4}. The curve for $\gamma = 70°$ is also seen to coincide with the accurate field slightly worse than that for $\gamma = 40°$. This can be explained as follows. As we see from Fig. 4, the oblique component for $\gamma = 70°$ has sharper peaks than that for $\gamma = 40°$ and the cell size assumed in our calculation does not provide their resolution.

To elucidate this issue, Fig. 6 shows plots of the computed normal component for the angle 40° and the cell sizes $d = 1.25$ and $d = 2.5$. The coincidence with the accurate field for the curve with $d = 2.5$ is much worse.

Thus, as the size of the cell within which the field is assumed to be constant decreases, the observed small deviations from the accurate field must disappear. It should be noted that the agreement at the region edges is poorer, because there are no data outside the region (the effect of a finite region size).

Let us now consider the question of how Semel's solution given above is related to our solution. To this end, we take the accurate line-of-sight model-field component for $\gamma = 70°$ as the input data and calculate the B_z field component at the height $z = 25$ by using Semel's formula and our method. Figure 7 shows these calculations together with the accurate model field. The solution obtained by our method is closer to the accurate field. As was explained above for Figs. 4–6, the observed discrepancy results from an insufficient field resolution for the cell size used. At the same time, the discrepancy between Semel's solution and the accurate field appears to be attributable solely to the approximate nature of his solution.

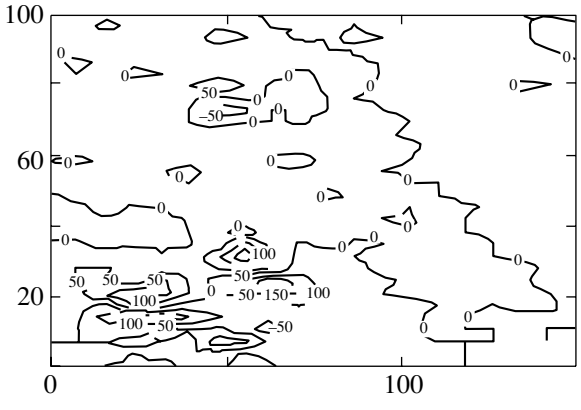

Fig. 2. Isolines of the October 13, 1999, magnetogram (in G).

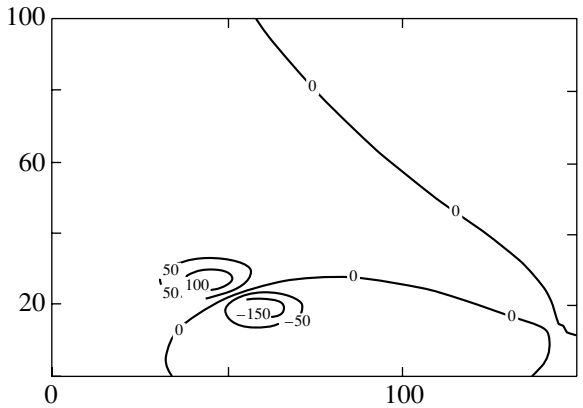

Fig. 3. Isolines of the model field (in G).

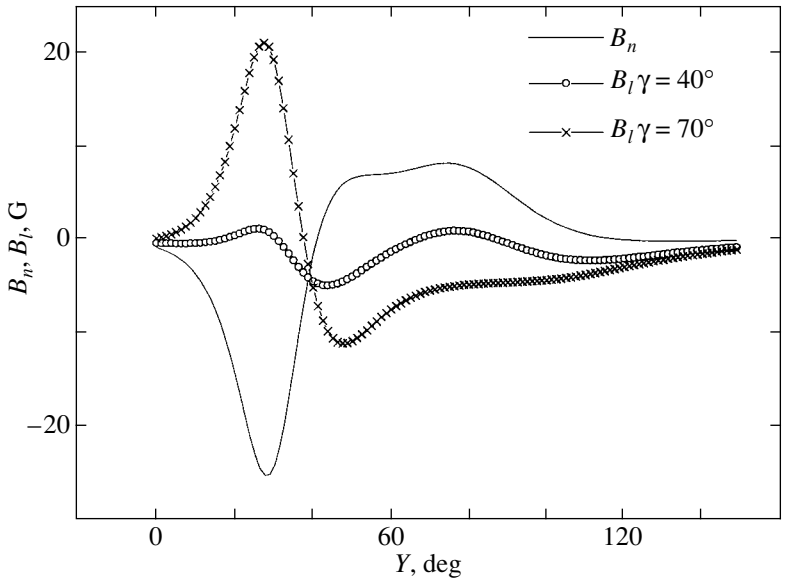

Fig. 4. The normal and oblique model-field components for $\gamma = 40°$ and 70°.

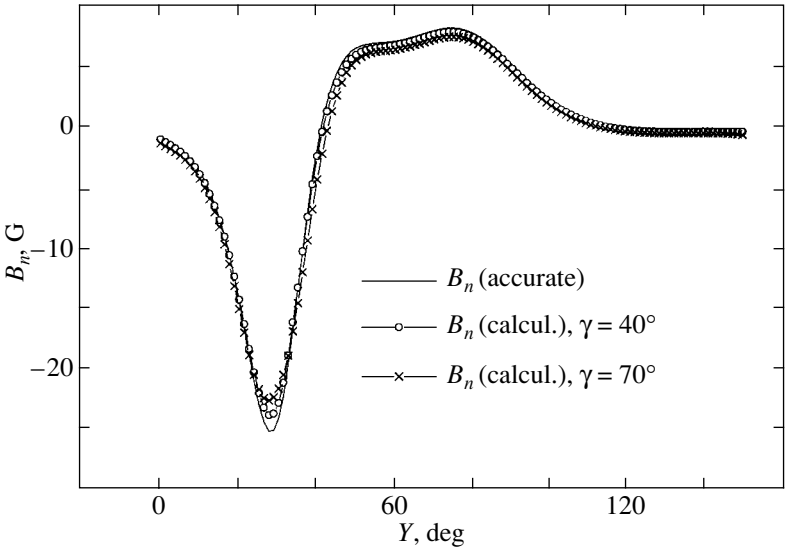

Fig. 5. The accurate and computed normal components for $\gamma = 40°$ and 70°.

CONCLUSIONS

We have proposed a method for solving the oblique-derivative problem by calculating the field component normal to the boundary in the form of an infinite alternating series with the convergence factor $\sin\gamma$. It allows the number of terms in the series that provide the desired accuracy of the calculation to be determined. The accuracy of the method also depends on the size of the cell (the smaller the size, the higher the accuracy) within which the field strength is assumed to be constant.

ACKNOWLEDGMENTS

This study was supported by the State Science and Technology Program "Astronomy" and the Russian Foundation for Basic Research (project no. 00-02-17736).

APPENDIX

We make use of the formula for B_z from Den *et al.* (1979):

$$B_z = \frac{1}{2\pi}\sum_{i,j} B_n^{ij} I_z^{ij}, \qquad \text{(A.1)}$$

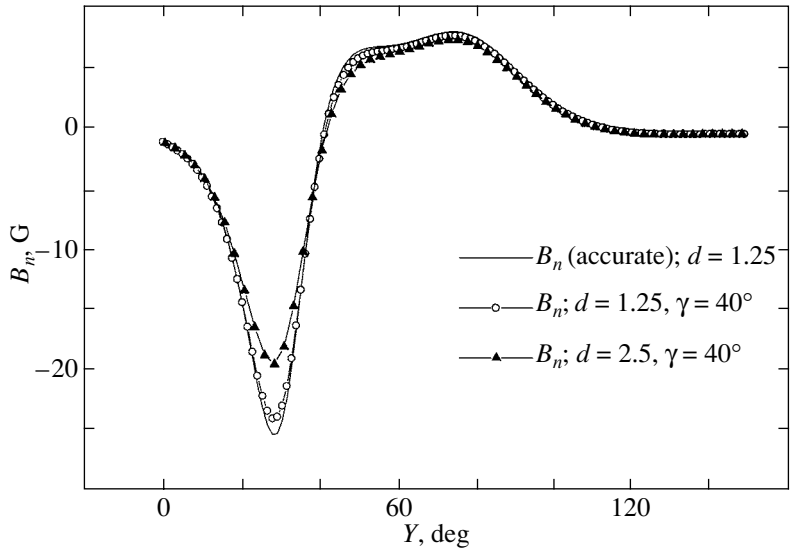

Fig. 6. The computed normal component for $\gamma = 40^\circ$ and the cell sizes $d = 1.25$ and 2.5.

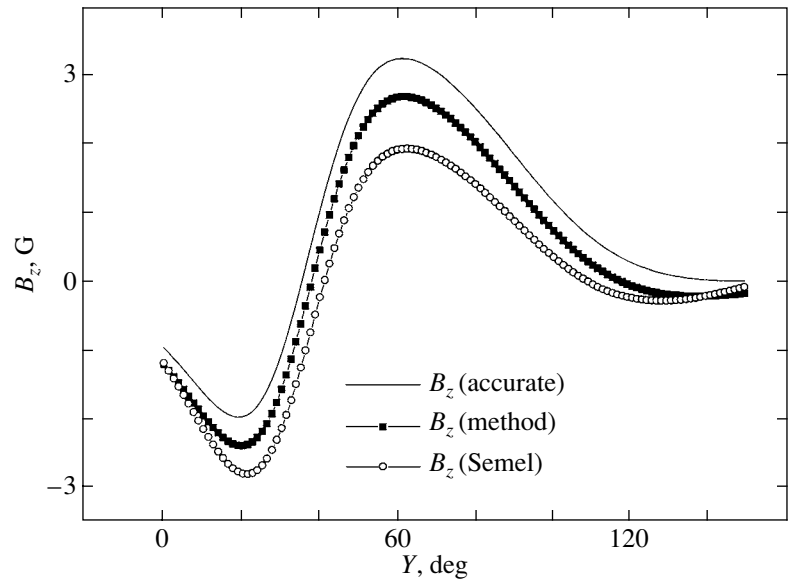

Fig. 7. The B_z field component at the height $z = 25$. The accurate model values and the field calculated by using our method and Semel's formula.

$$I_z = \int_{y_j}^{y_{j+1}} \int_{x_i}^{x_{i+1}} \frac{z\,dx'dy'}{r^3} \qquad \text{(A.2)}$$

$$= \arctan \frac{m_1 p_1}{z\sqrt{m_1^2 + p_1^2 + z^2}}$$

$$+ \arctan \frac{m_2 p_2}{z\sqrt{m_2^2 + p_2^2 + z^2}}$$

$$- \arctan \frac{m_2 p_1}{z\sqrt{m_2^2 + p_1^2 + z^2}}$$

$$- \arctan \frac{m_1 p_2}{z\sqrt{m_1^2 + p_2^2 + z^2}},$$

where $m_1 = x - x_{i+1}$, $m_2 = x - x_i$; $p_1 = y - y_{j+1}$, $p_2 = y - y_j$; and (x_i, y_j), (x_{i+1}, y_{j+1}) are the coordinates of the cell boundary. The summation in Eq. (A.1) is performed over all such cells. We consider the cell centers as x, y.

Consider B_z for $z \to 0$. In that case, $I_z = \frac{\pi}{2} + \frac{\pi}{2} - \frac{\pi}{2} - \frac{\pi}{2} = 0$ for the cells located outside the point x, y. Only for the cell with $m_1 = -m_2$ and $p_1 = -p_2$ (the

x, y coordinates correspond to the cell center),

$$I_z = 4 \lim_{z\to 0} \arctan \frac{m_2 p_2}{z\sqrt{m_2^2 + p_2^2 + z^2}} = 4\frac{\pi}{2} = 2\pi,$$

i.e.,

$$\lim_{z\to 0} B_z(x, y, z) = \lim_{z\to 0} \frac{1}{2\pi} \sum_{i,j} B_n^{ij} I_z^{ij} = B_n(x, y, 0) \tag{A.3}$$

for $x = \dfrac{x_{i+1} + x_i}{2}$ and $y = \dfrac{y_{j+1} + y_j}{2}$.

REFERENCES

1. J. Adams and G. W. Pneuman, Sol. Phys. **46**, 185 (1976).
2. M. D. Altschuler and G. Newkirk, Jr., Sol. Phys. **9**, 131 (1969).
3. O. G. Den, O. E. Den, E. A. Kornitskaya, and M. M. Molodensky, Soln. Dannye **1**, 97 (1979).
4. B. P. Filippov and O. G. Den, Pis'ma Astron. Zh. **26**, 384 (2000) [Astron. Lett. **26**, 322 (2000)].
5. G. A. Korn and T. M. Korn, *Mathematical Handbook for Scientists and Engineers* (McGraw-Hill, New York, 1968; Nauka, Moscow, 1974).
6. N. S. Koshlyakov, E. B. Gliner, and M. M. Smirnov, *Partial Differential Equations of Mathematical Physics* (Vysshaya Shkola, Moscow, 1970).
7. R. H. Levine, Sol. Phys. **44**, 365 (1975).
8. R. H. Levine and M. D. Altschuler, Sol. Phys. **36**, 345 (1974).
9. S. G. Mikhlin, *Mathematical Physics: An Advanced Course* (Nauka, Moscow, 1968; North-Holland, Amsterdam, 1970).
10. Y. Nakagawa, Astron. Astrophys. **27**, 95 (1973).
11. Y. Nakagawa and M. A. Raadu, Sol. Phys. **25**, 127 (1972).
12. T. Sakurai, Sol. Phys. **76**, 301 (1982).
13. H. U. Schmidt, *Proceedings of the NASA Symposium on Physics of Solar Flares, 1964,* Ed. by W. N. Hess, NASA Sp-50, p. 107.
14. M. Semel, Ann. Astrophys. **30**, 513 (1967).
15. B. V. Somov, *Cosmic Plasma Physics* (Kluwer, Dordrecht, 2000), Chap. 16.

Translated by V. Astakhov